Fernando Redivo Cardoso

Platforms for Quantum Information and Technology

São Carlos

May 2024

Fernando Redivo Cardoso

Platforms for Quantum Information and Technology

PhD thesis submitted to the Postgraduate Coordination in Physics of the Center for Exact Sciences and Technology (CCET) at the Federal University of São Carlos.

Federal University of São Carlos – UFSCar

Center for Exact Sciences and Technology (CCET)

Graduate Program in Physics/CCET

Supervisor: Celso Jorge Villas-Bôas, Ana Predojević

São Carlos

May 2024

UNIVERSIDADE FEDERAL DE SÃO CARLOS

Centro de Ciências Exatas e de Tecnologia
Programa de Pós-Graduação em Física

Folha de Aprovação

Defesa de Tese de Doutorado do candidato Fernando Redivo Cardoso, realizada em 29/02/2024.

Comissão Julgadora:

Prof. Dr. Celso Jorge Villas Boas (UFSCar)

Profa. Dra. Yara Galvão Gobato (UFSCar)

Prof. Dr. Alexandre Dodonov (UnB)

Prof. Dr. Enrique Solano (KIPU QUANTUM)

Prof. Dr. Reginaldo de Jesus Napolitano (USP)

O Relatório de Defesa assinado pelos membros da Comissão Julgadora encontra-se arquivado junto ao Programa de Pós-Graduação em Física.

Acknowledgements

Firstly, I would like to thank Celso Jorge Villas-Bôas and Ana Predojević for their dedication and trust towards me during all the time I have worked under their supervision. Thanks to Prof. Villas-Bôas and Prof. Predojević, I have developed all my knowledge within scientific research, and the period under their orientation constitutes the time of my life in which I have learned the most.

To my parents, Regina Célia Redivo Cardoso and José Roberto Cardoso, and my sister, Roberta Redivo Cardoso, who always believed in me and made all of this possible.

To Murilo Henrique de Oliveira, for his friendship and support, not only during the years in which we worked under the supervision of Prof. Villas-Bôas, but to the present days. Thank you for all the meaningful conversations and discussions we had throughout the years, about both science and life.

Finally, I would like to thank CAPES (88882.426687/2019-01) and CAPES-STINT (88887.646229/2021-00) for the financial support during the whole project, and both Federal University of São Carlos and Stockholm University, for making this cotutelle thesis possible.

Abstract

This work presents a collection of scientific research results in the field of quantum information. The first paper describes the mathematical properties of a particular type of state of light, called the two-mode squeezed state (TMSS). We have shown that it is possible to generate a superposition of such states with particular probability distributions, making them suitable for applications in quantum information. In particular, such states are effectively phase insensitive, a property that enables a larger extraction of information regarding a dynamical process. The second paper deals with an extensive discussion on the complexity of quantum algorithms. It was observed that while quantum algorithms can, under certain conditions, outperform classical algorithms in time or space complexity, some key steps such as state preparation and information retrieval are not always taken into account when analysing the complexity of quantum algorithms. For this reason, the aim of this study was to provide a complete complexity analysis for the implementation of quantum algorithms, considering different alternatives in terms of state preparation, quantum gate implementation and measurement techniques. We provide an asymptotic analysis of different algorithm implementation strategies. Finally, the last paper deals with the Hong-Ou-Mandel interference visibility of photons emitted in a cascade process. As a result of a two-photon excitation process, an entangled photon pair is emitted. This unwanted entanglement affects the coherence of the reduced single photon state, i.e. one of the photons emitted in the cascade process. As a result, the visibility of the Hong-Ou-Mandel interference is reduced. We show that, under certain conditions, it is possible to circumvent the restriction imposed by the time-energy entanglement by applying a post-selection method. The experimental results together with the theoretical framework are presented to provide a complete analysis of the method.

Keywords: Quantum Computation, Quantum Information, Single Photons, Quantum Interference.

List of Figures

Contents

1 Overview

In this work, platforms such as trapped ions and quantum dots were investigated for the study of quantum information, under the joint supervision of Prof. Dr. Celso Jorge Villas-Bôas and Prof. Dr. Ana Predojević, as part of a cotutelle Ph.D. between Federal University of São Carlos (Brazil) and Stockholm University (Sweden).

Firstly, we have treated quantum information in its basis regarding the properties of two-mode squeezed states. The probability distributions in phase space were investigated, showing potential applications in quantum metrology. In particular, we have employed the concept of Fisher information to estimate the amount of information that can be extracted about a dynamical process, using the reduced states of the two-mode squeezed state as probe. The results show a phase insensitive behavior, thus making the aforementioned reduced modes a robust platform to estimate displacements in any direction in phase space. Entanglement properties were also investigated, and the purity of the resulting reduced state was used as an entanglement witness. The results surpass the degree of entanglement of the EPR states for a lower squeezing parameter.

Secondly, we have analyzed computational complexity in depth, with the objective to quantify and optimize the implementation of quantum algorithms, as a way to approach the processing of quantum information. We point out the space and time complexity aspects of the information input, processing and reading, providing a detailed analysis and quantifying lower and upper bounds for resources under distinct architectures for quantum computation and hardware.

Under Prof. Predojević's supervision, I took part on the study of properties of two-photon interference. Specifically, we have investigated the impact of temporal correlations and time-energy entanglement on the Hong-Ou-Mandel interference of photons emitted in a cascaded process. We show that with the application of postselection techniques, it is possible to circumvent the restrictions imposed by the unwanted entanglement and obtain increased Hong-Ou-Mandel interference visibility. I have collaborated with the computational simulations and implementation of a method to calculate correlation functions and coherence properties. This work, entitled *Impact of temporal correlations, coherence, and postselection on two-photon interference*, is submitted to Physical Review Letters.

This thesis is divided into four main parts. In the first part, we have a quick theoretical background, presenting the basic concepts of Hong-Ou-Mandel interference, quantum computation and quantum Fisher information with squeezed states. In the following three chapters, the three works mentioned above are presented, followed by an

overview.

1.1 Author's Contribution

Paper I

Superposition of two-mode squeezed states for quantum information processing and quantum sensing

Fernando Redivo Cardoso, Daniel Zini Rossato, Gabriel P. L. M. Fernandes, Gerard Higgins, and Celso J. Villas-Bôas.

Phys. Rev. A **103**, 062405 (2021).

This paper addresses the mathematical properties of two-mode squeezed states, whose generation is covered in previous work [1]. In this work, we analyze properties such as photon number distribution, Wigner functions and entanglement. We study the application of even and odd two-mode squeezed states for estimation of parameters in quantum metrology with the concept of quantum Fisher information. My contributions are:

- Study of the general superposition generated originally in [1], with the quantification of photon distribution and calculation of analytical Wigner functions.
- Quantification of entanglement for the superpositions related to the relative phase factor between states, identifying conditions in which entanglement is maximized.
- Calculation of analytical expressions for quantum Fischer information and discussion about the advantages of phase-insensitive states obtained by reduction of the wavepacket, in comparison to the single mode squeezed states.
- Development of Python and Julia codes to implement the generation of the studied superpositions in the context of trapped ion systems.

Paper II

Detailed account of complexity for implementation of circuit-based quantum algorithms

Fernando Redivo Cardoso, Daniel Yoshio Akamatsu, Vivaldo Leiria Campo Junior, Eduardo I. Duzzioni, Alfredo Jaramillo, Celso J. Villas-Bôas.

Frontiers in Physics **9**, 731007 (2021).

In this work we analyze the computational complexity for implementation of quantum algorithms, considering the circuit model for quantum computation. We consider the space and time complexity of fundamental steps of a quantum algorithm, such as state preparation and measurement processes, under a variety of methods. The analysis covers distinct architectures for information input of initial conditions, covered by state preparation, decomposition of quantum gates for information processing, and quantum state tomography for the retrieval of the output results. My contributions to this paper are:

- Research of references for methods of quantum state preparation and quantum state tomography, together with the respective space and time complexity aspects.
- Research of complexity aspects for quantum gate decomposition.
- Estimatives of overall space and time complexity for combined techniques of state preparation, state manipulation via quantum gates, and reading of output results via quantum state tomography.
- Writing of all sections covered in the published paper, except for *4.1 - Pure State Tomography*.
- Review and discussion of all sections with all collaborators.

Paper III

Trapped ions as architecture for quantum computation

Gabriel P. L. M. Fernandes, Alexandre C. Ricardo, Fernando R. Cardoso and Celso J. Villas-Bôas.

.

This work consists of a text published for educational purposes. The basic concepts of trapped ion systems are reviewed, together with the basic interactions and implementation of quantum gates.

- Review of the main text and appendices.
- Contribution to “State of the art" section.

Paper IV

Impact of temporal correlations, coherence and postselection on two-photon interference

Fernando R. Cardoso, Jaewon Lee, Riccardo Checchinato, Jan-Heinrich Littmann, Marco De Gregorio, Sven Höfling, Christian Schneider, Celso J. Villas-Bôas and Ana Predojević.

arXiv: 2312.01503 (2024).

In this work we investigate how two-photon interference is impacted by properties of the photon emitter, wavepacket and the measurement process. In particular, we consider photons generated via a cascade emission process in a quantum dot. We performed simulations to obtain parameters regarding dissipative processes, such as dephasing of the internal energy levels of the quantum dot. The parameters are estimated by fitting of experimental data to theoretical results, convoluted with the response time of the detectors. We performed the experimental measurements, and the simulations consider a theoretical model for photon emission and calculation of two-photon correlations. We implemented the Monte Carlo wavefunction stochastic method for theoretical temporal postselection. My contributions to this work are:

- Development of all codes for simulation of the physical system with the quantum master equation formalism, written in Python and Julia programming languages.
- Simulation of all theoretical results presented in the paper, with the implementation of the sensor method [2].
- Proposition and Implementation of Monte Carlo stochastic method for theoretical simulation of photon postselection.
- Calculation of all theoretical values for Hong-Ou-Mandel interference visibility presented in the main text and supplemental material.

2 Teorethical background

2.1 Superposition of two-mode squeezed states and quantum Fisher information

In this section, we study the properties of superpositions of two-mode squeezed states and its potential applications in quantum information. In particular, we analyze the properties of the aforementioned superpositions for estimation of parameters involved in dynamical processes in the domain of quantum metrology. The application of squeezed states in quantum metrology is motivated by the possibility of obtaining reduced uncertainty in a variable, for instance, position x, at the expense of increasing the deviation in its conjugated variable, in this case, momentum p, without violating the intrinsic restriction imposed by the Heisenberg uncertainty principle [3]. We focus the study of the applications in quantum metrology in the reduced modes of the superposition of two-mode squeezed states, obtained by the reduction of the density matrix corresponding to the composed two-mode bosonic states in the system [4]. Specifically, we concentrate the analysis of two particular cases of the reduced modes of the superposition of two-mode squeezed states, namely, the even and odd states, which will be introduced further. It is shown that, due to the peculiar probability distributions in phase space, given by its Wigner functions, it is possible to obtain a robust platform for measurements that is phase independent, representing an advantage over the single mode squeezed states in certain cases [4]. The entanglement properties of the superposition of two-mode squeezed states are investigated, as a function of its squeezing and relative phase factors. This correlation is a fundamental ingredient for fundamental tests of quantum mechanics such as the Einstein-Podolski-Rosen paradox [5, 6], for implementation of quantum teleportation [7] and quantum computation [8, 9] with continuous variables, among others. The generation process for the two-mode squeezed states, originally presented in [1], take place through the interaction between a two-level system and two modes of the quantized electromagnetic field. The concept of quantum Fisher information is presented, along with the estimation protocol for parameters involved in dynamical processes. The mathematical properties of the states, such as occupation probabilities and Wigner functions are described [4].

2.1.1 Parameter estimation and quantum Fisher information

Metrology is the science that studies the theoretical and experimental aspects and methods of measurement processes of a physical quantities associated with a physical system or dynamical process of interest. Examples include measuring the length of a bar,

time intervals between events, estimating the acceleration of gravity, among others. It is of great interest that the measured value of a variable inherent to the system is as close as possible to the real value of this quantity, i.e. that the uncertainty associated with the measured value is minimized. The central interest of metrology, therefore, is the process of optimizing measurements and minimizing the uncertainties associated with them.

On the macroscopic scale, it is natural to relate the precision of the measurements to the instrument used to perform it. For quantum systems, the uncertainty principle

$$\Delta x \Delta p \geq \frac{\hbar}{2} \tag{2.1}$$

defines a limit for the deviations associated with the canonically conjugated variables x and p [10]. This means that the intrinsic properties of the theory prevent the estimation of quantities with absolute precision. Quantum metrology investigates the apllication of quantum systems, such as quantized modes of the electromagnetic field, in the estimation of parameters involved in physical process in order to achieve minimum uncertainty in measurement processes, within the limit imposed by the uncertainty principle.

The process of parameter estimation can be implemented through the estimation protocol, which involves the quantum system as a probe that interacts with a dynamical process. The protocol, in general, is described through the following steps [11]:

- The "probe", as the state that interacts with the dynamical process containing the parameter to be estimated, y, is prepared into a known initial configuration, described quantitatively by the density operator ρ;
- The configuration of the probe is altered by the process, making it dependent on the parameter $\rho = \rho(y)$;
- An experimental measurement is performed on the final probe configuration, with the result denoted by κ;
- An estimate of the parameter is made, y_{est}, using a well-established rule to compute y.

The rule mentioned in the last step of the established protocol depend on the process in question. It is necessary to have knowledge of the phenomenon in order to be able to estimate the unknown parameter y by means of κ. The experimental apparatuses utilized in the measurements are represented mathematically by a set of positive operator valued measure (POVM's) $\{E_\kappa\}$, which generally define the measurement processes in quantum mechanics [11], and satisfy the relation

$$\sum_\kappa E_\kappa = \mathbf{1}. \tag{2.2}$$

The theoretical model for calculating the estimation of y is based on the distribution of experimental results. For each experimental result κ, a probability is associated, dependent on the estimation parameter y, $P_\kappa(y)$, such that at the end of a sequence of measurements, the associated set of probabilities, $\{P_\kappa(y)\}$, is known. The mean value of the parameter, calculated using the individual values of the estimates, is defined by

$$\langle y_{est}\rangle = \sum_\kappa y_{est}(\kappa) P_\kappa(y), \tag{2.3}$$

with the probabilities properly normalized,

$$\sum_\kappa P_\kappa(y) = 1. \tag{2.4}$$

Using the normalization of probabilities,

$$\sum_\kappa y_{est}(\kappa) P_\kappa(y) - \sum_\kappa \langle y_{est}\rangle\, P_\kappa(y) = \sum_\kappa P_\kappa(y)\left[y_{est}(\kappa) - \langle y_{est}\rangle\right] = 0, \tag{2.5}$$

where the estimates $y_{est}(\kappa)$ are constant values. Deriving this result in relation to the y parameter, we get

$$\sum_\kappa P_\kappa(y) \frac{\mathrm{d}\ln(P_\kappa(y))}{\mathrm{d}y}\left[y_{est}(\kappa) - \langle y_{est}\rangle\right] = \frac{\mathrm{d}\langle y_{est}\rangle}{\mathrm{d}y}. \tag{2.6}$$

Squaring (2.6) and using the Cauchy-Schwarz inequality [12], we get

$$\left(\sum_\kappa P_\kappa(y)\left(\frac{\mathrm{d}\ln(P_\kappa(y))}{\mathrm{d}y}\right)^2\right)\left(\sum_\kappa P_\kappa(y)\left[y_{est}(\kappa) - \langle y_{est}\rangle\right]^2\right) \geq \left(\frac{\mathrm{d}\langle y_{est}\rangle}{\mathrm{d}y}\right)^2. \tag{2.7}$$

Defining the variance associated with the estimation variable $\langle \Delta y\rangle^2 \equiv \langle (y_{est} - \langle y_{est}\rangle)^2\rangle$, and substituting it in (2.7), we get

$$\langle \Delta y\rangle^2 \geq \frac{\left(\frac{\mathrm{d}\langle y_{est}\rangle}{\mathrm{d}y}\right)^2}{\left\langle\left(\frac{\mathrm{d}\ln(P_\kappa(y))}{\mathrm{d}y}\right)^2\right\rangle}, \tag{2.8}$$

which is called the Cramér-Rao inequality. The quantity in the denominator,

$$F(y) \equiv \left\langle\left(\frac{\mathrm{d}\ln(P_\kappa(y))}{\mathrm{d}y}\right)^2\right\rangle, \tag{2.9}$$

is called Fisher information, and represents the amount of information about the parameter y available in the probability set [11]. As $F(y)$ limits the deviation in the value of the parameter, the calculation of this quantity is of central interest for minimizing the uncertainties inherent in the measurement process.

2.1.2 Computation of the Quantum Fisher Information

To calculate the Quantum Fisher Information for the density matrix $\rho(y)$, it is necessary to construct the set of probabilities $\{P_\kappa(y)\}$. The probability $P_\kappa(y)$ associated with an experimental result is [11]

$$P_\kappa(y) = \mathrm{Tr}(\rho(y)E_\kappa), \tag{2.10}$$

where E_κ is the POVM associated with the measurement process on the probe, described in the protocol. As mentioned above, the uncertainty principle prohibits estimating parameters with absolute precision. However, it is natural to seek maximum precision in measurement processes, obtaining estimates close to the real value of the parameters, within the Heisenberg limit. This situation is equivalent, within the estimation theory presented, to maximizing Fisher's Information. Quantum Fisher Information is then given by the maximization over all POVM's $\{E_\kappa\}$,

$$F_Q[\rho(y)] \equiv \max_{\{E_\kappa\}} \left[\sum_\kappa \frac{1}{\mathrm{Tr}(\rho(y)E_\kappa)} \left(\frac{\mathrm{d}\,\mathrm{Tr}(\rho(y)E_\kappa)}{\mathrm{d}y} \right)^2 \right], \tag{2.11}$$

which is equivalent to performing the maximization on all the experimental apparatuses allowed by quantum mechanics [11]. However, an upper bound [13] for Fisher's Information is given in terms of the Hermitian operator symmetric logarithmic derivative, L_y, defined by the differential equation

$$\frac{\mathrm{d}\rho(y)}{\mathrm{d}y} = \frac{L_y\rho + \rho L_y}{2}. \tag{2.12}$$

Using (2.12), one gets

$$\frac{\mathrm{d}\,\mathrm{Tr}(\rho(y)E_\kappa)}{\mathrm{d}y} = \mathrm{Tr}\Big(\frac{L_y\rho + \rho L_y}{2} E_\kappa \Big), \tag{2.13}$$

and, using $\mathrm{Tr}(A)^* = \mathrm{Tr}\big(A^\dagger\big)$,

$$\mathrm{Tr}\Big(\frac{L_y\rho + \rho L_y}{2} E_\kappa \Big) = \frac{1}{2}\left[\mathrm{Tr}(E_\kappa\rho L_y) + \mathrm{Tr}(\rho L_y E_\kappa)^*\right] = \mathrm{Re}\{\mathrm{Tr}(E_\kappa\rho L_y)\}, \tag{2.14}$$

where the cyclic properties of the trace and the hermiticity of the operators were used. With the application of the Cauchy-Schwarz inequality,

$$\mathrm{Tr}\Big(\frac{L_y\rho + \rho L_y}{2} E_\kappa \Big) \leq |\mathrm{Tr}(E_\kappa\rho L_y)|^2. \tag{2.15}$$

Now, using the inequality [11]

$$\Big|\mathrm{Tr}\big(A^\dagger B\big)\Big|^2 \leq \mathrm{Tr}\big(A^\dagger A\big)\,\mathrm{Tr}\big(B^\dagger B\big), \tag{2.16}$$

and defining $A = \sqrt{\rho}\sqrt{E_\kappa}$, $B = \sqrt{\rho}L_y\sqrt{E_\kappa}$, we have

$$\begin{aligned} \mathrm{Tr}\left(A^\dagger B\right) &= \mathrm{Tr}(E_\kappa \rho L_y), \\ |\mathrm{Tr}(E_\kappa \rho L_y)|^2 &\leq \mathrm{Tr}(E_\kappa \rho)\,\mathrm{Tr}(E_\kappa L_y \rho L_y), \\ \left[\mathrm{Tr}\left(\frac{\mathrm{d}\rho}{\mathrm{d}y}E_\kappa\right)\right]^2 &\leq \mathrm{Tr}(E_\kappa \rho)\,\mathrm{Tr}(E_\kappa L_y \rho L_y), \\ \frac{1}{\mathrm{Tr}(E_\kappa \rho)}\left[\mathrm{Tr}\left(\frac{\mathrm{d}\rho}{\mathrm{d}y}E_\kappa\right)\right]^2 &\leq \mathrm{Tr}(E_\kappa L_y \rho L_y). \end{aligned} \tag{2.17}$$

We can then write the Fisher information as

$$F_Q[\rho(y)] \leq \sum_\kappa \mathrm{Tr}(E_\kappa L_y \rho L_y), \tag{2.18}$$

which, due to the condition $\sum_\kappa E_\kappa = \mathbf{1}$, becomes

$$F_Q[\rho] \leq \mathrm{Tr}\left(\rho L_y^2\right). \tag{2.19}$$

The inequality (2.19) reveals an independence of the maximization of Fisher's Information with respect to the set of all POVM's, $\{E_\kappa\}$, which can be increased by modifying the initial configuration of the probe, represented by the density operator ρ, in order to find the highest value of this in the estimation of an unknown parameter y.

2.1.2.1 Pure states

In the case of pure states, a simplified form for L_y can be found: Making $\rho^2 = \rho$,

$$\frac{\mathrm{d}\rho}{\mathrm{d}y} = \frac{\mathrm{d}\rho^2}{\mathrm{d}y} = \frac{\mathrm{d}\rho}{\mathrm{d}y}\rho + \rho\frac{\mathrm{d}\rho}{\mathrm{d}y}. \tag{2.20}$$

Rewriting (2.12) and substituting, you get

$$\frac{1}{2}L_y\rho + \rho\frac{1}{2}L_y = \frac{\mathrm{d}\rho}{\mathrm{d}y}\rho + \rho\frac{\mathrm{d}\rho}{\mathrm{d}y}, \tag{2.21}$$

where we conclude that $L_y = 2\frac{\mathrm{d}\rho}{\mathrm{d}y}$. For the case of a unitary evolution of the form

$$U(y) = \mathrm{e}^{-\mathrm{i}yG}, \tag{2.22}$$

the evolution of the initial state $|\psi_0\rangle$ is given by

$$\mathrm{i}\hbar\frac{\mathrm{d}\,|\psi\rangle}{\mathrm{d}y} = G\,|\psi\rangle\,. \tag{2.23}$$

which is the Schrödinger equation for the evolution of the initial state under the action of the transformation represented by the G operator, so that $|\psi\rangle = U(y)\,|\psi_0\rangle$. Deriving with respect to the parameter y, and substituting in (2.19), the Quantum Fisher Information is written, for a pure state, as

$$F_Q(\rho(y)) = 4(\Delta G)^2, \tag{2.24}$$

where $(\Delta G)^2 = \langle G^2\rangle - \langle G\rangle^2$ is the variance associated with the operator G, which generates the inprint of the unknown parameter in the density matrix ρ.

2.1.2.2 Mixed states

For mixed-state estimation under the action of the G parameter inprint generator, the evolution of the ρ probe configuration is given by the Von-Neumann equation [14]

$$\mathrm{i}\frac{\partial\rho}{\partial y} = G\rho - \rho G. \tag{2.25}$$

Rewriting the density matrix in spectral representation, with the eigenvalues and eigenvectors in a base $\{|m\rangle\}$, we get

$$\rho = \sum_m \lambda_m \, |m\rangle\langle m| \, . \tag{2.26}$$

Using (2.25), the array element corresponding to the operator $\dfrac{\partial\rho}{\partial y}$ is

$$\langle m|\frac{\partial\rho}{\partial y}|n\rangle = \langle m|-\mathrm{i}G\rho + \mathrm{i}\rho G|n\rangle = \mathrm{i}(\lambda_m - \lambda_n)\,\langle m|G|n\rangle \, , \tag{2.27}$$

from which we conclude

$$\langle m|G|n\rangle = \frac{1}{\mathrm{i}(\lambda_m - \lambda_n)}\,\langle m|\frac{\partial\rho}{\partial y}|n\rangle \, . \tag{2.28}$$

From equation (2.19), Fisher information is maximal when

$$F_Q = \mathrm{Tr}\Big(\rho L^2\Big), \tag{2.29}$$

which, using the definition of the symmetric logarithmic derivative operator (2.12), becomes

$$F_Q = \mathrm{Tr}\left(\frac{\partial\rho}{\partial y}L\right). \tag{2.30}$$

Rewriting the trace of the equation (2.30),

$$F_Q = \sum_m \langle m|\frac{\partial\rho}{\partial y}L|m\rangle = \sum_{m,n}\langle m|\,\frac{\partial\rho}{\partial y}\,|n\rangle\langle n|\,L\,|m\rangle \tag{2.31}$$

where the completeness relation $\sum_n |n\rangle\langle n| = \mathcal{I}$ has been inserted. Using the definition expressed in (2.12), one can write the form of the matrix element of the operator L as

$$\langle n|\frac{\partial\rho}{\partial y}|m\rangle = \frac{1}{2}(\lambda_n + \lambda_m)\,\langle n|L|m\rangle \, . \tag{2.32}$$

Substituting (2.32) in (2.31) gives the expression for Fisher's information,

$$F_Q = \sum_{m,n}\frac{2}{\lambda_m + \lambda_n}\left|\,\langle m|\frac{\partial\rho}{\partial y}|n\rangle\right|^2 . \tag{2.33}$$

In terms of the operator that generates the printout of the parameter in the density matrix ρ, using (2.25),

$$\langle m|\frac{\partial\rho}{\partial y}|n\rangle = \mathrm{i}(\lambda_m - \lambda_n)\,\langle m|G|n\rangle \, , \tag{2.34}$$

so that Fisher's information, written in terms of G, takes the form

$$F_Q = 2\sum_{m,n} \frac{(\lambda_m - \lambda_n)^2}{\lambda_m + \lambda_n} |\langle m|G|n\rangle|^2. \tag{2.35}$$

In this way, it is possible to calculate F_Q in a simple way, with the eigenvalues and eigenvectors of the density matrix ρ, which now represents a mixed state.

2.1.3 Two-mode squeezed states

The superposition of two-mode squeezed states are generated in the context of the interaction between an atom driven by a laser field and two modes of the quantized electomagnetic field [1]. The interaction between the atomic states and the field modes is represented by the effective Hamiltonian [1]

$$H = \chi(ab + a^\dagger b^\dagger)(\sigma_{--} - \sigma_{++}), \tag{2.36}$$

where a and b ($a^\dagger$ e $b^\dagger$) are the annihilation (creation) operators of the field modes, and $\sigma_{\pm\pm} = |\pm\rangle\langle\pm|$ are the operators that act on the atomic states. Here $|\pm\rangle = 1/\sqrt{2}(|g\rangle \pm |e\rangle$, with $|g\rangle$ and $|e\rangle)$ being the ground and excited states of the atom, respectively. The initial state of the atom under consideration is prepared as the superposition of spin states

$$|\phi_0\rangle = \frac{1}{\sqrt{2}}\left(|+\rangle + e^{i\varphi}|-\rangle\right), \tag{2.37}$$

where $e^{i\varphi}$ represents the relative phase factor between the $|+\rangle$ and $|-\rangle$ states.

The electromagnetic field inside the cavity is initially in the vacuum state, represented by

$$|\psi_0\rangle = |0,0\rangle. \tag{2.38}$$

The time evolution of the composite system, given by the product state $|\Psi\rangle = |\phi_0\rangle \otimes |\psi_0\rangle$ (atom and bosonic modes) is governed by the Hamiltonian (2.36), and generates the state

$$|\Psi(t)\rangle = e^{\frac{-it}{\hbar}\chi(ab+a^\dagger b^\dagger)(\sigma_{--}-\sigma_{++})}\left[\frac{1}{\sqrt{2}}\left(|+\rangle + e^{i\varphi}|-\rangle\right) \otimes |0,0\rangle\right]. \tag{2.39}$$

The action of the atom operators on the atomic state $|\phi_0\rangle$ results in

$$|\Psi(t)\rangle = \frac{1}{\sqrt{2}}\left[|+\rangle e^{r(ab+a^\dagger b^\dagger)}|0,0\rangle + e^{i\varphi}|-\rangle e^{-r(ab+a^\dagger b^\dagger)}|0,0\rangle\right], \tag{2.40}$$

where $\frac{i\chi t}{\hbar} = \xi$, with $|\xi| = r$ being the squeezing factor. A measurement performed on the atomic state on the basis $\{|+\rangle, |-\rangle\}$ leaves the field in the final configuration

$$|\psi_\pm(r)\rangle = S_\pm(r)|0,0\rangle, \tag{2.41}$$

where $S_{12,(\pm)}(r) = \mathrm{e}^{\pm r(ab+a^\dagger b^\dagger)}$ is the operator that generates the squeezing in the state of the field [3]. Represented in the Fock basis, the states $|\psi_\pm(r)\rangle$ can be written as [1]

$$|\psi_\pm(r)\rangle = \frac{1}{\cosh(r)} \sum_{n=0}^{\infty} [\pm \tanh(r)]^n \, |n,n\rangle \, . \tag{2.42}$$

After taking the partial trace over either of the modes, we obtain the reduced density matrix,

$$\rho_{1,+}(r) = \frac{1}{\cosh^2(r)} \sum_{n=0}^{\infty} \tanh^{2n}(r) \, |n\rangle\langle n| \, , \tag{2.43}$$

which describes a thermal state distribution.

Performing a change of basis to the atom states $\{|e\rangle \, , |g\rangle\}$, with

$$|\pm\rangle = \frac{1}{\sqrt{2}} \left(|g\rangle \pm |e\rangle\right) , \tag{2.44}$$

one can rewrite the final configuration of the composite system (2.40) in the form

$$|\Psi(r,\varphi)\rangle = \frac{1}{2} \left[|g\rangle \left(|\psi_+(r)\rangle + \mathrm{e}^{\mathrm{i}\varphi} \, |\psi_-(r)\rangle \right) + |e\rangle \left(|\psi_+(r)\rangle - \mathrm{e}^{\mathrm{i}\varphi} \, |\psi_-(r)\rangle \right) \right] . \tag{2.45}$$

Measurements performed on the atomic states on the basis $\{|g\rangle \, , |e\rangle\}$ leave the field in the superposition

$$|\psi(r,\varphi)\rangle = \mathcal{N}(r,\varphi) \left(|\psi_+(r)\rangle \pm \mathrm{e}^{\mathrm{i}\varphi} \, |\psi_-(r)\rangle \right) , \tag{2.46}$$

where $\pm$ refers to the atom detected either in the $|g\rangle$ or in the $|e\rangle$ atomic states. Represented in Fock basis, the superposition is written as

$$|\psi(r,\varphi)\rangle = \mathcal{N}(r,\varphi) \left[\sum_{n=0}^{\infty} \tanh^n(r) \left(1 \pm \mathrm{e}^{\mathrm{i}\varphi} (-1)^n \right) |n,n\rangle \right] , \tag{2.47}$$

where $\mathcal{N}(r,\varphi)$ stands for the normalization factor, with

$$|\mathcal{N}(r,\varphi)|^2 = \frac{1}{2} \left[\frac{1 - \tanh^4(r)}{(1 + \tanh^2(r)) \pm \cos(\varphi)(1 - \tanh^2(r))} \right] . \tag{2.48}$$

Similarly, the reduced density matrix corresponding to the two-mode state (2.47) is given by

$$\rho_1 = |\mathcal{N}(r,\varphi)|^2 \sum_{n=0}^{\infty} 2 \tanh^{2n}(r) \left[1 \pm \cos(\varphi)(-1)^n \right] |n\rangle\langle n| \, . \tag{2.49}$$

The even and odd EPR states are special cases generated when $\varphi = 0$ and $\varphi = \pi$, respectively, and can be written as

$$\left| \psi_{(e,o)}(r) \right\rangle = \mathcal{N}_{(e,o)}(r) \sum_{n=0}^{\infty} \tanh^n(r) (1 \pm (-1)^n) \, |n,n\rangle \, , \tag{2.50}$$

where the indexes e, o identify the even and odd states, represented by the positive and negative signs on the right-hand side of eq. (2.50), respectively, with the normalization factor given by

$$\left| \mathcal{N}_{(e,o)}(r) \right|^2 = \frac{1}{2 \sum_{n=0}^{\infty} \left[\tanh^{2n}(r) (1 \pm (-1)^n) \right]} . \tag{2.51}$$

The states described by $\left|\psi_{(e,o)}(r)\right\rangle$ have occupation probabilities concentrated on even and odd number states of excitation. In fact, the substitution of φ in equation (2.49) results in the expressions

$$|\psi_e(r)\rangle = 2\mathcal{N}_e(r)\sum_{n=0}^{\infty}\tanh^{2n}(r)\,|2n,2n\rangle\,, \tag{2.52a}$$

$$|\psi_o(r)\rangle = 2\mathcal{N}_o(r)\sum_{n=0}^{\infty}\tanh^{2n+1}(r))\,|2n+1,2n+1\rangle\,. \tag{2.52b}$$

with the corresponding reduced density matrix for the single-mode states

$$\rho_{1,(e,o)}(r) = \left|\mathcal{N}_{(e,o)}(r)\right|^2\sum_{n=0}^{\infty}2\tanh^{2n}(r)(1\pm(-1)^n)\,|n\rangle\langle n|\,. \tag{2.53}$$

Figure 1 shows the photon distributions and Wigner functions for the studied EPR states.

The states represented by the reduced density matrices $\rho_1(r,\varphi)$ show peculiar characteristics as the squeezing factor r increases. Similar to $|\psi_+(r)\rangle$, the even and odd EPR states are left in a mixture of Fock states after the reduction of its respective density operators. However, the probability distributions $W(q,p)$ behave differently when compared to $|\psi_+(r)\rangle$, as the Wigner function for the even and odd states is concentrated on the vicinity of the origin. This particular feature of $\left|\psi_{(e,o)}(r)\right\rangle$ motivates its application in the estimation of parameters with quantum metrology.

2.2 Quantum algorithms and complexity aspects

This section provides a theoretical introduction to quantum computing. The basic concepts such as qubits, algorithms, circuit representation and complexity aspects will be presented, along with the operations that need to be performed on the system to process information and reading of the output results.

2.2.1 Qubit states and units of information

Classical bits: The bit (binary digit) is the smallest unit of information that can be stored or transmitted. Two different values can be associated with a bit: 0 or 1. Bits can be read, stored, manipulated and transmitted using various types of physical elements, such as electronic devices, in which the bit is associated with the presence or absence of electrical charge or current. Information represented by more than bit is called a bit string and its length depends on the information to be processed.

Quantum bits: The qubit, like classical bits, among its possible configurations, also present the values 0 and 1, which are conveniently represented here by the Dirac notation $|0\rangle$ and $|1\rangle$, denominated computational basis states [15]. The fundamental difference between bits and qubits is that in the case of qubits, the states can be found in states

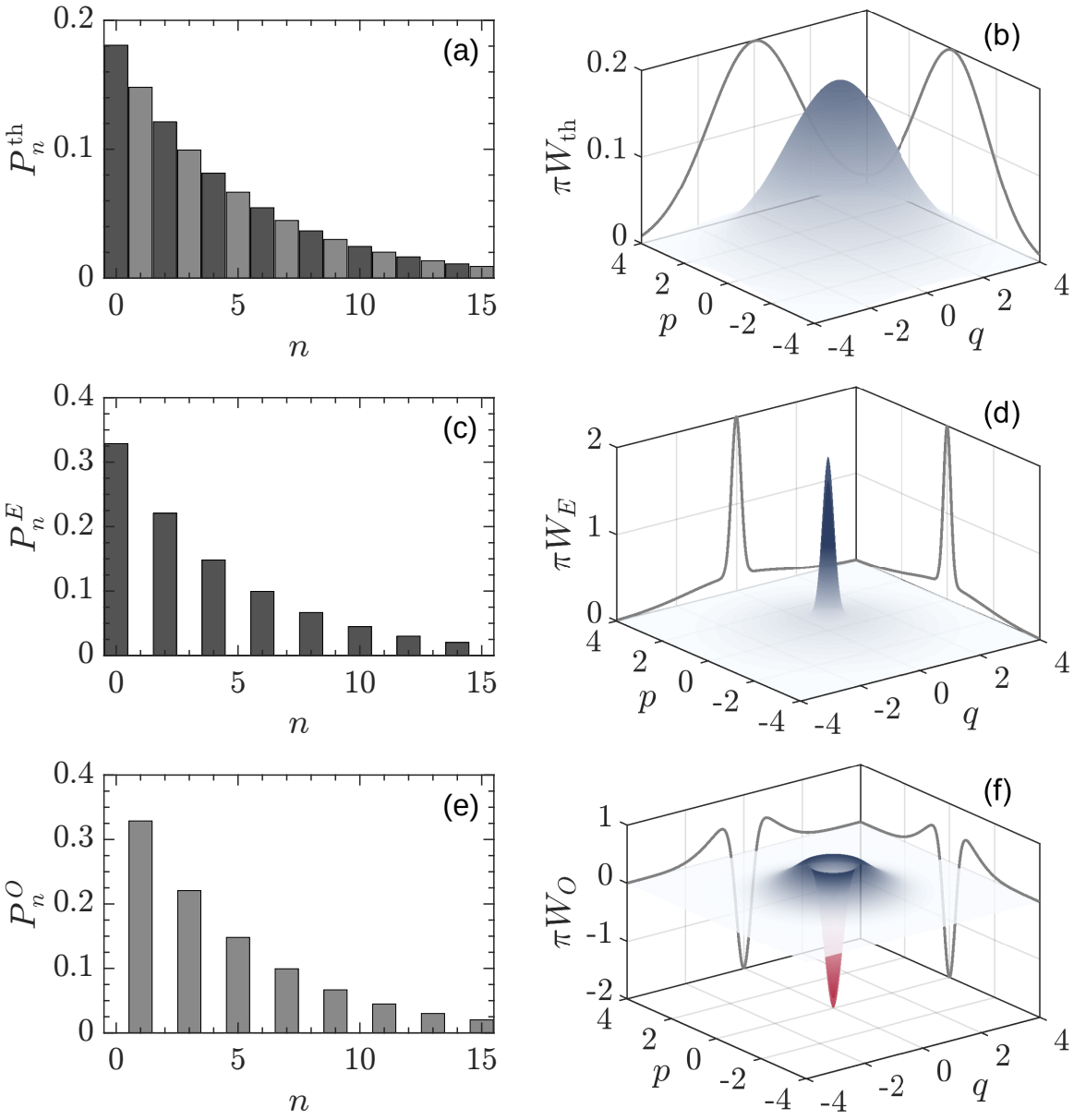

Figure 1 – Field properties of EPR states. In the left panels we show the populations in the Fock basis of the reduced (a) EPR (c) even and (e) odd EPR states, for squeezing parameter $r = 1.5$. In the right panels (b), (d) and (f) the Wigner functions for each of the respective states are represented. Reprinted figure with permission from Fernando R. Cardoso, Daniel Z. Rossatto, Gabriel P. L. M. Fernandes, Gerard Higgins, and Celso J. Villas-Bôas, Physical Review A 103, 062405, 2021. Copyright (2021) by the American Physical Society.

that are not only $|0\rangle$ or $|1\rangle$, but in superpositions of those. The general qubit state can be represented by

$$|\psi\rangle = \alpha\,|0\rangle + \beta\,|1\rangle\,. \tag{2.54}$$

The complex coefficients α and β are interpreted as probability amplitudes, and are related

by $|\alpha|^2 + |\beta|^2 = 1$. Formally the qubit is characterized by a vector in a complex vector space, called Hilbert space. The vector space also allows one qubit to be represented in linear combinations of the basis states $\{|0\rangle, |1\rangle\}$ for example

$$|+\rangle = \frac{1}{\sqrt{2}} (|0\rangle + |1\rangle), \tag{2.55}$$

which represents one case of superposition of states from the computational basis, with equal probabilities of the possible measurement outcomes $|\langle 0|+\rangle|^2 = |\langle 1|+\rangle|^2 = 1/2$.

Classicaly, information can be encoded and stored as a string of n bits, with n depending on the information encoded. For $n = 2$, a string can be in $2^n = 4$ possible states, namely 00, 01, 10, 11. In the quantum case, a string with n bits is defined by the composite quantum state

$$|\Psi\rangle = |e_1\rangle \otimes |e_2\rangle \otimes \ldots \otimes |e_n\rangle, \tag{2.56}$$

$e_i = \{0, 1\}$, in the Hilbert space given by the product of the individual Hilbert spaces of each of the components, $\mathcal{H} = \mathcal{H}_1 \otimes \mathcal{H}_2 \otimes \ldots \otimes \mathcal{H}_n$. For the example of $n = 2$, the state of the string is in general represented, making use of the computational basis states $\{|0\rangle, |1\rangle\}$ for each of the components, by

$$|\Psi\rangle = \alpha |00\rangle + \beta |01\rangle + \gamma |10\rangle + \delta |11\rangle. \tag{2.57}$$

In general, a string with n bits will be represented as the composite quantum state of n qubits, with dimension $d = 2^n$. A quantum state that generically represents the state of such string can be written as the superposition

$$|\Psi\rangle = \alpha_{\underbrace{0\ldots0}_{\text{n indexes}}} |0\ldots0\rangle + \ldots + \alpha_{\underbrace{1\ldots1}_{\text{n indexes}}} |1\ldots1\rangle = \sum_{i_1,\ldots,i_n=0,1} \alpha_{i_1\ldots i_n} |i_1\ldots i_n\rangle. \tag{2.58}$$

Naturally, as in the classical case, as the amount of information processed or stored increases, here represented simply by the length of the string, so does the amount of resources needed to process or store it. Those resources are here represented by the number of qubits needed to represent such a state.

2.2.2 Logic operations

2.2.2.1 Single qubit gates

Quantum information processing is done using gates. A quantum circuit is composed of quantum gates and wires that carry bits between them. The quantum gates are sets of

operators acting on the qubit whose state must be transformed. An operation performed on the state $|\psi\rangle$ can be written as

$$|\psi'\rangle = U|\psi\rangle\,, \tag{2.59}$$

where $|\psi'\rangle$ denotes the transformed state after the action of the quantum gate U. For $|\psi'\rangle$ to be normalized, U must be unitary.

Due the unitarity of the quantum gates, there is an inverse operation such that $U^\dagger U = \mathcal{I}$, with $\mathcal{I}$ representing the identity operator. For this reason, quantum gates are reversible: the initial state in eq. (2.59) can be reverted applying the inverse quantum gate, $|\psi\rangle = U^\dagger|\psi'\rangle$, and the initial state is recovered. The quantum gates can be divided into single- and multi-qubit gates.

Single qubit operations are quantum gates that alter the state of one qubit only, leaving the other qubits untouched. Examples of single qubit operations comprise rotations, which rotate the vector on the Bloch sphere [15], and the NOT operation.

The NOT operation has the action of "negation" of the value, as it flips the qubit on the Bloch sphere. The action of this gate is

$$|0\rangle \xrightarrow{\text{NOT}} |1\rangle\,, |1\rangle \xrightarrow{\text{NOT}} |0\rangle\,. \tag{2.60}$$

Representing the states as vectors $|0\rangle = (1,0)$, $|1\rangle = (0,1)$, the NOT gate corresponds to the Pauli σ_x matrix,

$$\text{NOT} \equiv X = \begin{pmatrix} 0 & 1 \\ 1 & 0 \end{pmatrix}. \tag{2.61}$$

Single qubit rotations can be in general defined as the operator

$$R_{\hat{n}}(\theta) = \cos(\theta/2)\mathcal{I} - \mathrm{i}\sin(\theta/2)\hat{n}\cdot\vec{\sigma}, \tag{2.62}$$

where $\hat{n} = (n_x, n_y, n_z)$ defines the rotation axis, with $n_x^2 + n_y^2 + n_z^2 = 1$, and $\vec{\sigma} = (\sigma_x, \sigma_y, \sigma_z)$ denotes the Pauli matrices. As an example the state $|\psi\rangle = |0\rangle$ rotated around the y-axis by an angle of $\pi/2$ has the action

$$R_y(\pi/2)|0\rangle = \begin{pmatrix} \cos(\pi/4) & -\sin(\pi/4) \\ \sin(\pi/4) & \cos(\pi/4) \end{pmatrix}\begin{pmatrix} 1 \\ 0 \end{pmatrix} = \begin{pmatrix} 1/\sqrt{2} \\ 1/\sqrt{2} \end{pmatrix} = \frac{1}{\sqrt{2}}(|0\rangle + |1\rangle) = |+\rangle\,, \tag{2.63}$$

and analogously $R_y(-\pi/2) = |-\rangle$. $R_y(\pi/2)$ is also known as the Hadamard gate [15] H. Hadamard gates applied independently to a set of n qubits transform the state $|0\rangle^{\otimes n}$ into the superposition of all the possible string states in the composed Hilbert space.

2.2.2.2 Multi qubit gates

As mentioned in the previous section, single qubit gates are those that act upon the state of one qubit, leaving the others untouched. Multi qubit operations are gates that transform more than one qubit, or have more than one qubit involved.

As an important example of multi qubit operation, one can list the Controlled-NOT or CNOT operation. CNOT operation consists of a controlled operation, where two qubits are involved: the so called control and target qubits. The control qubit is the one in which the application of the transformation, in this case, the single qubit NOT gate, is performed upon the target qubit. The operation can be written as

$$|c\rangle\,|a\rangle \xrightarrow{\text{CNOT}} |c\rangle\,|c \oplus a\rangle\,, \tag{2.64}$$

with $c \oplus a$ indicating addition modulus 2 of bits c and a. For the set of two qubit states of the computational basis, $\{|00\rangle\,, |01\rangle\,, |10\rangle\,, |11\rangle\}$, where the first qubit is the control and the second is the target, CNOT has the action

$$\begin{cases} |00\rangle \xrightarrow{\text{CNOT}} |0\ 0 \oplus 0\rangle = |00\rangle\,, \\ |01\rangle \xrightarrow{\text{CNOT}} |0\ 0 \oplus 1\rangle = |01\rangle\,, \\ |10\rangle \xrightarrow{\text{CNOT}} |1\ 1 \oplus 0\rangle = |11\rangle\,, \\ |11\rangle \xrightarrow{\text{CNOT}} |1\ 1 \oplus 1\rangle = |10\rangle\,. \end{cases} \tag{2.65}$$

and can be represented in the matrix form as

$$\text{CNOT} \equiv \begin{pmatrix} 1 & 0 & 0 & 0 \\ 0 & 1 & 0 & 0 \\ 0 & 0 & 0 & 1 \\ 0 & 0 & 1 & 0 \end{pmatrix}. \tag{2.66}$$

The formalism is not only valid for the NOT operation, but for all general single qubit rotations. The control is added to the system whenever one needs an operation to be performed on one qubit, or a set of qubits, given that one condition is fulfilled. Another example of controlled operation, analogous to the CNOT case is the controlled Hadamard operation, that puts the target qubit in a superposition given the state of the control qubit

$$\begin{cases} |00\rangle \xrightarrow{\text{HC}} |0\rangle\,|+\rangle = \frac{1}{\sqrt{2}}\left(|00\rangle + |01\rangle\right), \\ |01\rangle \xrightarrow{\text{HC}} |0\rangle\,|-\rangle = \frac{1}{\sqrt{2}}\left(|00\rangle - |01\rangle\right), \\ |10\rangle \xrightarrow{\text{HC}} |1\rangle\,|+\rangle = \frac{1}{\sqrt{2}}\left(|10\rangle + |11\rangle\right), \\ |11\rangle \xrightarrow{\text{HC}} |1\rangle\,|-\rangle = \frac{1}{\sqrt{2}}\left(|10\rangle - |11\rangle\right), \end{cases} \tag{2.67}$$

and has the following matrix representation

$$HC = \begin{pmatrix} 1 & 0 & 0 & 0 \\ 0 & 1 & 0 & 0 \\ 0 & 0 & \frac{1}{\sqrt{2}} & \frac{1}{\sqrt{2}} \\ 0 & 0 & \frac{1}{\sqrt{2}} & \frac{-1}{\sqrt{2}} \end{pmatrix}. \tag{2.68}$$

It is also possible to have gates with more than two qubits involved. One example of this is the 3-qubit Toffoli gate. This operation transforms the target qubit, conditioned to the states of two control qubits. In this case, the target qubit is flipped whenever the states of both control qubits are set to $|1\rangle$, and left untouched otherwise. The Toffoli gate has the matrix representation

$$\text{TOFFOLI} = \begin{pmatrix} 1 & 0 & 0 & 0 & 0 & 0 & 0 & 0 \\ 0 & 1 & 0 & 0 & 0 & 0 & 0 & 0 \\ 0 & 0 & 1 & 0 & 0 & 0 & 0 & 0 \\ 0 & 0 & 0 & 1 & 0 & 0 & 0 & 0 \\ 0 & 0 & 0 & 0 & 1 & 0 & 0 & 0 \\ 0 & 0 & 0 & 0 & 0 & 1 & 0 & 0 \\ 0 & 0 & 0 & 0 & 0 & 0 & 0 & 1 \\ 0 & 0 & 0 & 0 & 0 & 0 & 1 & 0 \end{pmatrix}. \tag{2.69}$$

2.2.3 Quantum circuits

Quantum circuits are diagram representations of sequences of logic operations performed on a set of qubits. The circuit is composed of wires, which carry the information contained within the qubit states from left to right, and the gates are represented by boxes on the wires corresponding to the qubits they must act on. The state of the composed system is given by the tensor product of all the components at any specific point of the circuit. The employment of quantum circuits turns out to be a convenient tool to represent quantum algorithms, that sometimes can make use of several single- and multi qubit gates and controlled operations, making matrix representations extensive.

To illustrate a simple case of a quantum circuit, we represent the SWAP operation, which consists in an operation between two qubits that has the effect of swapping the information between one another. This gate has the logic action of

$$|a, b\rangle \xrightarrow{\text{SWAP}} |b, a\rangle\,, \tag{2.70}$$

that can be decomposed into the application of three CNOT operations between the two qubits of the system, acting in alternate times as control and target. The circuit is represented in figure 2.

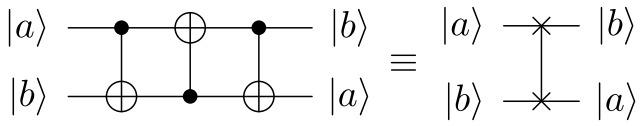

Figure 2 – Circuit representation of the SWAP gate, that swaps the information between two qubits of a composed system. On the left, the decomposition of the gate into three CNOT operations is presented, and on the right, the simplified representation. The black circles on the wires mark the control qubit of each CNOT operation indicated by $\oplus$ acting on the target qubit.

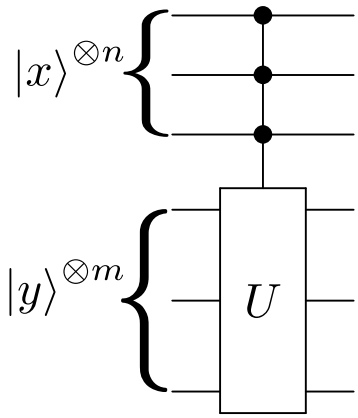

Figure 3 – Circuit representation of an operation that takes a set of n control qubits, applied to a set of m target qubits. The composed states are here denoted, for the sake of simplicity, by $|x\rangle^{\otimes n}$ and $|y\rangle^{\otimes m}$ to illustrate the dimension of the Hilbert spaces of control and targets, respectively.

It is also possible to have multi controlled operations, acting on a multi qubit state. These kind of operations are controlled by more than one qubit, and acts also in a set of qubits. Although its matrix representation or Dirac notation can be extensive, this class of operation has an intuitive form in the circuit representation of quantum algorithms. A case of multi controlled qubit operation is illustrated on figure 3, where a hypothetical case of n controls are applied to m targets.

2.2.4 Complexity aspects of quantum algorithms

There are different classes of computational complexity. Among them, one can list **P** (deterministic polynomial time) and **NP** (non-deterministic polynomial time). The **P** class consists of problems that can be solved within a polynomial quantity of time steps or operations. Problems within **NP** are those in which solutions can be verified in a polynomial quantity of operations. One example of problem from **NP** class is the factorization of integers, that can be rapidly verified, but not executed [15]. A broader class of problems is the so called **PSPACE**, composed by problems that can be solved with a limited amount of resources, but with no upper limit in time. The study of complexity classes is not a completely closed subject in terms of knowledge or answered questions,

and it is not the objective of this work. Fundamental discussions about the topic can be found in [15].

One can divide the complexity aspects involved in solving computational tasks in two different categories:

- Space: Space aspects take into account the required physical resources to solve the problem in question, in analogy to the hardware in classical computers. This aspect within quantum computation is represented by the number of qubits required to perform a task.
- Time: Time aspects consist into the number of operations that must be performed in order to get a specific task done. This aspect is often mentioned in terms of number of steps, which translate in number of operations executed upon the qubits part of the complete system under consideration.

Computational complexity is denoted by the asymptotic notation, which consists in

- "Big O" $O(\cdot)$: indicates the upper limit for complexity aspects in a given problem. It is used to indicate the worst case scenario for computational complexity.
- "Big Omega" $\Omega(\cdot)$: the opposite of $O(\cdot)$, indicates the lower limit for complexity, consisting in the cases where the number of operations or space complexity is the minimum.
- "Big Theta" $\Theta(\cdot)$: employed when a circuit or function behaves asymptotically in the same manner as other function or circuit: $f(x)$ is $\Omega(g(x))$ if $f(x)$ is $O(g(x))$ AND $f(x)$ is $\Omega(g(x))$.

2.2.5 Quantum algorithms

A quantum algorithm consists of a defined sequence of steps that must be executed to complete a determined task, employing quantum mechanical systems and operations. Different quantum algorithms have been developed to perform various kinds of tasks, for example database search [16], number factoring [17], solving linear systems [18], ordinary and partial differential equations [19, 20, 21]. The properties and resources of quantum mechanics, as superposition and entanglement, result in different conditions regarding how computational tasks are done, and under some circumstances, can present quantum advantage [9, 22, 23].

One of the features of quantum computation is the so called quantum parallelism [15]. Parallelism is a feature of quantum systems that allows one to calculate several values

for a given function f employing one circuit. Generally speaking, it is possible to obtain values for the function $f(x)$ for all values of x simultaneously with a reduced amount of time steps.

As a simple example of parallelism, we can assume a function $f(x) : \{0,1\} \to \{0,1\}$. A simple algorithm to calculate $f(x)$ using a circuit consists of employing two qubits and a transformation that performs the task

$$|x, y\rangle \to |x, y \oplus f(x)\rangle \,. \tag{2.71}$$

Hence, if one has $|y\rangle = |0\rangle$, after the transformation that calculates $f(x)$, $|y\rangle$ will then be found in the state $|f(x)\rangle$. We can assume, for example, that the first qubit is prepared in the superposition state $|x\rangle = 1/\sqrt{2}\,(|0\rangle + |1\rangle)$, which can be obtained by the initialization of $|x\rangle = |0\rangle$, followed by the application of a Hadamard gate H. The composite system then is given by $|\Psi\rangle = |x\rangle \otimes |y\rangle = 1/\sqrt{2}\,(|00\rangle + |10\rangle)$. The transformation U acts on $|\Psi\rangle$, leaving the system in the configuration

$$U\,|\Psi\rangle = \frac{1}{\sqrt{2}}\,(|0\rangle\,|f(0)\rangle + |1\rangle\,|f(1)\rangle)\,. \tag{2.72}$$

Therefore the final state of the system is left in a superposition that contains information about values of f calculated upon all points of the domain. However one must consider that although all values were obtained with just one circuit, the circuit itself might consist of an independent algorithm, with associated complexity aspects that might depend on the function f itself. The fundamental difference is that in the quantum case all the tasks can be done applying the transformation U on the superposition $|\Psi\rangle$. Naturally, the given example for two qubits can be also generalized for n qubits through the following algorithm:

1 Initially, a system of $n+1$ qubits must be prepared in the configuration $|\psi_1\rangle = |0\rangle^{\otimes n}\,|0\rangle$;

2 Hadamard operations are applied independently upon the set of n qubits, leaving the composite system in the configuration $|\psi_2\rangle = H^{\otimes n}\,|\psi_1\rangle = |+\rangle^{\otimes n}\,|0\rangle$;

3 The transformation U is then applied to the system performing the operation $|x, y\rangle \to |x, y \otimes f(x)\rangle$. The state $|x\rangle$ in this case corresponds to the superposition $|x\rangle = 1/\sqrt{(2^n)}\sum_\gamma |\gamma\rangle$, with γ standing for each of the n-bit strings. After U the state of the system is then given by

$$|\psi_3\rangle = U\,|+\rangle^{\otimes n}\,|0\rangle = \frac{1}{\sqrt{2^n}}\sum_\gamma |\gamma\rangle\,|f(\gamma)\rangle\,. \tag{2.73}$$

Despite of the useful parallelism features of quantum computation, it is worth noticing that, after the transformation U, the system is left in a $n+1$-dimensional quantum superposition, which means that after the algorithm is completed, a measurement performed on the system will collapse the wavefunction to a particular state,

$$|\psi_f\rangle = |x'\rangle\,|f(x')\rangle\,, \tag{2.74}$$

where x' represents the measurement outcome. Therefore, though parallelism is an intrinsic feature of quantum computation, the collapse of the wavefunction brings one to the discussion of the access of information after calculation. For the quantum parallelism to present some advantage over classical systems, it becomes necesssary to be able to recover all values of $f(x)$ in an efficient manner, since the information is already within the superposition given by $|\psi_3\rangle$.

Although the collapse of the wavefunction for the quantum system introduces a degree of difficulty in the readout process of outcomes for quantum algorithms, it is theoretically possible to obtain global properties of the function f calculated via the transformation U. An algorithm that aims for this task is the so called Deutsch algorithm, which combines properties of parallelism and interference. The algorithm consists in the following steps:

1 A system of two qubits is initialized in the state $|\psi_1\rangle = |0\rangle\,|0\rangle$;

2 A NOT gate is applied on the second qubit, transforming the state into $|\psi_2\rangle = |0\rangle\,|1\rangle$;

3 Two independent Hadamard gates are applied to the qubits, and the transformed state $|\psi_3\rangle = H^{\otimes 2}\,|\psi_2\rangle = |+\rangle\,|-\rangle$;

4 The transformation U is applied to the system, which is left in the following superposition

$$|\psi_4\rangle = \frac{1}{2}\left(|0\rangle\,|0\oplus f(0)\rangle - |0\rangle\,|1\oplus f(0)\rangle + |1\rangle\,|f(1)\rangle - |1\rangle\,|1\oplus f(1)\rangle\right), \tag{2.75}$$

which can be also written in a compact form

$$|\psi_4\rangle = \frac{1}{\sqrt{2}}\,|x\rangle\left(|0\oplus f(x)\rangle - |1\oplus f(x)\rangle\right), \tag{2.76}$$

given $|x\rangle = \frac{1}{\sqrt{2}}\left(|0\rangle + |1\rangle\right)$.

The function f can have one output bit, either 0 or 1. If $f(x) = 0$,

$$|\psi_4\rangle = \frac{1}{\sqrt{2}}\,|x\rangle\left(|0\rangle - |1\rangle\right) = (-1)^0\,|x\rangle\,|-\rangle\,, \tag{2.77}$$

and if $f(x) = 1$,

$$|\psi_4\rangle = \frac{1}{\sqrt{2}} |x\rangle (-|0\rangle + |1\rangle) = (-1)^1 |x\rangle |-\rangle , \tag{2.78}$$

and therefore the state can be written as

$$|\psi_4\rangle = (-1)^{f(x)} |x\rangle |-\rangle . \tag{2.79}$$

As one can see from eq. (2.79), when $f(0) = f(1)$, the output states only differ by a global phase factor $(-1)^{f(x)}$, for a given value of $f(x)$. Now one must analyze the case where $f(0) \neq f(1)$.

- $f(0) = 0$, $f(1) = 1$, then

$$|\psi_4\rangle = |-\rangle |-\rangle , \tag{2.80}$$

- $f(0) = 1$, $f(1) = 0$, then

$$|\psi_4\rangle = - |-\rangle |-\rangle . \tag{2.81}$$

which means in general that when $f(0) \neq f(1)$ one has $|\psi_4\rangle = \pm |-\rangle |-\rangle$, and one can write the state $|\psi_4\rangle$ as

$$|\psi_4\rangle = \begin{cases} \pm |+\rangle |-\rangle , & \text{if } f(0) = f(1), \\ \pm |-\rangle |-\rangle , & \text{if } f(0) \neq f(1). \end{cases} \tag{2.82}$$

Lastly one applies a Hadamard gate upon the first qubit, and obtain

$$H |\psi_4\rangle = |\psi_5\rangle = \begin{cases} \pm |0\rangle |-\rangle , & \text{if } f(0) = f(1), \\ \pm |1\rangle |-\rangle , & \text{if } f(0) \neq f(1). \end{cases} \tag{2.83}$$

Now, if $f(0) = f(1)$, one has $f(0) \oplus f(1) = 0$, and on the other hand if $f(0) \neq f(1)$, $f(0) \oplus f(1) = 1$. Under these conditions, one can write eq. (2.83) as

$$|\psi_5\rangle = \pm |f(0) \oplus f(1)\rangle |-\rangle . \tag{2.84}$$

Therefore, it becomes possible to obtain a global property of the function, $f(0) \oplus f(1)$ with only one implemented circuit. In the classical counterpart, this property would require two independent calculations, $f(0)$ and $f(1)$. This also differs from the case without interference, where the final state was obtained as $|\psi\rangle = 1/\sqrt{2}(|0\rangle |f(0)\rangle + |1\rangle |f(1)\rangle)$, where measurements are mutually exclusive, with probability of $\left|1/\sqrt{2}\right|^2 = 1/2$ for each outcome.

2.2.6 Measurement and retrieval of information from quantum states

It is possible to determine the state of a bit, given a generic process to access information, which can be either in state 0 or 1. In the case of quantum computation, this process must necessarily involve measurements, which consist on the manipulation and operations done upon the physical system itself. This measurement process, as mentioned before, collapses the wavefunction, and the measurement outcome in this case represents one of the several possibilities, depending on the dimension of the system under consideration.

Formally, to retrieve the encoded information provided by a quantum state, it is necessary to have an ensemble of identically prepared systems. This comes from the fact that there is no measurement or set of measurements, described by observables M that can distinguish between non-orthogonal states, such as $|0\rangle$ and $|-\rangle$, since $\langle 0|-\rangle \neq 0$. Therefore, one must be able to perform projective measurements in different directions or bases to reconstruct the density matrix that represents the state of the full system [24]. In particular, the set of matrices $\{\mathcal{I}, X, Y, Z\}$ form an orthogonal set of operators with respect to the Hilbert-Schmidt inner product [15], and the density matrix can then be expanded as

$$\rho = \mathrm{Tr}(\rho X)X + \mathrm{Tr}(\rho Y)Y + \mathrm{Tr}(\rho Z)Z + \mathrm{Tr}(\rho)\mathcal{I}. \tag{2.85}$$

As each of the factors $\mathrm{Tr}(\rho O)$ have statistical interpretation as averages of observables, several measurements are necessary to obtain correct estimations. For a set of m measurements, a set of outcomes $\{O_0, O_1, \ldots, O_{m-1}\}$ is obtained, such that

$$\mathrm{Tr}(\rho O) = \frac{1}{m}\sum_{j=0}^{m-1} O_j. \tag{2.86}$$

In particular, the availability of several identical copies of ρ is referred to as query complexity. In the case where the state represents the output solution of a problem solved by a quantum algorithm, ρ can only be obtained with the full implementation of the algorithm itself, which involves all the space and time aspects mentioned before.

The process of quantum state tomography can be performed under different conditions, protocols and physical systems [25, 26, 27, 28, 29]. The fact that solutions might be encoded within the probability amplitudes of the output wavefunction [19, 21, 18] makes the density matrix reconstruction a tool of fundamental importance for the complete knowledge of the solution, and quantum algorithm implementations frequently depend of this process [19, 30]. However, the study of quantum algorithms, due to the large dimensions of the involved Hilbert spaces, and considering that the determination of the amplitudes scale exponentially with its dimensions [30], it is considered that the simpler alternative is to obtain properties of the solution, represented by observables specially defined previously

for these ends [18, 31, 30], represented by $\langle\psi|M|\psi\rangle$. The mathematical structure of the operators M is specific to the problem under consideration and the information one must obtain from the output states. This query complexity therefore adds an additional layer to the complexity of implementation of a quantum algorithm itself, that must be considered in the case of applying quantum computers to solve any type of problems.

2.3 Two-photon interference from a quantum dot cascade source

In this section, we studied the interference properties of photons emitted by a quantum dot. In particular, the quantum dot is driven from the ground state to the biexciton state using a two-photon excitation process, upon which it would emit a photon pair in a cascade. The time-ordered nature of the cascade emission implies the existence of temporal correlations [32] and time-energy entanglement [33], however quantum dots such as polarization entanglement [34], time-energy entanglement [35, 33] and hyperentanglement [36]. Although photons are suitable for applications in quantum information through encoding information in its degrees of freedom, their low interaction nature imposes difficulties. The Hong-Ou-Mandel phenomenon is a quantum interference effect, originally demonstrated by Chung Ki Hong, Zheyu Ou, and Leonard Mandel, in 1987 [37], and constitutes a mechanism that enables two-photon interference, therefore the interaction between photons. The HOM effect takes place when two photons impinge at two distinct ports of a beam splitter, where the photons can interfere depending on their degree of distinguishability and spatio-temporal properties. The interaction introduced by the HOM interference has many applications, such as entanglement swapping [38], quantum teleportation [39], photonic circuits [40], among others. In this chapter, we introduce the emission process and the theoretical basis for the interference visibility calculation, introduced by a description of the HOM interference phenomenon. To calculate the two-photon correlations and interference properties, we employ the sensor method [2], which constitutes a practical tool for calculation of frequency- and time-resolved photon-photon correlations.

2.3.1 Hamiltonian and excitation process

The quantum dot is modelled as a three-level system, with ground ($|g\rangle$), exciton ($|x\rangle$) and biexciton ($|b\rangle$) energy levels [41]. The excitation of the system takes place by driving a two-photon excitation from the ground ($|g\rangle$) to the biexciton ($|b\rangle$) state through a virtual level, detuned from the exciton state by Δ_x. A schematic of the system is given in Figure 4.

The excitation pulse is assumed to have a Gaussian profile and frequency ω_L,

$$\Omega(t) = \Omega_0 \mathrm{e}^{-2\log(2)\left(\frac{t-t_0}{\sigma}\right)^2}. \tag{2.87}$$

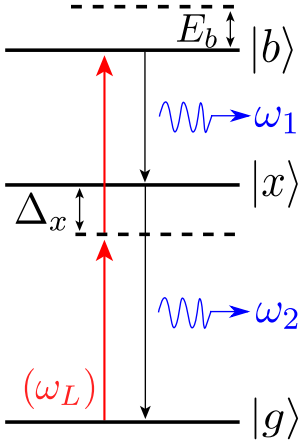

Figure 4 – Schematic representation of the three level system. The excitation pulse of frequency ω_L couples the ground and biexciton states via a virtual level, detuned from the exciton level by Δ_x. The emmitted photons of frequencies ω_1 and ω_2 correspond to the $|b\rangle \rightarrow |x\rangle$ and $|x\rangle \rightarrow |g\rangle$ transitions, respectively.

where Ω_0 represents the Rabi frequency. The pulse peak is located at $t = t_0$ and its width is σ. The Hamiltonian that governs the dynamics of the three level system can be written as [41]

$$H_e = \omega_x \sigma_{xx} + \omega_b \sigma_{bb} + \frac{\Omega(t)}{2}\left(\mathrm{e}^{-\mathrm{i}\omega_L t} + \mathrm{e}^{\mathrm{i}\omega_L t}\right)(\sigma_{gx} + \sigma_{xb} + \mathrm{h.c.})\,, \tag{2.88}$$

where ω_x and ω_b are the frequencies of the exciton and biexciton states, respectively. The operators $\sigma_{ij} = |i\rangle\langle j|$ account for the transitions $|g\rangle \rightarrow |x\rangle$ and $|x\rangle \rightarrow |b\rangle$. Once the excitation is completed, the decay takes place via a cascade emission process. A photon pair is generated as a result, with frequencies denoted as ω_1 and ω_2. The emissions are temporally ordered, such that the biexciton photon (ω_1) preceeds the exciton one. The decay rates of the system are associated with the respective lifetimes of the corresponding internal states. These are denoted by τ_b and τ_x, for the biexciton and exciton states, respectively.

2.3.2 Sensor method

The sensor method is a tool to calculate frequency- and time-resolved correlations [2]. The method has been applied to compute correlation functions in a variety of systems [42, 43], having the advantage of computing N-photon correlations for arbitrary time delays and frequency intervals, making it suitable for the application on any open quantum system.

The method consists of coupling of two two-level systems, which behave as sensors, to the three-level emitter. Each sensor is made resonant to one of the emission frequencies of the three-level system. This translates to the addition of extra terms to the Hamiltonian

given by eq. (2.88). The sensor contribution to the Hamiltonian can be written as

$$H_s = \sum_{j=1}^{2} \left\{ \omega_j \xi_j^\dagger \xi_j + g \left[\left(\sigma_{xb} + \sigma_{gx} \right) \xi_j^\dagger + \text{h.c.} \right] \right\}, \tag{2.89}$$

where $\xi_j^\dagger$ (ξ_j) and ω_j represent the creation (annihilation) operator and the resonance frequency for sensors $j = 1, 2$. Given that the emissions eventually occur in free space, we assume that the linewidth κ_j associated with each of the sensors is broadband ($\kappa \gg 1$). The coupling strengths (g) associated with the sensors are made small, satisfying $g \ll \sqrt{\kappa\Gamma/2}$ [2], where Γ represents the spontaneous decay rates, to prevent the introduction of back-action into the main system. The sensor method has been previously developed and utilized for the investigation of photon-photon correlations in various physical systems. Moreover, no additional assumptions are imposed on the system, and the correlation functions obtained with the sensor operators correspond to the correlations in emission [2]. We employ and demonstrate the applicability of the sensor method to investigate time-resolved correlations, as well as to model the emission and two-photon interference of photons emitted as a part of the biexciton-exciton cascade.

The complete Hamiltonian to describe the full system (emitter + sensors) can be written as $H_e + H_s$, and reads

$$\begin{aligned} H = \omega_x \sigma_{xx} + \omega_b \sigma_{bb} + \frac{\Omega(t)}{2} \left(\mathrm{e}^{-\mathrm{i}\omega_L t} + \mathrm{e}^{\mathrm{i}\omega_L t} \right) \left(\sigma_{gx} + \sigma_{xb} + \text{h.c.} \right) \\ + \sum_{j=1}^{2} \left\{ \omega_j \xi_j^\dagger \xi_j + g \left[\left(\sigma_{xb} + \sigma_{gx} \right) \xi_j^\dagger + \text{h.c.} \right] \right\}. \end{aligned} \tag{2.90}$$

It is convenient to perform a unitary transformation to simplify the Hamiltonian and remove the complex time dependence. The transformation is defined by the operator $U_1 = \mathrm{e}^{-\mathrm{i}H_1 t}$, where H_1 is given as

$$H_1 = \left(\omega_L + \Delta_b \right) \sigma_{xx} + \left(2\omega_L + \Delta_b \right) \sigma_{bb} + \sum_{j=1}^{2} \omega_j \xi_j^\dagger \xi_j \tag{2.91}$$

with $\Delta_b = 2\omega_L - \omega_b$ being the detuning between the laser frequency and the two-photon resonance. The transformed Hamiltonian $H' = U_1^\dagger H_S U_1 - \mathrm{i} U_1^\dagger \frac{\partial U_1}{\partial t}$ is written as

$$\begin{aligned} H' = \left(\Delta_x - \Delta_b \right) \sigma_{xx} - 2\Delta_b \sigma_{bb} + \frac{\Omega(t)}{2} \left(\mathrm{e}^{-\mathrm{i}\Delta_b t} \sigma_{gx} + \sigma_{xb} + \text{h.c.} \right) \\ + g \sum_{j=1}^{2} \left[\left(\mathrm{e}^{-\mathrm{i}\Delta_b t} \sigma_{gx} + \sigma_{xb} \right) \xi_i^\dagger \mathrm{e}^{\mathrm{i}\Delta_i t} + \text{h.c.} \right], \end{aligned} \tag{2.92}$$

where $\Delta_i = \omega_i - \omega_L$ is defined as the sensor detuning. We applied the rotating wave approximation was applied, and terms that oscillate with double laser frequency $2\omega_L$ were dropped. The two-photon excitation is assumed to be resonant with the biexciton

frequency ω_b, resulting in $\Delta_b = 0$. The time dependence from the sensor operators can be removed by performing a second unitary transformation $U_2 = \mathrm{e}^{-\mathrm{i}H_2 t}$, with H_2 defined as

$$H_2 = \sum_{j=1}^{2} \alpha_i \xi_i^\dagger \xi_i, \tag{2.93}$$

where the coefficients α_i are to be defined. The result of the second transformation applied on H' is

$$\begin{aligned} H_I = -\alpha_1 \xi_1^\dagger \xi_1 - \alpha_2 \xi_2^\dagger \xi_2 + (\Delta_x - \Delta_b)\,\sigma_{xx} - 2\Delta_b \sigma_{bb} + \frac{\Omega(t)}{2}\left(\sigma_{gx} + \sigma_{xb} + \mathrm{h.c.}\right) \\ + g \sum_{i=1}^{2} \left[\left(\sigma_{gx} + \sigma_{xb}\right) \xi_i^\dagger \mathrm{e}^{\mathrm{i}(\Delta_i + \alpha_i)t} + \mathrm{h.c.} \right], \end{aligned} \tag{2.94}$$

which becomes time independent under the following conditions

$$\begin{cases} \Delta_1 + \alpha_1 = 0 \Rightarrow -\alpha_1 = \Delta_1 \\ \Delta_2 + \alpha_2 = 0 \Rightarrow -\alpha_2 = \Delta_2, \end{cases} \tag{2.95}$$

and the time independent Hamiltonian reads

$$\begin{aligned} H_I = \Delta_1 \xi_1^\dagger \xi_1 + \Delta_2 \xi_2^\dagger \xi_2 + (\Delta_x - \Delta_b)\,\sigma_{xx} - 2\Delta_b \sigma_{bb} \\ + \frac{\Omega(t)}{2}\left(\sigma_{gx} + \sigma_{xb} + \mathrm{h.c.}\right) + \epsilon \sum_{i=1}^{2} \left[\left(\sigma_{xb} + \sigma_{gx}\right) \xi_i^\dagger + \mathrm{h.c.} \right]. \end{aligned} \tag{2.96}$$

The sensor detunings Δ_1 and Δ_2 can be adjusted to be resonant with the frequencies of the emmitted photons, corresponding to the transitions $|b\rangle \to |x\rangle$ and $|x\rangle \to |g\rangle$. In this case, one must introduce

$$\begin{aligned} \omega_1 &= \omega_b - \omega_x \\ \omega_1 - \omega_L &= (\omega_b - \omega_x) - \omega_L + \omega_L - \omega_L \\ \Delta_1 &= -(\Delta_b + \Delta_x), \end{aligned} \tag{2.97}$$

for sensor 1, and

$$\begin{aligned} \omega_2 &= \omega_x - \omega_g \\ \omega_2 - \omega_L &= \omega_x - \omega_L \\ \Delta_2 &= \Delta_x. \end{aligned} \tag{2.98}$$

for sensor 2.

The dynamics of the system is solved using the ensemble master equation,

$$\dot{\rho} = -\mathrm{i}[H_I, \rho] + \sum_k \mathcal{L}_k \rho, \tag{2.99}$$

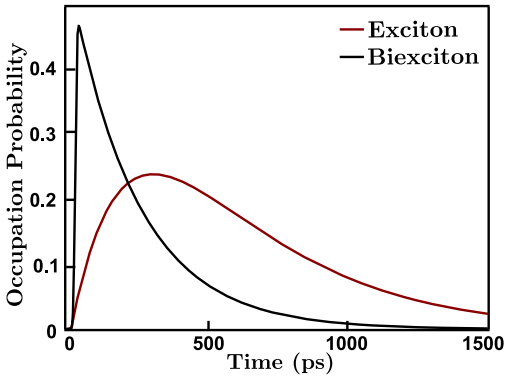

Figure 5 – Occupation probabilities as a function of time for biexciton and exciton states, simulated via the master equation.

considering the system to be at the ground state at $t = 0$. The dissipation mechanisms are taken into account by means of the Lindblad operators $\mathcal{L}_k$, that are connected to spontaneous decay, dephasing and sensor linewidth. For spontaneous decay, one has

$$\mathcal{L}_1\rho = \frac{\Gamma_b}{2}\left[2\sigma_{xb}\rho\sigma_{xb}^\dagger - \sigma_{xb}^\dagger\sigma_{xb}\rho - \rho\sigma_{xb}^\dagger\sigma_{xb}\right], \tag{2.100}$$

$$\mathcal{L}_2\rho = \frac{\Gamma_x}{2}\left[2\sigma_{gx}\rho\sigma_{gx}^\dagger - \sigma_{gx}^\dagger\sigma_{gx}\rho - \rho\sigma_{gx}^\dagger\sigma_{gx}\right], \tag{2.101}$$

with $\Gamma_{x,b} = 1/\tau_{x.b}$ represents the decay rate for each of biexciton and exciton states. The dephasing related to both transitions are modeled by [41],

$$\mathcal{L}_3\rho = \frac{\Gamma_{\rm db}}{2}\left[2\sigma_{\rm db}\rho\sigma_{\rm db}^\dagger - \sigma_{\rm db}^\dagger\sigma_{\rm db}\rho - \rho\sigma_{\rm db}^\dagger\sigma_{\rm db}\right], \tag{2.102}$$

$$\mathcal{L}_4\rho = \frac{\Gamma_{\rm db}}{2}\left[2\sigma_{\rm dx}\rho\sigma_{\rm dx}^\dagger - \sigma_{\rm dx}^\dagger\sigma_{\rm dx}\rho - \rho\sigma_{\rm dx}^\dagger\sigma_{\rm dx}\right], \tag{2.103}$$

with $\sigma_{\rm db} = \sigma_{bb} - \sigma_{xx}$ and $\sigma_{\rm dx} = \sigma_{xx} - \sigma_{gg}$. The factors $\Gamma_{\rm db,dx} = (1/\tau_{\rm db,dx})$ are the dephasing rates of biexciton and exciton, respectively. The last Lindblad terms correspond to the sensor linewidths, and can be written as

$$\mathcal{L}_j\rho = \frac{\kappa_j}{2}\left(2\xi_j\rho\xi_j^\dagger - \xi_j^\dagger\xi_j\rho - \rho\xi_j^\dagger\xi_j\right), \tag{2.104}$$

with $j = 1, 2$. As the emissions into free space are considered, the sensor are considered to have a broad linewidth, with $\kappa_j \gg 1$. The population of the biexciton state is defined by

$$P_b = \Gamma_b \int_0^\infty \langle\sigma_{bb}(t)\rangle \, {\rm d}t, \tag{2.105}$$

and is adjusted through Ω_0 to $P_b = 0.5$. The occupation probabilities for biexciton and exciton states as a function of time are represented in figure 6, obtained by the expectation values $\langle\sigma_{bb}(t)\rangle$ and $\langle\sigma_{xx}(t)\rangle$.

2.3.3 Two-photon interference

The radiation field in each of the input ports of the beamsplitter is described by the annihilation (creation) operator ξ_j ($\xi_j^\dagger$), with $j = 1, 2$, each with specific and potentially

distinguishable degrees of freedom, such as polarization, and also temporal properties, characterized by their lengths and arrival times at the beamsplitter. Considering the case of a $50:50$ beamsplitter, which means that 50% of the incident light is transmitted, and the other 50% is reflected, the beam splitter acts as a unitary transformation upon the field operators, and those are transformed by [44]

$$\begin{aligned}\chi_1 &= \frac{1}{\sqrt{2}}\left(\xi_1 + \xi_2\right), \\ \chi_2 &= \frac{1}{\sqrt{2}}\left(\xi_1 - \xi_2\right),\end{aligned} \tag{2.106}$$

where χ_j operators denote output modes of the radiation after the beam splitter. More specifically, the modes containing one photon each can be described as the quantum state

$$\left|\Psi_{\text{in}}\right\rangle_{12} = \xi_1^\dagger \xi_2^\dagger \left|0\right\rangle_1 \left|0\right\rangle_2, \tag{2.107}$$

where again the subscripts denote the distinct modes of the radiation. After interacting at the beamsplitter, the state containing one photon each will be described in terms of the operators χ_j as $\chi_1^\dagger \chi_2^\dagger \left|0\right\rangle_1 \left|0\right\rangle_2$, and can be written in terms of the input modes using the transformation in eq. (2.106) as

$$\left|\Psi_{\text{out}}\right\rangle_{12} = \frac{1}{2}\left(\xi_1^\dagger \xi_1^\dagger - \xi_1^\dagger \xi_2^\dagger + \xi_2^\dagger \xi_1^\dagger - \xi_2^\dagger \xi_2^\dagger\right)\left|0\right\rangle_1 \left|0\right\rangle_2. \tag{2.108}$$

At this point distinguishability plays a key role in the phenomenon, which can be seen with a very simple analysis. If we consider, for example, photons from modes 1 and 2 have horizontal and vertical polarization respectively, they are distinguishable. In this case, we denote the transformation in eq. (2.106) taking into account the polarization degree of freedom,

$$\begin{aligned}\chi_{1,H}(t) &= \frac{1}{\sqrt{2}}\left(\xi_{1,H} + \xi_{2,H}\right), \\ \chi_{2,V}(t) &= \frac{1}{\sqrt{2}}\left(\xi_{1,V} - \xi_{2,V}\right),\end{aligned} \tag{2.109}$$

and the output state is then

$$\left|\Psi_{\text{out}}\right\rangle_{12} = \frac{1}{2}\left(\xi_{1,H}^\dagger \xi_{1,V}^\dagger - \xi_{1,H}^\dagger \xi_{2,V}^\dagger + \xi_{1,V}^\dagger \xi_{1,H}^\dagger - \xi_{2,H}^\dagger \xi_{2,V}^\dagger\right)\left|0\right\rangle_1 \left|0\right\rangle_2, \tag{2.110}$$

which in terms of amplitudes is [44]

$$\begin{aligned}\left|\Psi_{\text{out}}\right\rangle_{12} = \frac{1}{2}(&\left|1;H,1;V\right\rangle_1 \left|0;H,0;V\right\rangle_2 - \left|1;H\right\rangle_1 \left|1;V\right\rangle_2 + \\ &\left|1;V\right\rangle_1 \left|1;H\right\rangle_2 - \left|0;H,0;V\right\rangle_1 \left|1;H,1;V\right\rangle_2),\end{aligned} \tag{2.111}$$

where the notation $\left|n;H,m;V\right\rangle_j$ indicates the presence of n photons of polarization H and m photons of polarization V in mode j. In this case there is no interference: the system has a probability of having two photons in either modes 1 and 2, given by the amplitudes

of the first and last terms $|1/2|^2 + |1/2|^2 = 1/2$, and also a coincidence probability, the scenario in which one photon is present in each mode of $1/2$, given by the two middle terms. In the indistinguishable scenario, where all degrees of freedom for both modes have the same properties, the polarization indexes can be dropped from eq. (2.111), the middle terms cancel out, and the output state can be obtained directly from eq. (2.108) as

$$|\Psi_{\text{out}}\rangle_{12} = \frac{1}{\sqrt{2}} \left(|2\rangle_1 |0\rangle_2 - |0\rangle_1 |2\rangle_2 \right). \tag{2.112}$$

In this case due to indistinguishability, the impinging photons interfere such that there is no coincidence events: detectors placed at the output ports of the beamsplitter would not click within a zero delay time between detections.

Besides polarization, it is also possible to analyze distinguishability in terms of other degrees of freedom, such as the times in which the two interfering photons impinge on the beamsplitter. In this case, the temporal properties are relevant to the analysis, as the degree of distinguishability will change if the wavepackets do not match in space. In the case of temporal distinguishability of single photons impinging on different ports of the beamsplitter, one can account for the interference between the paths evaluating the correlation functions for the coincidence events.

In general, one can describe the statistics of the output modes of the beamsplitter by means of intensity-intensity correlation functions [14]. Considering detection events at times t_1 and t_2, the statistics of the field is given in terms of the normally ordered correlation

$$G^{(2)}_{ij}(t_1, t_2) = \langle : n_i(t_1) n_j(t_2) : \rangle \,, \tag{2.113}$$

which accounts for auto- and cross-correlation for $i = j$ and $i \neq j$, respectively. One is interested in this case to quantify the cross-correlation between two independent modes of the field that impinge on the beamsplitter. The two modes are assumed to be independent, i.e. radiated by independent sources. Considering a time interval τ between the detection of the output ports, the cross-correlation can be evaluated through eq. (2.113) as [45]

$$\langle : n_1(t+\tau) n_2(t) : \rangle = \left\langle \chi_1^\dagger(t+\tau) \chi_2^\dagger(t) \chi_2(t) \chi_1(t+\tau) \right\rangle, \tag{2.114}$$

which in terms of the input operators is

$$\begin{aligned} \langle : n_i(t_1) n_j(t_2) : \rangle = \frac{1}{4} \Big\langle & \left(\xi_1^\dagger(t+\tau) - \xi_2^\dagger(t+\tau) \right) \left(\xi_1^\dagger(t) + \xi_2^\dagger(t) \right) \times \\ & \left(\xi_1(t) + \xi_2(t) \right) \left(\xi_1(t+\tau) - \xi_2(t+\tau) \right) \Big\rangle, \end{aligned} \tag{2.115}$$

from which terms with odd number of operators from the same mode such as $\left\langle \xi_i^\dagger \xi_i^\dagger \xi_i \xi_j \right\rangle$

vanish, yielding

$$G_{ij}^{(2)}(t,\tau) = \frac{1}{4}\left[\left\langle \xi_1^\dagger(t+\tau)\xi_1^\dagger(t)\xi_1(t)\xi_1(t+\tau)\right\rangle + \left\langle \xi_2^\dagger(t+\tau)\xi_2^\dagger(t)\xi_2(t)\xi_2(t+\tau)\right\rangle\right] + \frac{1}{4}\left[\left\langle \xi_1^\dagger(t+\tau)\xi_2^\dagger(t)\xi_2(t)\xi_1(t+\tau)\right\rangle + \left\langle \xi_2^\dagger(t+\tau)\xi_1^\dagger(t)\xi_1(t)\xi_2(t+\tau)\right\rangle\right] - \frac{1}{4}\left[\left\langle \xi_2^\dagger(t+\tau)\xi_1^\dagger(t)\xi_2(t)\xi_1(t+\tau)\right\rangle + \left\langle \xi_1^\dagger(t+\tau)\xi_2^\dagger(t)\xi_1(t)\xi_2(t+\tau)\right\rangle\right]. \tag{2.116}$$

The assumption that the fields are radiated by independent sources, and thus not correlated by any means makes it possible to write the cross-correlation terms in eq. (2.116) as products of two two-time autocorrelation functions [45], which can be written as

$$G_{12}^{(2)}(t,\tau) = \frac{1}{4}\left[\left\langle \xi_1^\dagger(t+\tau)\xi_1^\dagger(t)\xi_1(t)\xi_1(t+\tau)\right\rangle + \left\langle \xi_2^\dagger(t+\tau)\xi_2^\dagger(t)\xi_2(t)\xi_2(t+\tau)\right\rangle\right] + \frac{1}{4}\left[\left\langle \xi_1^\dagger(t+\tau)\xi_1(t+\tau)\right\rangle\left\langle \xi_2^\dagger(t)\xi_2(t)\right\rangle + \left\langle \xi_2^\dagger(t+\tau)\xi_2(t+\tau)\right\rangle\left\langle \xi_1^\dagger(t)\xi_1(t)\right\rangle\right] - \frac{1}{4}\left[\left\langle \xi_2^\dagger(t+\tau)\xi_2(t)\right\rangle\left\langle \xi_1^\dagger(t)\xi_1(t+\tau)\right\rangle + \left\langle \xi_1^\dagger(t+\tau)\xi_1(t)\right\rangle\left\langle \xi_2^\dagger(t)\xi_2(t+\tau)\right\rangle\right]. \tag{2.117}$$

Rewriting eq. (2.117) in terms of two-time unnormalized intensity and amplitude correlations,

$$G_j^{(1)}(t,\tau) = \left\langle \xi_j^\dagger(t+\tau)\xi_j(t)\right\rangle, \tag{2.118}$$

$$G_{jj}^{(2)}(t,\tau) = \left\langle \xi_j^\dagger(t+\tau)\xi_j^\dagger(t)\xi_j(t)\xi_j(t+\tau)\right\rangle, \tag{2.119}$$

one can also rewrite the cross-correlation as

$$G_{12}^{(2)}(t,\tau) = \frac{1}{4}\left[G_{11}^{(2)}(t,\tau) + G_{22}^{(2)}(t,\tau)\right] + \frac{1}{4}\left[\left\langle \xi_1^\dagger(t+\tau)\xi_1(t+\tau)\right\rangle\left\langle \xi_2^\dagger(t)\xi_2(t)\right\rangle + \left\langle \xi_2^\dagger(t+\tau)\xi_2(t+\tau)\right\rangle\left\langle \xi_1^\dagger(t)\xi_1(t)\right\rangle - 2\,\mathrm{Re}\left(G_1^{(1)}(t,\tau)\right)^* G_2^{(1)}(t,\tau)\right]. \tag{2.120}$$

Integrating eq. (2.120) over t one obtains the correlation as a function of the time delay τ, $G_{\mathrm{HOM}}^{(2)}(\tau)$ [45]

$$G_{\mathrm{HOM}}^{(2)}(\tau) = \int_0^\infty G_{12}^{(2)}(t,\tau)\mathrm{d}t. \tag{2.121}$$

The correlation at zero delay can then be obtained by integrating over the time span of t and τ as

$$G_{\mathrm{HOM}}^{(2)}[0] = \int_{-\infty}^{\infty}\int_0^\infty G_{12}^{(2)}(t,\tau)\ \mathrm{d}t\ \mathrm{d}\tau, \tag{2.122}$$

where the limits $(-\infty,\infty)$ account for both positive and negative values of τ, given that one photodetection occurs at time t.

2.3.4 Monte Carlo wavefunction and postselection

The Monte Carlo wavefunction method [46] consists of determining single quantum trajectories that the evolution of the quantum system undergoes. Instead of obtaining

the density operator $\rho(t)$ as in the master equation solution, the method is based on the solution of the Schrödinger equation

$$\mathrm{i}\hbar\frac{\mathrm{d}\,|\Psi(t)\rangle}{\mathrm{d}t} = H_{\mathrm{nh}}\,|\Psi(t)\rangle\,. \tag{2.123}$$

The evolution is governed by the non-hermitian Hamiltonian H_{nh} defined as [46]

$$H_{\mathrm{nh}} = H_I - \frac{\mathrm{i}\hbar}{2}\sum_k C_k^\dagger C_k, \tag{2.124}$$

where C_k denotes the k-th to the collapse operator of the system composed of emitter and sensors, and H_I is the interaction Hamiltonian given in eq. (2.96). The imaginary terms present in eq. (2.124) cause a decrease of the norm of the state vector $|\Psi(t)\rangle$, such that $\||\psi(t_1)\rangle\| > \||\psi(t_2 > t_1)\rangle\|$.

The decrease of the norm of the state vector is used to trigger a transition of the system, corresponding to the collapse and renormalization of the wavefunction [46]

$$|\Psi(t)\rangle \to \frac{C_k\,|\Psi(t)\rangle}{\sqrt{\langle\Psi(t)|C_k^\dagger C_k|\Psi(t)\rangle}}. \tag{2.125}$$

To perform the simulation, a random number r_1 $(0 \leq r_1 \leq 1)$ is generated, and the time interval is discretized. For every time step, the norm of the state vector is calculated and numerically compared with r_1. A quantum jump takes place at $t = t_0$ when the condition $\||\Psi(t_0\rangle\| < r_1$. As a result, a set of N state vectors is obtained, each corresponding to a trajectory calculated in the time evolution. The correspondence with the ensemble master equation is achieved in the average

$$\rho(t) = \lim_{N\to\infty}\frac{1}{N}\sum_{j=1}^{N}|\Psi_j(t)\rangle\langle\Psi_j(t)|\,, \tag{2.126}$$

where $|\Psi_j(t)\rangle$ denotes the j-th simulated trajectory at time t.

For the computation of the postselected density matrix, a reduced set of trajectories is considered upon ensemble average represented in eq. (2.126).

2.3.5 Wavepacket reduction and time-energy entanglement

The cascaded nature of the system under consideration translates into a time-ordered emission of the photons. This temporal correlation was investigated by J. D. Franson, with the introduction of the concept of time-energy entanglement. The wavefunction for a photon pair pertaining to one cascade is given by [32]

$$\psi(t_b, t_x) = 2\sqrt{\Gamma_b\Gamma_x}\mathrm{e}^{-\Gamma_b t_b}\Theta(t_b)\mathrm{e}^{-\Gamma_x(t_x-t_b)}\Theta(t_x - t_b), \tag{2.127}$$

where t_b (t_x) denote the emission time and decay rate of the biexciton (exciton) state, and $\Theta(t)$ denotes the Heaviside function. The entanglement arises from the presence

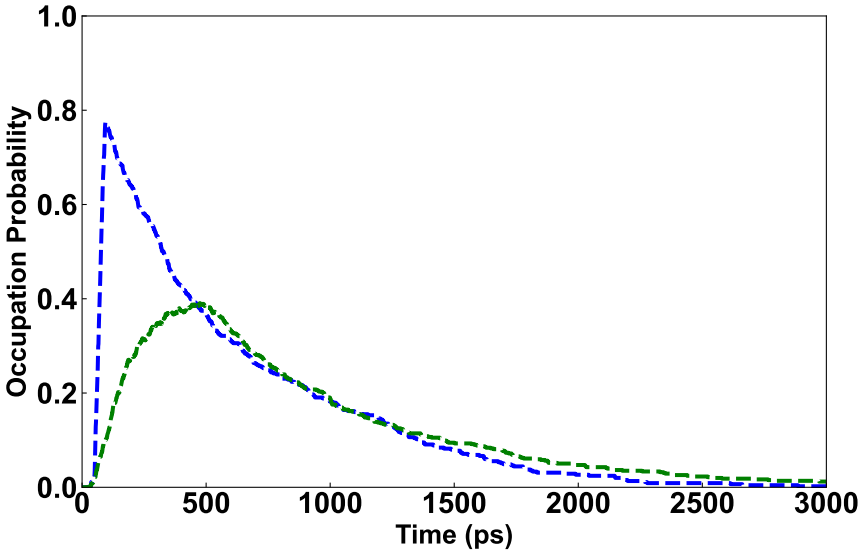

Figure 6 – Occupation probabilities as a function of time for biexciton and exciton states. The number of trajectories considered for the average is $N = 1000$.

of the factor $\Theta(t_x - t_b)$, which accounts for the time ordering of the emissions, with $\Theta(t_x - t_b) \neq 0 \Leftrightarrow tx > t_b$. The effect of this correlation can be observed by evaluating the state of one photon that pertains to one photon pair. Denoting the composite density matrix of the system as $\rho(t_b, t_x) = \psi^*(t_b, t_x)\psi(t_b, t_x)$, the reduced density matrix corresponding to one photon can be obtained by taking the partial trace over either of the temporal degrees of freedom. Denoting the exciton reduced density matrix by ρ_x, obtained by tracing over the biexciton emission time t_b, the quantity [32]

$$\mathrm{Tr}\left(\rho_x^2\right) = \frac{\Gamma_b}{\Gamma_b + \Gamma_x} \tag{2.128}$$

represents the purity of the exciton photon, related to the decay rates Γ_b and Γ_x. The expression for the purity shows that the correlations between biexciton and exciton photons are strong when $\Gamma_x \gg \Gamma_b$. This corresponds to the case considered in the time-energy entanglement [47], where the uncertainty in the time difference of the emission events in the cascade is smaller compared to the uncertainties of individual emissions ($\tau_x \ll \tau_b$). On the other hand, $\Gamma_x \ll \Gamma_b$ ($\tau_x \gg \tau_b$) implies that the reduced density operator has a greater temporal purity, as $\mathrm{Tr}(\rho_x^2) \to 1$ as the ratio between lifetimes τ_b/τ_x becomes smaller.

To analyze the impact of the temporal correlations on the coherence and interference properties of the reduced single-photon state, a postselection framework was implemented. The concept consists of sampling the first photon of the cascade corresponding to the transition $|b\rangle \to |x\rangle$, into distinct temporal groups, separated by a time $t = t_0$. In this way, the postselected density matrix is constructed based on the biexciton photons whose emission time t_b is such that $t_b < t_0$. No restrictions are imposed on the exciton emission. The postselection scheme is illustrated in Figure 7. This postselection of the photon emissions virtually translates in an average reduction of the biexciton state lifetime, as

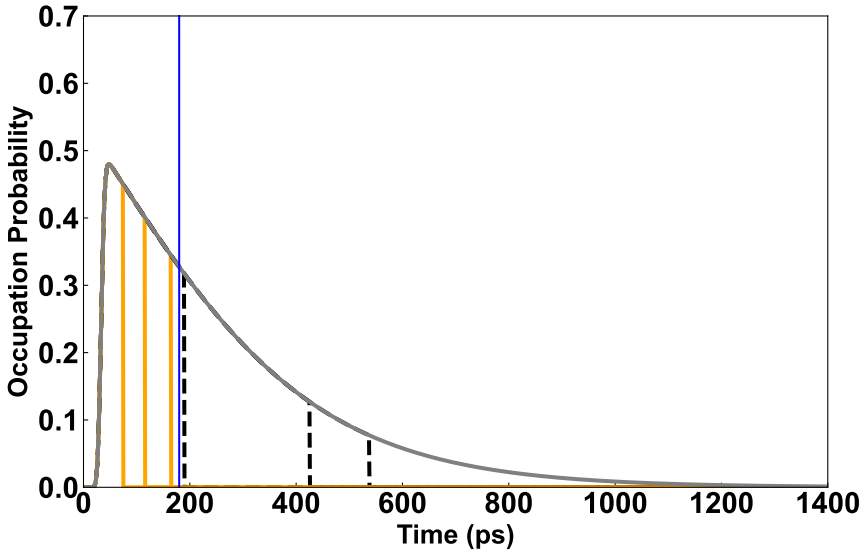

Figure 7 – Occupation probability for the biexciton state $|b\rangle$ as a function of time, simulated via Monte Carlo wavefunction method. The blue vertical line corresponds to the postselection condition, located at $t = 192$ps. The orange lines represent the trajectories in which the biexciton emission preceeds the postselection condition. The dashed black lines correspond to trajectories in which the biexciton emission does not satisfy the condition.

the postselected density matrix,

$$\rho_{PS}(t) \approx \frac{1}{N'} \sum_{j=1}^{N'<N} |\Psi_j(t)\rangle\langle\Psi_j(t)| \tag{2.129}$$

disregards emission events based on the postselection time window. The condition for increased purity, $\Gamma_x \ll \Gamma_b$, can be achieved through postselection by making $t_{PS} \ll \tau_x$. Simulated trajectories are illustrated on Figure 7. Figure 8 shows the theoretical results for Hong-Ou-Mandel interference visibility predicted theoretically. The experiment was conducted with quantum dot embedded in a micropillar structure [48], showing the effective action of the experimental postselection framework. The detailed experimental schemes, together with the experimental data is presented in [49].

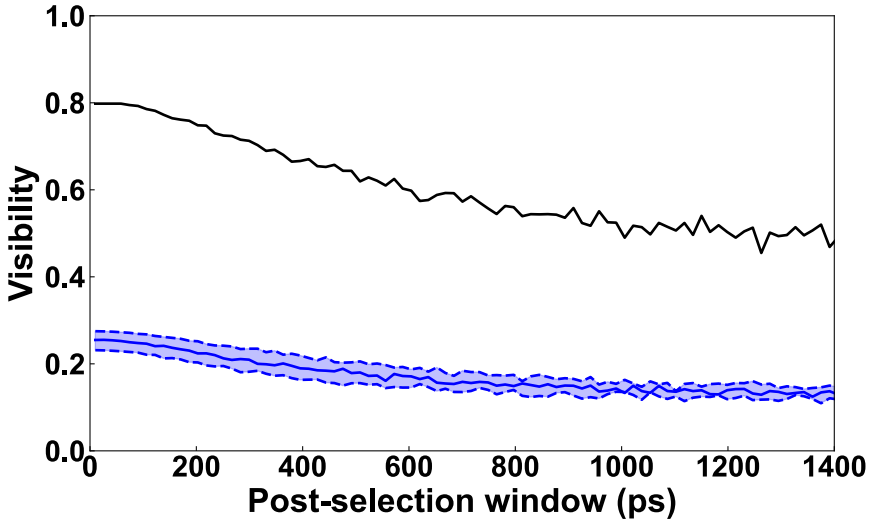

Figure 8 – Theoretical curves for the Hong-Ou-Mandel interference visibility as a function of the postselection time window. The black curve represents the no-dephasing case. The blue curve accounts for the scenario corresponding to the coherence times estimated theoretically. The light blue region represents the error with which the coherence times were determined.

3 Conclusion

In this thesis, we have reviewed the results achieved during the entire doctoral project, focused on quantum information and quantum computation. The results consist of two published and one submitted papers, each of which addressing a distinct topic regarding quantum information processing.

In the first work [4], we have investigated the mathematical properties of superpositions of two-mode squeezed states. In particular, we focused on two particular cases that take place under specific parameters, the even and odd EPR states. We presented a parameter relevant to quantifying and maximizing the entanglement between the two modes of the electromagnetic field, which shows the possibility of achieving higher efficiency in entanglement in entanglement generation compared to the two-mode squeezed EPR state. We motivate the application of even and odd EPR states for quantum metrology purposes. Through the concept of Quantum Fisher Information, we presented a quantitative analysis that motivates the use of these states for the implementation of phase insensitive quantum metrology.

The second work [50] addresses the complexity analysis of quantum algorithms. We point out that, although quantum algorithms might offer an improvement over their well established classical counterparts, the full implementation of a quantum algorithm for practical execution is often costly regarding the time and space complexity aspects. To provide a quantitative analysis, we have considered the computational complexity of information input, consisting of the preparation of the initial state for algorithmic processing, together with complexity of retrieving the output state, containing the relevant information about the task performed by the algorithm. We perform a detailed analysis regarding distinct architectures for quantum random access memory (qRAM) and quantum state tomography, combining the results of different approaches and indicating the alternatives that can lead to optimized complexity.

Finally, we presented a study regarding interference properties of photons emitted in cascaded processes [49]. We have employed the sensor method, described in the theoretical background, for the computation of correlation functions of photons pertaining to one cascade. The behavior of the Hong-Ou-Mandel interference visibility was quantified for both of the emitted photons under distinct coherence conditions, caractherized by the lifetimes of the internal states and the dephasing times relative to each of the transitions, and quantify the dephasing times correspondent to the system we study experimentally. To study the impact of postselection on HOM interference visibility, we implement a stochastic framework based on the Monte-Carlo wavefunction method. We present and

discuss the enhancement of visibility based on the length of the postselection time window. With this work, submitted to Physical Review Letters, we hope to provide a relevant discussion about the performance of cascaded sources and, indicating the way towards optimal performance.

We believe that this thesis provides a valuable collection of results in the field of quantum information and quantum computation, regarding to both basic and applied aspects of physics.

Bibliography

1 VILLAS-BOAS, C.; MOUSSA, M. One-step generation of high-quality squeezed and epr states in cavity qed. The European Physical Journal D-Atomic, Molecular, Optical and Plasma Physics, Springer, v. 32, n. 1, p. 147–151, 2005. Citado 4 vezes nas páginas 14, 17, 23, and 24.

2 VALLE, E. del et al. Theory of frequency-filtered and time-resolved n-photon correlations. Phys. Rev. Lett., American Physical Society, v. 109, p. 183601, Oct 2012. Citado 4 vezes nas páginas 16, 37, 38, and 39.

3 SCULLY, M. O.; ZUBAIRY, M. S. Quantum optics. [S.l.]: AAPT, 1999. Citado 2 vezes nas páginas 17 and 24.

4 CARDOSO, F. R. et al. Superposition of two-mode squeezed states for quantum information processing and quantum sensing. Phys. Rev. A, American Physical Society, v. 103, p. 062405, Jun 2021. Citado 2 vezes nas páginas 17 and 49.

5 EINSTEIN, A.; PODOLSKY, B.; ROSEN, N. Can Quantum-Mechanical Description of Physical Reality Be Considered Complete? Phys. Rev., American Physical Society, v. 47, p. 777, May 1935. Citado na página 17.

6 REID, M. D. et al. Colloquium: The einstein-podolsky-rosen paradox: From concepts to applications. Rev. Mod. Phys., American Physical Society, v. 81, p. 1727–1751, Dec 2009. Citado na página 17.

7 PIRANDOLA, S. et al. Advances in quantum teleportation. Nat. Photonics, Springer Science and Business Media LLC, v. 9, n. 10, p. 641–652, set. 2015. Citado na página 17.

8 TAKEDA, S.; FURUSAWA, A. Toward large-scale fault-tolerant universal photonic quantum computing. APL Photonics, AIP Publishing, v. 4, n. 6, 2019. Citado na página 17.

9 ZHONG, H.-S. et al. Quantum computational advantage using photons. Science, American Association for the Advancement of Science, v. 370, n. 6523, p. 1460–1463, 2020. Citado 2 vezes nas páginas 17 and 32.

10 SAKURAI, J. J.; COMMINS, E. D. Modern quantum mechanics, revised edition. [S.l.]: AAPT, 1995. Citado na página 18.

11 PEZZE, L.; SMERZI, A. Quantum theory of phase estimation. arXiv preprint arXiv:1411.5164, 2014. Citado 3 vezes nas páginas 18, 19, and 20.

12 ARFKEN, G. B.; WEBER, H. J. Mathematical methods for physicists. [S.l.]: AAPT, 1999. Citado na página 19.

13 HELSTROM, C. W. Quantum detection and estimation theory. Journal of Statistical Physics, Springer, v. 1, n. 2, p. 231–252, 1969. Citado na página 20.

14 SCULLY, M. O.; ZUBAIRY, M. S. Quantum optics. [S.l.]: American Association of Physics Teachers, 1999. Citado 2 vezes nas páginas 22 and 43.

15 NIELSEN, M. A.; CHUANG, I. Quantum Computation and Quantum Information. [S.l.]: American Association of Physics Teachers, 2002. Citado 5 vezes nas páginas 25, 28, 31, 32, and 36.

16 GROVER, L. K. Quantum computers can search arbitrarily large databases by a single query. Phys. Rev. Lett., American Physical Society, v. 79, p. 4709–4712, Dec 1997. Citado na página 32.

17 SHOR, P. W. Algorithms for quantum computation: discrete logarithms and factoring. In: IEEE. Proceedings 35th annual symposium on foundations of computer science. [S.l.], 1994. p. 124–134. Citado na página 32.

18 HARROW, A. W.; HASSIDIM, A.; LLOYD, S. Quantum algorithm for linear systems of equations. Phys. Rev. Lett., APS, v. 103, n. 15, p. 150502, 2009. Citado 3 vezes nas páginas 32, 36, and 37.

19 XIN, T. et al. Quantum algorithm for solving linear differential equations: Theory and experiment. Phys. Rev. A, American Physical Society, v. 101, p. 032307, Mar 2020. Citado 2 vezes nas páginas 32 and 36.

20 CAO, Y. et al. Quantum algorithm and circuit design solving the poisson equation. New Journal of Physics, IOP Publishing, v. 15, n. 1, p. 013021, 2013. Citado na página 32.

21 ARRAZOLA, J. M. et al. Quantum algorithm for nonhomogeneous linear partial differential equations. Phys. Rev. A, APS, v. 100, n. 3, p. 032306, 2019. Citado 2 vezes nas páginas 32 and 36.

22 BRAVYI, S.; GOSSET, D.; KÖNIG, R. Quantum advantage with shallow circuits. Science, American Association for the Advancement of Science, v. 362, n. 6412, p. 308–311, 2018. Citado na página 32.

23 DALEY, A. J. et al. Practical quantum advantage in quantum simulation. Nature, Nature Publishing Group UK London, v. 607, n. 7920, p. 667–676, 2022. Citado na página 32.

24 PARIS, M.; REHACEK, J. Quantum state estimation. [S.l.]: Springer Science & Business Media, 2004. v. 649. Citado na página 36.

25 D'ARIANO, G. M.; PARIS, M. G. A.; SACCHI, M. F. Quantum Tomography. 2003. Citado na página 36.

26 GROSS, D. et al. Quantum state tomography via compressed sensing. Phys. Rev. Lett., American Physical Society, v. 105, p. 150401, Oct 2010. Citado na página 36.

27 CRAMER, M. et al. Efficient quantum state tomography. Nature communications, Nature Publishing Group, v. 1, n. 1, p. 1–7, 2010. Citado na página 36.

28 CHRISTANDL, M.; RENNER, R. Reliable quantum state tomography. Phys. Rev. Lett., American Physical Society, v. 109, p. 120403, Sep 2012. Citado na página 36.

29 MAHLER, D. H. et al. Adaptive quantum state tomography improves accuracy quadratically. Phys. Rev. Lett., American Physical Society, v. 111, p. 183601, Oct 2013. Citado na página 36.

30 ZHENG, Y. et al. Solving systems of linear equations with a superconducting quantum processor. Phys. Rev. Lett., APS, v. 118, n. 21, p. 210504, 2017. Citado 2 vezes nas páginas 36 and 37.

31 CLADER, B. D.; JACOBS, B. C.; SPROUSE, C. R. Preconditioned quantum linear system algorithm. Phys. Rev. Lett., APS, v. 110, n. 25, p. 250504, 2013. Citado na página 37.

32 SIMON, C.; POIZAT, J.-P. Creating single time-bin-entangled photon pairs. Phys. Rev. Lett., APS, v. 94, n. 3, p. 030502, 2005. Citado 3 vezes nas páginas 37, 45, and 46.

33 HOHN, M. et al. Energy-time entanglement from a resonantly driven quantum-dot three-level system. Phys. Rev. Res., American Physical Society, v. 5, p. L022060, Jun 2023. Citado na página 37.

34 AKOPIAN, N. et al. Entangled photon pairs from semiconductor quantum dots. Phys. Rev. Lett., American Physical Society, v. 96, p. 130501, Apr 2006. Citado na página 37.

35 JAYAKUMAR, H. et al. Time-bin entangled photons from a quantum dot. Nature communications, Nature Publishing Group UK London, v. 5, n. 1, p. 4251, 2014. Citado na página 37.

36 PRILMÜLLER, M. et al. Hyperentanglement of photons emitted by a quantum dot. Phys. Rev. Lett., American Physical Society, v. 121, p. 110503, Sep 2018. Citado na página 37.

37 HONG, C. K.; OU, Z. Y.; MANDEL, L. Measurement of subpicosecond time intervals between two photons by interference. Phys. Rev. Lett., American Physical Society, v. 59, p. 2044–2046, Nov 1987. Citado na página 37.

38 ŻUKOWSKI, M. et al. "event-ready-detectors" bell experiment via entanglement swapping. Phys. Rev. Lett., American Physical Society, v. 71, p. 4287–4290, Dec 1993. Citado na página 37.

39 BOUWMEESTER, D. et al. Experimental quantum teleportation. Nature, Nature Publishing Group UK London, v. 390, n. 6660, p. 575–579, 1997. Citado na página 37.

40 WANG, J. et al. Integrated photonic quantum technologies. Nature Photonics, Nature Publishing Group UK London, v. 14, n. 5, p. 273–284, 2020. Citado na página 37.

41 JAYAKUMAR, H. et al. Deterministic photon pairs and coherent optical control of a single quantum dot. Phys. Rev. Lett., American Physical Society, v. 110, p. 135505, Mar 2013. Citado 3 vezes nas páginas 37, 38, and 41.

42 DARSHESHDAR, E. et al. Photon-photon correlations from a pair of strongly coupled two-level emitters. Phys. Rev. A, American Physical Society, v. 103, p. 053702, May 2021. Citado na página 38.

43 PEIRIS, M. et al. Two-color photon correlations of the light scattered by a quantum dot. Phys. Rev. B, American Physical Society, v. 91, p. 195125, May 2015. Citado na página 38.

44 BRAŃCZYK, A. M. Hong-ou-mandel interference. arXiv preprint arXiv:1711.00080, 2017. Citado na página 42.

45 WOOLLEY, M. J. et al. Signatures of hong–ou–mandel interference at microwave frequencies. New Journal of Physics, IOP Publishing, v. 15, n. 10, p. 105025, 2013. Citado 2 vezes nas páginas 43 and 44.

46 CARMICHAEL, H. Statistical methods in quantum optics 1: master equations and Fokker-Planck equations. [S.l.]: Springer Science & Business Media, 1999. v. 1. Citado 2 vezes nas páginas 44 and 45.

47 FRANSON, J. D. Bell inequality for position and time. Phys. Rev. Lett., APS, v. 62, n. 19, p. 2205, 1989. Citado na página 46.

48 GINÉS, L. et al. High extraction efficiency source of photon pairs based on a quantum dot embedded in a broadband micropillar cavity. Phys. Rev. Lett., American Physical Society, v. 129, p. 033601, Jul 2022. Citado na página 47.

49 CARDOSO, F. R. et al. Impact of temporal correlations, coherence, and postselection on two-photon interference. arXiv preprint arXiv:2312.01503, 2024. Citado 2 vezes nas páginas 47 and 49.

50 CARDOSO, F. R. et al. Detailed account of complexity for implementation of circuit-based quantum algorithms. Frontiers in Physics, Frontiers, p. 582, 2021. Citado na página 49.

4 Superposition of two-mode squeezed states for quantum information processing and quantum sensing

Superposition of two-mode squeezed states for quantum information processing and quantum sensing

Fernando R. Cardoso [1,*] Daniel Z. Rossatto [2] Gabriel P. L. M. Fernandes [1]
Gerard Higgins [3] and Celso J. Villas-Boas [1]

[1]*Departamento de Física, Universidade Federal de São Carlos, 13565-905 São Carlos, São Paulo, Brazil*
[2]*Universidade Estadual Paulista (Unesp), Campus Experimental de Itapeva, 18409-010 Itapeva, São Paulo, Brazil*
[3]*Department of Physics, Stockholm University, 106 91 Stockholm, Sweden*

(Received 3 February 2021; accepted 17 May 2021; published 2 June 2021)

We investigate superpositions of two-mode squeezed states (TMSSs), which have potential applications in quantum information processing and quantum sensing. We study some properties of these nonclassical states such as the statistics of each mode and the degree of entanglement between the two modes, which can be higher than that of a TMSS with the same degree of squeezing. The states we consider can be prepared by inducing two-mode Jaynes-Cummings and anti-Jaynes-Cummings interactions in a system of two modes and a spin-$\frac{1}{2}$ particle, for instance, in the trapped ion domain, as described here. We show that when two harmonic oscillators are prepared in a superposition of two TMSSs, each reduced single-mode state can be advantageously employed to sense arbitrary displacements of the mode in phase space. The Wigner function of this reduced state exhibits a symmetrical peak centered at the phase-space origin, which has the convenient peculiarity of getting narrower in both quadratures simultaneously as the average photon number increases. This narrow peak can be used as the pointer of our quantum sensor, with its position in phase space indicating the displacement undergone by the oscillator.

DOI: 10.1103/PhysRevA.103.062405

I. INTRODUCTION

In quantum mechanics, the superposition principle is the origin of fascinating nonclassical attributes of quantum states such as quantum coherence [1], squeezing [2], and entanglement [3]. Great efforts, both theoretical and experimental, have been made in order to generate nonclassical states and to investigate their properties, since these states have a wide range of applications in quantum information processing [4–10], quantum-enhanced metrology [11–14], and fundamental tests of quantum mechanics [15,16].

Consider the two-mode squeezed state (TMSS), which is an entangled state of two bosonic modes [2]. This kind of correlation exhibits Bell nonlocality [15], a key ingredient to demonstrate the Einstein-Podolsky-Rosen paradox [17,18] (fundamental test of quantum mechanics), to implement quantum teleportation in continuous variables [19] (manipulation of quantum information), and to detect very weak fields [20] such as the gravitational waves [21] (quantum metrology). Another intriguing nonclassical state is the so-called cat state, a quantum superposition of two diametrically opposed coherent states, which has been employed to demonstrate Schrödinger's famous cat paradox and has been used as a resource for quantum information processing [22–40].

Here we are interested in nonclassical states that connect the concepts of both TMSSs and cat states, namely, a superposition of TMSSs with the same amplitudes but opposite phases. There are already theoretical proposals for their generation in microwave cavities [41] (that could also be adapted for the context of optical cavities or solid-state-based systems), in trapped ions [42], and by using the parity operator [43]. Nevertheless, the literature lacks studies of their properties and applications, which is our goal here.

We first analyze the statistics of each reduced single-mode state (RSMS) of a superposition of TMSSs. For the symmetrical balanced superposition, which we call the even TMSS, we show that there is bosonic superbunching [44,45], an effect with potential applications for advanced imaging techniques (such as ghost interference and imaging) as well as efficient nonlinear light-matter interaction [46–52]. In contrast, for small squeezing parameters, each single mode of the asymmetrical balanced superposition (odd TMSS) presents two-photon anticorrelation [44,45], a desired behavior for single-photon sources [53]. Remarkably, each mode of the even and odd TMSSs behaves as a pseudothermal state, which consists of thermal states with only even and odd Fock excitations, respectively. In addition, we investigate the entanglement degree between the modes of such catlike states, which can be higher than that of the TMSS in certain parameter regimes. Since entanglement is a resource of quantum states, this may be an advantage for quantum information processing.

Afterward, we show that the RSMS of either the even or the odd TMSS can be used to sense the amplitude of arbitrary single-mode displacements acting on a harmonic oscillator. The Wigner functions of these RSMSs each have a symmetrical peak centered at the phase-space origin, which gets

*frc@df.ufscar.br

narrower in both quadratures simultaneously as the squeezing parameter and the average number of excitations in the state increase, but without violating Heisenberg's uncertainty relation. This narrow peak works as the pointer of our quantum sensor, with its position in the phase space indicating the displacement undergone by the oscillator, which could physically describe, for instance, an optical [40] or a microwave resonator mode [35,54,55], vibrational modes of trapped ions [42,56], or a nanomechanical oscillator [57]. In this sense, our sensor is able to probe any time-dependent classical force inducing a displacement on a quantum resonator [58].

Several studies have attempted to figure out the ultimate limits of measuring forces and displacements on an oscillator [59], beating the standard quantum limit and even reaching the Heisenberg one [11,54,60–66]. However, it worth stressing that this is not our goal. Hence, as similarly considered in Ref. [58], which described the determination of both parameters of a displacement acting on an oscillator, the idea we put forward here is the possibility of sensing displacements undergone by a quantum resonator with a single-mode sensor state robust against phase errors when measuring a phase-space quadrature. Furthermore, our results hold regardless of the displacement strength, not being limited to small amplitudes as is the case for grid states [58].

The paper is organized as follows. Section II outlines the procedure for generating superpositions of TMSSs by coupling a two-level quantum system with two bosonic field modes and presents the expressions for the two-mode superposition and the reduced density matrices. In Sec. III we present the relevant statistical properties for those states, such as Wigner functions and populations in the Fock basis, and also the second-order correlation function $g^{(2)}(0)$, discussing the properties of antibunching and superbunching, and show that odd TMSSs can be used as a source of single photons in two modes. Section IV provides the entanglement properties of the superpositions of TMSSs and shows that, for a certain regime of parameters, the superpositions of TMSSs show more entanglement than TMSSs. In Sec. V we present basic concepts of quantum metrology and discuss potential applications of even and odd TMSSs in detecting small coherent forces in any direction (they are sensitive to displacements in all directions in phase space). In Sec VI a simulation of the process for generating even and odd TMSSs in the trapped-ion domain is presented. The process involves coupling the electronic state of the ion with two of its motional degrees of freedom using a two-color laser field. We also discuss the process of probing the Wigner function. Section VII summarizes the results and presents the conclusions.

II. GENERATION OF SUPERPOSITION OF TWO-MODE SQUEEZED STATES

Two-mode squeezed states can be generated by coupling two bosonic modes with a two-level quantum system (a qubit) via the Hamiltonian ($\hbar = 1$)

$$\begin{aligned}\mathcal{H} &= -(\chi^* ab + \chi a^\dagger b^\dagger)\sigma_x \\ &= -(\chi^* ab\sigma^+ + \chi a^\dagger b^\dagger \sigma^-) - (\chi^* ab\sigma^- + \chi a^\dagger b^\dagger \sigma^+),\end{aligned} \tag{1}$$

where χ is the coupling strength; a ($a^\dagger$) and b ($b^\dagger$) are the annihilation (creation) operators for the bosonic modes; $\sigma_x = |+\rangle\langle +| - |-\rangle\langle -|$ is the Pauli-X operator, with $|\pm\rangle = \frac{1}{\sqrt{2}}(|g\rangle \pm |e\rangle)$, where $|e\rangle$ ($|g\rangle$) is the excited (ground) state of the two-level system; and $\sigma^\pm = \frac{1}{2}(\sigma_x \pm i\sigma_y)$ are the fermionic raising and lowering operators. The two terms in the second line of Eq. (1) are a two-mode Jaynes-Cummings interaction and a two-mode anti-Jaynes-Cummings interaction.

The coupling Hamiltonian $\mathcal{H}$ can be realized in various platforms. In Sec. VI we describe how it may be implemented in a trapped-ion setup.

We consider the case where the two-level system is initially in the superposition state $|\phi_0\rangle = \frac{1}{\sqrt{2}}(|-\rangle + e^{i\varphi}|+\rangle) \equiv [\cos(\varphi/2)|g\rangle + i\sin(\varphi/2)|e\rangle]$ while the two bosonic modes are both in the vacuum state $|\psi_0\rangle = |0,0\rangle$. Thus the initial state of the composite system is separable $|\Psi_0\rangle = |\phi_0\rangle|\psi_0\rangle$ (the tensor product symbol is omitted for brevity). After applying the coupling $\mathcal{H}$ for time τ the composite system evolves to

$$|\Psi_\tau\rangle = e^{-i\mathcal{H}\tau}|\Psi_0\rangle = \frac{1}{\sqrt{2}}[|-\rangle|\psi(\xi)\rangle + e^{i\varphi}|+\rangle|\psi(-\xi)\rangle], \tag{2}$$

where

$$\begin{aligned}|\psi(\xi)\rangle &= e^{(\xi^* ab - \xi a^\dagger b^\dagger)}|0,0\rangle \\ &= \frac{1}{\cosh r}\sum_{n=0}^{\infty}(-e^{i\theta}\tanh r)^n |n,n\rangle\end{aligned} \tag{3}$$

is the TMSS which we parametrize by $\xi = -i\chi\tau = re^{i\theta}$, with the squeezing parameter $r = |\chi|\tau$ and squeezing angle $\theta = \arg(\xi)$ [67].

From Eq. (2) the bosonic modes are projected onto a TMSS by measurement of the two-level system in the X basis $\{|+\rangle, |-\rangle\}$. Starting from the TMSS, the reduced density matrix of one mode (found by tracing out the variables of the other mode) is a thermal state

$$\rho_{\rm th} = (1-\lambda_r)\sum_{n=0}^{\infty}\lambda_r^n |n\rangle\langle n| = \sum_{n=0}^{\infty}\frac{\langle n\rangle_{\rm th}^n}{(1+\langle n\rangle_{\rm th})^{n+1}}|n\rangle\langle n|, \tag{4}$$

with the average number of excitations $\langle n\rangle_{\rm th} = {\rm Tr}(a^\dagger a\rho_{\rm th}) = \sinh^2 r = \frac{\lambda_r}{1-\lambda_r}$ and $\lambda_r = \tanh^2 r$ [67].

More interesting results emerge when the two-level system is projected onto the Z basis $\{|e\rangle, |g\rangle\}$. In this basis Eq. (2) becomes

$$|\Psi(\xi,\varphi)\rangle = \frac{1}{2\mathcal{N}_+}|g\rangle|\psi_+(\xi,\varphi)\rangle - \frac{1}{2\mathcal{N}_-}|e\rangle|\psi_-(\xi,\varphi)\rangle, \tag{5}$$

where

$$|\psi_\pm(\xi,\varphi)\rangle = \mathcal{N}_\pm[|\psi(\xi)\rangle \pm e^{i\varphi}|\psi(-\xi)\rangle] \tag{6}$$

are superposition states of two diametrically opposed TMSSs, with $|\mathcal{N}_\pm|^2 = \frac{1}{2}\frac{1+\lambda_r}{(1+\lambda_r)\pm\epsilon_\varphi(1-\lambda_r)}$ and $\epsilon_\varphi = \cos\varphi$. When the two-level system is projected onto $|g\rangle$ ($|e\rangle$) the bosonic modes are projected onto the catlike state $|\psi_+(\xi,\varphi)\rangle$ [$|\psi_-(\xi,\varphi)\rangle$]. Since $\varphi \in [0, 2\pi)$ and $|\psi_+(\xi,\varphi)\rangle = |\psi_-(\xi,\varphi+\pi)\rangle$, it is sufficient to analyze just the properties of one of these states, e.g., $|\psi_+(\xi,\varphi)\rangle$. We refer to the states that emerge

when $\varphi = 0$ and $\varphi = \pi$ as even and odd TMSSs, respectively, $|\psi_E(\xi)\rangle \equiv |\psi_+(\xi, 0)\rangle = |\psi_-(\xi, \pi)\rangle$ and $|\psi_O(\xi)\rangle \equiv |\psi_+(\xi, \pi)\rangle = |\psi_-(\xi, 0)\rangle$, because they comprise only even and odd bosonic excitations

$$|\psi_E(\xi)\rangle = \sqrt{1-\lambda_r^2}\sum_{n=0}^{\infty}\left(-\lambda_r^{1/2}e^{i\theta}\right)^{2n}|2n, 2n\rangle, \tag{7}$$

$$|\psi_O(\xi)\rangle = \sqrt{\frac{1-\lambda_r^2}{\lambda_r}}\sum_{n=0}^{\infty}\left(-\lambda_r^{1/2}e^{i\theta}\right)^{2n+1}|2n+1, 2n+1\rangle. \tag{8}$$

When the two modes are in the state $|\psi_+(\xi, \varphi)\rangle$ the reduced density matrix of each mode is

$$\rho(r, \varphi) = 2(1-\lambda_r)|\mathcal{N}_+|^2\sum_{n=0}^{\infty}\lambda_r^n[1+(-1)^n\cos\varphi]|n\rangle\langle n|, \tag{9}$$

which is independent of the squeezing angle θ. Specifically for the even and odd TMSSs, we have the RSMSs

$$\rho_E = \left(1-\lambda_r^2\right)\sum_{n=0}^{\infty}\lambda_r^{2n}|2n\rangle\langle 2n|, \tag{10}$$

$$\rho_O = \left(1-\lambda_r^2\right)\sum_{n=0}^{\infty}\lambda_r^{2n}|2n+1\rangle\langle 2n+1|. \tag{11}$$

As the even and odd TMSSs [Eqs. (7) and (8)] are built from the superposition of TMSSs, whose reduced single-mode states are described by thermal states [Eq. (4)], it is not surprising that the reduced single modes of the even and odd TMSSs behave as pseudothermal states. We can indeed identify that by rewriting Eqs. (10) and (11) in terms of $\langle n\rangle_{\rm th}$ and comparing them with $\rho_{\rm th}$, namely,

$$\rho_E = \frac{1+2\langle n\rangle_{\rm th}}{1+\langle n\rangle_{\rm th}}\sum_{n=0}^{\infty}\frac{\langle n\rangle_{\rm th}^{2n}}{(1+\langle n\rangle_{\rm th})^{2n+1}}|2n\rangle\langle 2n|, \tag{12}$$

$$\rho_O = \frac{1+2\langle n\rangle_{\rm th}}{\langle n\rangle_{\rm th}}\sum_{n=0}^{\infty}\frac{\langle n\rangle_{\rm th}^{2n+1}}{(1+\langle n\rangle_{\rm th})^{(2n+1)+1}}|2n+1\rangle\langle 2n+1|. \tag{13}$$

From these expressions one can recognize ρ_E and ρ_O as even and odd thermal states (pseudothermal states), respectively [68], which are particular cases of binomial negative states [69]. Even thermal states (even RSMSs) can also be generated through a parametric pumping field with fluctuations [70].

III. STATISTICAL PROPERTIES

Let us discuss the properties of each single mode of the catlike state. Since $\rho(r, \varphi)$ is diagonal in the Fock basis, with populations $P_n(\varphi) = 2(1-\lambda_r)|\mathcal{N}_+|^2\lambda_r^n[1+(-1)^n\cos\varphi]$, the Wigner function of this state can be written as $W(q, p) = \sum_{n=0}^{\infty}P_nW_n(q, p)$, in which $W_n(q, p) = (2/\pi)(-1)^nL_n(4s^2)e^{-2s^2}$ is the Wigner function of the Fock state $|n\rangle$, with the Laguerre polynomial $L_n(x)$ and $s^2 = q^2 + p^2$. Here q and p are the eigenvalues of the position and momentum quadrature operators of the mode $\hat{q} = a + a^\dagger$ and $\hat{p} = i(a^\dagger - a)$, respectively, representing the dimensionless amplitudes of the mode quadratures in phase space [71].

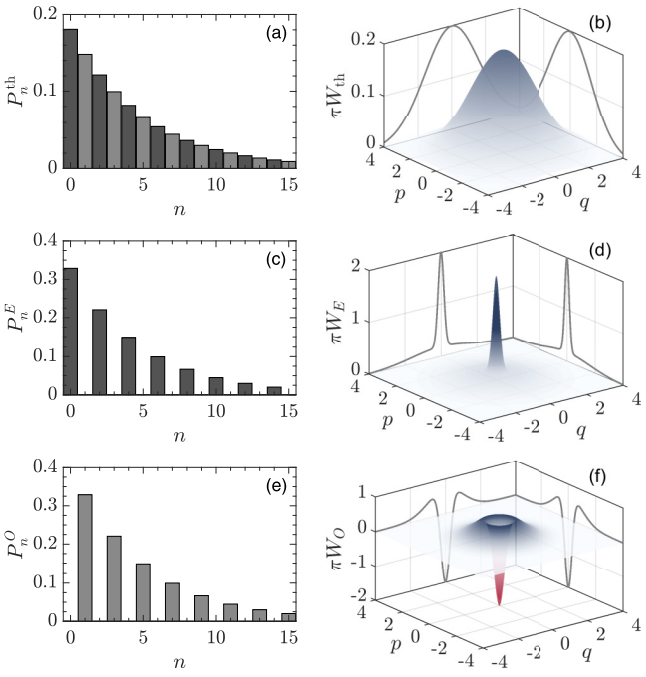

FIG. 1. Statistical properties of the reduced single-mode states: populations in the Fock basis of the (a) thermal state ($P_n^{\rm th}$) and for each mode of the (c) even (P_n^E) and (e) odd (P_n^O) TMSSs for the squeezing parameter $r = 1.5$ (light gray for odd occupation) and (b), (d), and (f) Wigner functions for the same reduced single-mode states, respectively.

First we observe that $\rho(r, \varphi)$ reduces to the thermal state $\rho_{\rm th}$ when $\varphi = \{\frac{\pi}{2}, \frac{3\pi}{2}\}$ because $|\psi_+(\xi, \varphi = \frac{\pi}{2}, \frac{3\pi}{2})\rangle$ reduces to $|\psi(\xi)\rangle$ except for a global phase factor. The Wigner function of the thermal state $\rho_{\rm th}$ is given by the two-dimensional Gaussian function

$$W_{\rm th}(q, p) = \frac{2}{\pi}\frac{\exp\left(-2\frac{(q^2+p^2)}{2\langle n\rangle_{\rm th}+1}\right)}{2\langle n\rangle_{\rm th}+1} = \frac{2}{\pi}\frac{1-\lambda_r}{1+\lambda_r}\exp\left(-2\frac{1-\lambda_r}{1+\lambda_r}(q^2+p^2)\right), \tag{14}$$

while for each single mode of the even (ρ_E) and odd (ρ_O) TMSSs the Wigner functions are each described by sums of two two-dimensional Gaussian functions

$$W_{E_O}(q, p) = \varpi_{E_O}\left((1-\lambda_r)\exp\left[-2\left(\frac{1-\lambda_r}{1+\lambda_r}\right)(q^2+p^2)\right] \pm (1+\lambda_r)\exp\left[-2\left(\frac{1+\lambda_r}{1-\lambda_r}\right)(q^2+p^2)\right]\right), \tag{15}$$

with $\varpi_E = \pi^{-1}$ and $\varpi_O = (\pi\lambda_r)^{-1}$.

Figure 1 shows the populations and the Wigner function for $\rho_{\rm th}$ ($P_n^{\rm th}$ and $W_{\rm th}$), ρ_E (P_n^E and W_E), and ρ_O (P_n^O and W_O) for the squeezing parameter $r = 1.5$. We observe that the profile of the populations for ρ_E and ρ_O are very similar, namely, $P_{2n+1}^O = P_{2n}^E = (1-\lambda_r^2)\lambda_r^{2n}$, that is, the probability distribu-

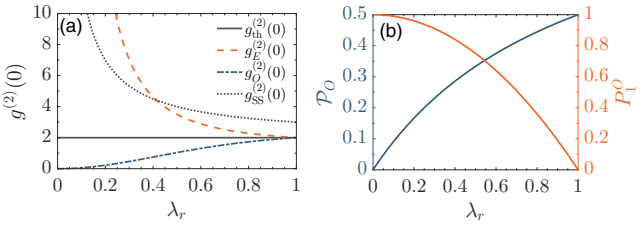

FIG. 2. (a) Second-order correlation function at zero-time delay $g^{(2)}(0)$ as a function of the squeezing parameter r, via $\lambda_r = \tanh^2(r)$, for the thermal state ($\rho_{\rm th}$) (black solid line), the RSMSs of the even (ρ_E) (orange dashed line) and odd (ρ_O) (blue dot-dashed line) TMSSs, and the single-mode squeezed state ($|{\rm SS}\rangle$) (black dotted line). (b) Probability of projecting onto the odd TMSS ($\mathcal{P}_O$) (ascending blue line) and probability of it having a single-photon in each mode (P_1^O) (descending orange line) as a function of λ_r.

tion of ρ_O is shifted by one unit compared with the distribution of ρ_E.

Accordingly, the average number of excitations is related by $\langle n\rangle_O = \langle n\rangle_E + 1$, where $\langle n\rangle_E = {\rm Tr}(a^\dagger a \rho_E) = 2\lambda_r^2/(1-\lambda_r^2)$. Moreover, we notice that P_n^E and P_n^O are very similar to $P_n^{\rm th}$, except for a normalization factor and for being nonzero only for even and odd Fock numbers, respectively, which illustrates the pseudothermal behavior of each mode of the even and odd TMSSs. It is also important to notice in Fig. 1 a concentrated profile of Wigner functions around the phase-space origin for both ρ_E and ρ_O, which can be useful for metrological purposes, as we discuss in Sec. V.

We can also investigate the statistics of ρ_E and ρ_O using the second-order correlation function at zero-time delay $g^{(2)}(0) = \langle a^\dagger a^\dagger a a\rangle/\langle a^\dagger a\rangle^2$,

$$g_E^{(2)}(0) = 2 + \frac{1-\lambda_r^2}{2\lambda_r^2} \geqslant 2 \quad \text{for } \rho_E, \tag{16}$$

$$g_O^{(2)}(0) = 2 - \frac{2\left(1-\lambda_r^2\right)}{\left(1+\lambda_r^2\right)^2} \leqslant 2 \quad \text{for } \rho_O. \tag{17}$$

For large values of the squeezing parameter ($\lambda_r \to 1$ or, equivalently, for $r \gg 1$) we observe that the correlation functions $g^{(2)}(0)$ of ρ_E and ρ_O become indistinguishable and tend to the thermal one, i.e., $g_{\rm th}^{(2)}(0) = 2$. In contrast, when the squeezing parameter is small, the RSMSs of the even and odd TMSSs present completely opposite statistics: While ρ_O exhibits antibunching [$g_O^{(2)}(0) < 1$], ρ_E displays superbunching [$g_E^{(2)}(0) > 2$]. To be more specific, $g_E^{(2)}(0) > 2\,\forall\, r \geqslant 0$ ($\lambda_r \geqslant 0$) and $g_O^{(2)}(0) < 1$ for $0 \leqslant \lambda_r < \sqrt{\sqrt{5}-2} \approx 0.49 \leftrightarrow 0 \leqslant r < \tanh^{-1}\sqrt[4]{\sqrt{5}-2} \approx 0.86$. Figure 2(a) displays the change of $g^{(2)}(0)$ with λ_r for $\rho_{\rm th}$, ρ_E, ρ_O and the single-mode squeezed state $|{\rm SS}\rangle = e^{(re^{-i\theta}a^2 - re^{i\theta}a^{\dagger 2})/2}|0\rangle$, with $g_{\rm SS}^{(2)}(0) = 2 + 1/\lambda_r$. We have included the latter for the sake of comparison, since it has the same average number of excitations of each single mode of the TMSS ($\langle n\rangle_{\rm SS} = \langle n\rangle_{\rm th}$) and presents superbunching. Remarkably, each mode of the even TMSS exhibits more superbunching than if it were in a single-mode squeezed state [$g_E^{(2)}(0) > g_{\rm SS}^{(2)}(0) > 2$] within the parameter range $0 \leqslant \lambda_r < \sqrt{2}-1 \approx 0.41 \leftrightarrow 0 \leqslant r < \tanh^{-1}\sqrt{\sqrt{2}-1} \approx 0.76$.

Due to the aforementioned attributes, each mode of the even and odd TMSSs is quite suitable for quantum devices related to advanced imaging techniques and single-photon generation, respectively. A single photon may be produced in each of the two modes when the odd TMSS is produced. The probability of projecting onto the odd TMSS is $\mathcal{P}_O = \lambda_r/(1+\lambda_r)$. The proportion of the odd TMSS described by two single photons is $P_1^O = 1-\lambda_r^2$. Production of high-purity states of two single photons requires $\lambda_r \to 0$, which comes at the expense of a low production probability $\mathcal{P}_O$, as shown in Fig. 2(b). It is worth noting that the qubit may be used to herald projection onto the odd TMSS.

IV. ENTANGLEMENT

Considering a bipartite system in a pure state, the degree of entanglement between the subsystems can be quantified through the linear entropy $E = \frac{d}{d-1}(1-\gamma)$, where $\gamma = {\rm Tr}(\rho_1^2)$ is the purity of one of the subsystems described by the reduced density matrix ρ_1 and $d = \dim \rho_1$. Since our subsystems are bosonic modes, with infinite-dimensional Hilbert spaces, $0 \leqslant E \leqslant 1$ such that $E = 0$ for separable states while $E = 1$ for maximally entangled continuous-variable states.

For the TMSS $|\psi(\xi)\rangle$, the degree of entanglement is

$$E_{\rm TMSS}(r) = 1 - \frac{1-\lambda_r}{1+\lambda_r}, \tag{18}$$

while for the general superposition $|\psi_+(\xi,\varphi)\rangle$,

$$E_\varphi(r) = 1 - \left(\frac{1-\lambda_r^2}{1+\lambda_r^2}\right)\frac{(1+\epsilon_\varphi)^2 + \lambda_r^2(1-\epsilon_\varphi)^2}{[(1+\epsilon_\varphi) + \lambda_r(1-\epsilon_\varphi)]^2}. \tag{19}$$

Here $E_\varphi(r) = E_{\rm TMSS}(r)$ for any r when $\varphi = \{\frac{\pi}{2}, \frac{3\pi}{2}\} \to \epsilon_\varphi = 0$, which is not a surprise, since we have seen in Sec. III that $\rho(r,\varphi)$ reduces to $\rho_{\rm th}$ for these values of φ. The same degree of entanglement also occurs when $\lambda_r = \sqrt{(1+\epsilon_\varphi)/(1-\epsilon_\varphi)}$ or $r \to \infty$. Notably, $E_\varphi(r) > E_{\rm TMSS}(r)$ for $\varphi \in (\frac{\pi}{2}, \pi) \cup (\pi, \frac{3\pi}{2})$ provided $0 < \lambda_r < \sqrt{(1+\epsilon_\varphi)/(1-\epsilon_\varphi)}$. In this range, for the same value of the squeezing parameter r, the entanglement degree in the catlike TMSSs becomes higher than that in the TMSS. Curiously, it can reach high values even for $r \ll 1$, namely, $E_\varphi(r) \approx 0.5$ for $\varphi = \pi + \beta$ and $r \approx |\beta|/2$ considering $|\beta| \ll 1$, for which we have $|\psi_+(\xi,\varphi)\rangle \approx (|0,0\rangle - {\rm sgn}(\beta)e^{i(\theta+\pi/2)}|1,1\rangle)/\sqrt{2}$, i.e., a maximally entangled qubit state. By contrast, $E_{\rm TMSS}(r) \approx \beta^2/2 \ll 1$ under the same conditions, for which we have $|\psi(\xi)\rangle \approx (|0,0\rangle - (|\beta|/2)e^{i\theta}|1,1\rangle)/\sqrt{1+|\beta|^2/4} \approx |0,0\rangle$, i.e., a separable state. This means that it is possible to generate much more entanglement between the modes with a lower squeezing parameter by exploiting the catlike states instead of the TMSS, indicating an advantage from the point of view of quantum information science. Figure 3 illustrates the above results. It is worth noting that the even ($\varphi = 0$) and odd ($\varphi = \pi$) TMSSs have the same entanglement degree $E_E(r) = E_O(r) = 1 - (1-\lambda_r^2)/(1+\lambda_r^2)$, which is always smaller than or equal to that for the TMSS. Despite that, we show in the next section that their RSMSs can be employed for quantum metrological purposes.

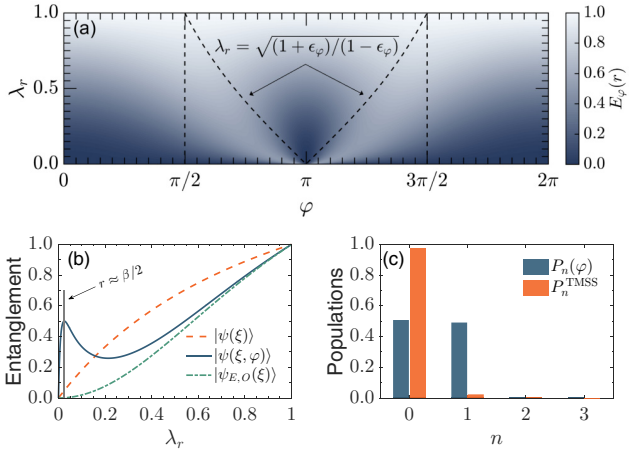

FIG. 3. (a) Density plot showing the entanglement between the two modes $[E_\varphi(r)]$, when they are in the catlike state $|\psi_+(r,\varphi)\rangle$, as a function of the initial-state relative phase φ and the two-mode squeezing parameter r via $\lambda_r = \tanh^2(r)$. The dashed lines delimit the region for which $E_\varphi(r)$ surpasses the entanglement of the TMSS $[E_{\mathrm{TMSS}}(r)]$. (b) Entanglement degree as a function of λ_r corresponding to the states $|\psi(\xi)\rangle$ (orange dashed line), $|\psi(\xi,\varphi)\rangle$ (blue solid line), and $|\psi_{E,O}(\xi)\rangle$ (green dot-dashed line), considering $\varphi = \pi + \beta$, with $\beta = \pi/10$. One can notice here that the entanglement outperforming occurs even for small values of r, reaching its maximum for $r \approx |\beta|/2$ $(\lambda_r \approx r^2)$ when $|\beta| \ll 1$. Surprisingly, under this condition an extreme contrast between the entanglement in the catlike state and in the TMSS takes place; while the latter is essentially a separable state given by the two-mode ground state $[|\psi(\xi)\rangle \approx (|0,0\rangle - (|\beta|/2)e^{i\theta}|1,1\rangle)/\sqrt{1+|\beta|^2/4} \to E_{\mathrm{TMSS}}(r) \approx 0.05$ for the considered parameters], the former is approximately a maximally entangled qubit state $[|\psi_+(\xi,\varphi)\rangle \approx (|0,0\rangle - ie^{i\theta}|1,1\rangle)/\sqrt{2} \to E_\varphi(r) \approx 0.5]$. The even and odd TMSSs have the same entanglement degree, which is always smaller than or equal to that for the TMSS. (c) Populations of the catlike state $[P_n(\varphi)]$ [blue (dark gray) bars] and the TMSS (P_n^{TMSS}) [orange (light gray) bars] for $r = \beta/2$ and $\varphi = \pi + \beta$, with $\beta = \pi/10$.

V. QUANTUM METROLOGY

Quantum metrology takes advantage of the properties of quantum mechanics to better estimate parameters involved in dynamical processes, using quantum states as probes [72]. The process of estimating a parameter y follows a specific sequence of steps, known as the protocol of estimation [73]: (i) The probe state is prepared in an initial and determined configuration, represented by the density matrix ρ; (ii) the initial state evolves through a dynamical process, which is represented by a unitary evolution operator $U(y)$ such that the final configuration of the system is dependent on the parameter y; (iii) the final state $\rho(y)$ is measured, giving results $y_{\mathrm{est}}(\kappa)$, with associated probabilities $P_\kappa(y)$; (iv) these results are used to estimate the parameter y. It is important to note that different results κ come from separate processes of measurement. The average value of the parameter can then be calculated with the individual estimation $y_{\mathrm{est}}(\kappa)$ as $\langle y_{\mathrm{est}}\rangle = \sum_\kappa y_{\mathrm{est}}(\kappa)P_\kappa(y)$, with $\sum_\kappa P_\kappa(y) = 1$. The deviation of the parameter can be defined as $(\Delta y)^2 \equiv \langle (y_{\mathrm{est}} - \langle y_{\mathrm{est}}\rangle)^2\rangle$ and its lower bound is proportional to the inverse of the Fisher information $\langle (\frac{d\ln[P_\kappa(y)]}{dy})^2\rangle$ [74,75] with respect to the parameter y and represents the maximum quantity of information that can be obtained with respect to y through the probability set $\{P_\kappa(y)\}$, as derived from the Cramér-Rao inequality [76,77]. Although this is the main method of estimation of the parameter we discuss, nonlinear methods of estimation for quantum metrological purposes are also available [78–80].

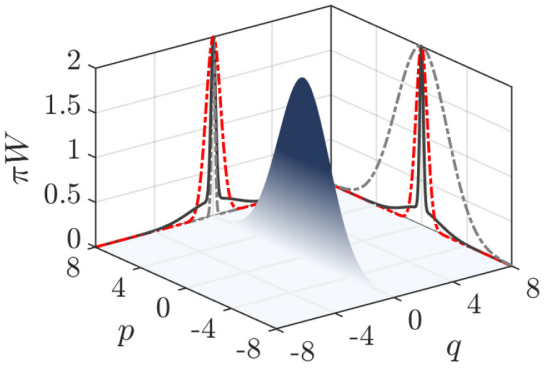

FIG. 4. Comparison of the Wigner function and its projections of the single-mode squeezed state (projections in light gray dot-dashed curves) with the projections of the RSMS of the even TMSS (black solid lines), with $r = 1.5$ and the vacuum state $|0\rangle$ (red dashed lines). The projections of the RSMS of the even TMSS display tails because they are described by the summation of two two-dimensional Gaussian functions [see Eq. (15)].

Given a generator $U(y)$ for the transformation on the density matrix which leads to the final state $\rho(y)$, the quantum Fisher information for y with probe state ρ can be written as $F(y) = 4[\Delta U(y)]^2$ if ρ is a pure state, with $[\Delta U(y)]^2 = \langle U^2(y)\rangle - \langle U(y)\rangle^2$, and $F(y) = 2\sum_{i,j}\frac{(\delta_i-\delta_j)^2}{\delta_i+\delta_j}|\langle i|U(y)|j\rangle|^2$ if ρ is mixed, where δ_j and $|j\rangle$ stand for the eigenvalues and eigenvectors of ρ, respectively.

Single-mode squeezed states are widely used in quantum metrology due to the reduction of fluctuations in one of the quadratures of the bosonic mode [81–83]. The fact that the Wigner functions of each mode of the even and odd TMSSs are invariant under rotations and sharply concentrated around the origin of the phase space (Fig. 1) motivates the study of applications of those states in quantum metrology.

Figure 4 shows a comparison between the Wigner functions of a single-mode squeezed state, with reduced noise in one of the quadratures, the RSMS of the even TMSS, for the same value of the squeezing parameter r, and a vacuum coherent state. The single-mode squeezed state has a more concentrated probability distribution profile than the RSMS. However, we would like to point out that the symmetry of the Wigner function (around the origin of the phase space) of the even and odd RSMSs implies a robust and sensitive scheme for applications in quantum metrology, since that peak, whose width can be controlled by the squeezing parameter r, allows for probing small displacements in any direction, as described in detail in the next section. Furthermore, the Wigner function still presents thermal contributions along broad regions of the phase space, so, despite the concentrated peak around the origin, the Heisenberg uncertainty principle

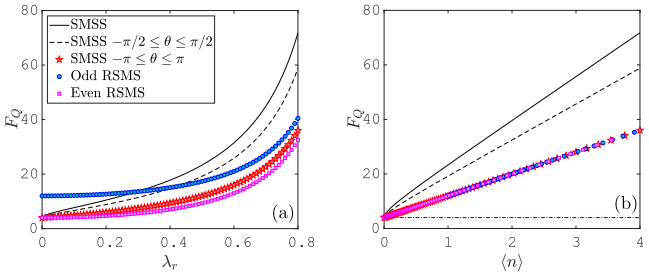

FIG. 5. (a) Quantum Fisher information F_Q as a function of λ_r and (b) average number of excitations in the bosonic field $\langle n \rangle$ for each state. If the direction of squeezing in phase space matches the displacement direction, single-mode squeezed states are well suited for measuring the displacement. This is shown by the quantum Fisher information F_Q of the solid black curve. If the angle θ between the squeezing direction and the displacement direction is large, it can be more efficient to measure the displacement using the RSMS of the even or odd TMSS. This is seen by comparing the red star curve (the black dashed and red star curves show the average F_Q values obtained with SMSSs when θ is spread over a range) with the blue circle and pink square curves. Here $\lambda_r = \tanh^2 r$ describes the amount of squeezing. Note also that for small values ($\lambda_r < 0.3$) the odd RSMS presents a larger F_Q than the SMSS. In particular, for $\lambda \to 0$, the odd RSMS (blue circles) approximates to the single-photon state $|1\rangle$ and the SMSS to the vacuum $|0\rangle$. From (b) it can be seen that F_Q behaves linearly for all states and, in particular, for small values of λ, $F_Q(\langle n \rangle) \approx 4(2\langle n \rangle + 1)$, with $\langle n \rangle$ the average number of excitations for each corresponding state. Note also that the red star, blue circle, and pink square curves overlap in (b), corresponding to the SMSS ($-\pi \leqslant \theta \leqslant \pi$) and odd and even RSMSs, respectively. We also included in (b) the quantum Fisher information for a coherent state $|\alpha\rangle$ represented by the blue dot-dashed line, which presents a constant value of $F_Q = 4.0$.

is not violated. For estimation of displacement, we employ the general quadrature operator $X(\phi) = ae^{-i\phi} + a^\dagger e^{i\phi}$, which corresponds to position and momentum operators for $\phi = 0, \pi/2$, respectively. Figure 5 shows the quantum Fisher information for the RSMSs of the even and odd TMSSs and for the single-mode squeezed state, for estimation of position amplitudes of the mode. Although the single-mode squeezed state shows better results for the quantum Fisher information (for a specific quadrature), by employing a measurement scheme of the Wigner function [84], the even and odd RSMSs could be employed to detect small coherent forces.

For our state, differently from the single-mode squeezed state, one does not need to worry about the phase of the displacement due to the symmetry of its Wigner function around the origin, as we see in Fig. 4. Thus, although both variances of the quadratures X and P increase with the amount of squeezing λ as $(3\lambda^2 + 1)/(1 - \lambda^2)$ and $(\lambda^2 + 3)/(1 - \lambda^2)$ for the even and odd RSMSs, respectively, the RSMSs still can be very useful to detect small displacements and, consequently, small forces, by monitoring the Wigner function of the reduced mode state. This is described in detail in the next section, showing in particular how these ideas can be implemented in trapped-ion systems.

VI. ION IMPLEMENTATION

Two-mode squeezed states can be generated by a combination of Jaynes-Cummings and anti-Jaynes-Cummings interactions, as we see in Eq. (1). In this section we describe how these interactions can be realized to produce an entangled state of two motional modes of a single trapped ion, which could be used for enhanced force sensing. In Ref. [42] similar effective Hamiltonians are proposed, but the proposal involves two trapped ions and other types of two-mode squeezed states are considered.

Electronic states of a single trapped ion can be coupled to the ion's motion using a laser field. When the laser field's wave vector projects onto two motional modes (x and y), the Hamiltonian describing the coupling (within the interaction picture and after taking the rotating-wave approximation) is

$$H_F = \frac{\Omega}{2} e^{-i\Delta t} e^{i\eta_x (a e^{-i\omega_x t} + a^\dagger e^{i\omega_x t})} e^{i\eta_y (b e^{-i\omega_y t} + b^\dagger e^{i\omega_y t})} \sigma^+ + \text{H.c.}, \tag{20}$$

where Ω is the coupling strength, Δ is the detuning of the laser field from the atomic resonance, $a^\dagger$, $b^\dagger$ and a, b raise and lower the states of the x and y modes, and ω_i are the motion mode frequencies. In addition, σ^+ and σ^- act on the ion's internal state and the Lamb-Dicke parameters are defined by

$$\eta_i = k_i \sqrt{\frac{\hbar}{2m\omega_i}}, \tag{21}$$

where k_i is the projection of the laser field's wave vector in the i direction and m is the ion mass.

When a two-color coupling field satisfying $\Delta = \pm(\omega_x + \omega_y)$ is used, provided the system is within the Lamb-Dicke regime $\eta_x^2(2n_x + 1)$ and $\eta_y^2(2n_y + 1) \ll 1$ (n_i is the number of phonons in the i mode), the coupling Hamiltonian becomes

$$\begin{aligned} H_{\text{eff}} &= -\tfrac{1}{2}\eta_x \eta_y \Omega \sigma^+ (ab + a^\dagger b^\dagger) + \text{H.c.} \\ &= -\tfrac{1}{2}\eta_x \eta_y \Omega \sigma_x (ab + a^\dagger b^\dagger) \end{aligned} \tag{22}$$

after another application of the rotating-wave approximation. Identifying $\chi = \frac{1}{2}\eta_x \eta_y \Omega$, this Hamiltonian is equivalent to Eq. (1) for real-valued χ.

The coupling laser field drives second-order sideband transitions which are relatively weak. This implementation requires the coupling dynamics to be faster than the decoherence time $\eta_x \eta_y \Omega \gg \gamma$, also off-resonant excitation of stronger transitions must be avoided $\Omega \ll \omega_x + \omega_y$.

If the system is initialized in $|\Psi(t = 0)\rangle = |g\rangle|0, 0\rangle$, then after evolution under H_F given by Eq. (22), followed by projection of the electronic state onto $|g\rangle$ ($|e\rangle$), the motional modes of the trapped ion can be prepared in the even (odd) TMSS in principle. Projective measurement of a trapped ion's electronic state is commonly accomplished with near-unity fidelity by detecting laser-induced fluorescence detection [56]. We note that if the ion is in state $|g\rangle$, the scattering of fluorescence photons destroys the ion's motional state. If the ion is in projected onto the nonfluorescing state ($|e\rangle$), the motional state (the odd TMSS) will be unperturbed.

In Fig. 6 we plot the fidelity of the states which evolve under the effective Hamiltonian H_{eff} [Eq. (22)] as compared with the states evolved under the full Hamiltonian H_F [Eq. (20)]. The effective Hamiltonian describes the squeezing dynam-

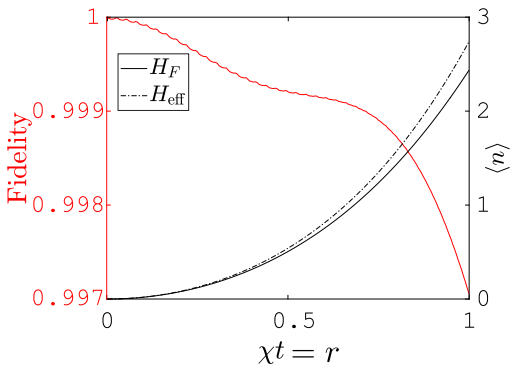

FIG. 6. The squeezing dynamics in a trapped ion system is captured well by $H_{\rm eff}$: The fidelity (represented by the red solid decreasing curve) shows the overlap of the state evolved according to the effective Hamiltonian $H_{\rm eff}$ (black dot-dashed curve) with the state evolved according to the full Hamiltonian H_F (black solid line). The evolution of the average number of excitations in the bosonic fields is also shown.

ics well up to $\chi t = r = 1$. The parameters considered are $\omega_x = 1.0$, $\omega_y = 1.2$, $\Omega = \omega_x/20$, and $\eta_x = \eta_y = 0.1$. We also show the evolution of the average number of phonons $\langle n \rangle = a^\dagger a + b^\dagger b$.

Now we describe how these states can be employed to detect small forces by measuring the Wigner function of one of the modes based on the protocol given in Ref. [84]. By tracing out one of the modes, one can see that the Wigner function of the reduced state is completely symmetric around the origin (see Fig. 4). Thus, one does not need to worry about the phase of the coherent displacement applied to the ion trap.

A weak coherent force applied on either the ion or the ion trap causes a displacement $D(\alpha) = e^{\alpha a^\dagger - \alpha^* a}$ of the mode state, resulting in a state $\rho(\alpha) = D(\alpha)\rho_v D^{-1}(\alpha)$, where ρ_v is the reduced density operator of the motional state. The phase and amplitude of the complex parameter α indicate the direction and intensity of the displacement operation in the phase space. At this point a laser pulse resonant to the $|g\rangle \leftrightarrow |e\rangle$ transition (the carrier transition) is applied, whose Hamiltonian is given by (keeping terms up to η_x^2) $H_c = \Omega/2[1 - \eta_x^2(a^\dagger a + \frac{1}{2})]\sigma_x$. Adjusting the interaction time τ such that $\Omega\eta_x^2\tau/2 = \pi/2$, the evolution operator will be given by $U = e^{-iH_c\tau} = e^{-i(\Phi - \pi a^\dagger a/2)}$, with $\Phi = \Omega\tau/2 - \pi/4$. As shown in [84], the evolved state of the system, $U\rho(\alpha)|e\rangle\langle e|U^{-1}$, will be

$$[|e\rangle \cos(\Phi - \pi a^\dagger a/2) - i|g\rangle \sin(\Phi - \pi a^\dagger a/2)]\rho(\alpha) \times [\langle e| \cos(\Phi - \pi a^\dagger a/2) + i\langle g| \sin(\Phi - \pi a^\dagger a/2)] \quad (23)$$

and then the population inversion $P_{eg} = \langle \sigma_z \rangle$ of the ion will give, apart from a constant factor, the value of the Wigner function at the position $\alpha = (q - ip)/2$ in phase space, i.e., $P_{eg} \propto W(\alpha)$ [84]. For the even (odd) TMSS, when there is no force acting on the ion, this results in $\alpha = 0$ and consequently the maximal (minimal) value of the atomic population inversion. However, for small values of $|\alpha|$, which are larger than the width of the central peak of the Wigner function, the population inversion would result in nearly zero, thus allowing us to detect the action of small coherent forces applied in any direction.

VII. CONCLUSION

In this work we have presented the statistical properties of superpositions of two-mode squeezed states with relative phase factors, giving special attention to two cases of relative phase, corresponding to the even and odd TMSSs. The reduced single-mode states of the even (ρ_E) and odd (ρ_O) TMSSs, obtained by tracing out one of the bosonic modes, present populations in the Fock basis which resemble thermal distribution, thus illustrating the pseudothermal behavior of those states. Furthermore, we investigated the second-order correlation function of ρ_E and ρ_O and showed that, for small squeezing parameters, ρ_E presents superbunching behavior, while ρ_O presents antibunching, thus making it a potential source of single photons. We studied entanglement between the two bosonic modes corresponding to the superposition of TMSSs; for small values of the squeezing parameter r and specific relative phase angle φ, the superpositions show a larger degree of entanglement than TMSSs, generating a maximally mixed state in each of the RSMSs when tracing out one of the mode variables. We also studied the pseudoprobability distributions related to ρ_E and ρ_O in phase space, given by the Wigner function $W(q, p)$. We pointed out that the profiles of both RSMSs narrow around the phase-space origin as the squeezing parameter is increased. For ρ_E and ρ_O, the symmetry of $W(q, p)$ makes the states sensible to weak forces in any direction of the phase space, in contrast with the single-mode squeezed state. Finally, we described how the states discussed above can be generated and how they can be employed to measure weak forces in the trapped-ion domain, by deriving effective two-mode Jaynes-Cummings-like interactions, thus motivating applications in quantum information processing, quantum metrology, and quantum sensing of small coherent displacements.

ACKNOWLEDGMENTS

This work was supported by the Coordenação de Aperfeiçoamento de Pessoal de Nível Superior (CAPES), Finance Code 001, and through the CAPES/STINT project, Grant No. 88881.304807/2018-01. C.J.V.-B. is grateful for support from São Paulo Research Foundation Grant No. 2019/11999-5 and the National Council for Scientific and Technological Development Grant No. 307077/2018-7. This work is also part of the Brazilian National Institute of Science and Technology for Quantum Information Grant No. 465469/2014-0. G.H. gratefully acknowledges the hospitality of Universidade Federal de São Carlos and Universidade de São Paulo.

[1] A. Streltsov, G. Adesso, and M. B. Plenio, Quantum coherence as a resource, Rev. Mod. Phys. **89**, 041003 (2017).

[2] A. I. Lvovsky, in *Fundamentals of Photonics and Physics*, edited by D. L. Andrew (Wiley, Hoboken, 2015), Vol. 1, Chap. 5, pp. 121–164.

[3] R. Horodecki, P. Horodecki, M. Horodecki, and K. Horodecki, Quantum entanglement, Rev. Mod. Phys. **81**, 865 (2009).
[4] M. A. Nielsen and I. L. Chuang, *Quantum Computation and Quantum Information* (Cambridge University, Cambridge, 2000).
[5] T. D. Ladd, F. Jelezko, R. Laflamme, Y. Nakamura, C. Monroe, and J. L. O'Brien, Quantum computers, Nature (London) **464**, 45 (2010).
[6] B. M. Terhal, Quantum error correction for quantum memories, Rev. Mod. Phys. **87**, 307 (2015).
[7] N. Gisin and R. Thew, Quantum communication, Nat. Photon. **1**, 165 (2007).
[8] V. Scarani, H. Bechmann-Pasquinucci, N. J. Cerf, M. Dušek, N. Lütkenhaus, and M. Peev, The security of practical quantum key distribution, Rev. Mod. Phys. **81**, 1301 (2009).
[9] H. J. Kimble, The quantum internet, Nature (London) **453**, 1023 (2008).
[10] R. Van Meter, *Quantum Networking (Networks and Telecommunications)* (Wiley, Hoboken, 2014).
[11] V. Giovannetti, S. Lloyd, and L. Maccone, Quantum-enhanced measurements: Beating the standard quantum limit, Science **306**, 1330 (2004).
[12] V. Giovannetti, S. Lloyd, and L. Maccone, Advances in quantum metrology, Nat. Photon. **5**, 222 (2011).
[13] G. Tóth and I. Apellaniz, Quantum metrology from a quantum information science perspective, J. Phys. A: Math. Theor. **47**, 424006 (2014).
[14] L. Pezzè, A. Smerzi, M. K. Oberthaler, R. Schmied, and P. Treutlein, Quantum metrology with nonclassical states of atomic ensembles, Rev. Mod. Phys. **90**, 035005 (2018).
[15] N. Brunner, D. Cavalcanti, S. Pironio, V. Scarani, and S. Wehner, Bell nonlocality, Rev. Mod. Phys. **86**, 419 (2014).
[16] D. Z. Rossatto, T. Werlang, E. I. Duzzioni, and C. J. Villas-Boas, Nonclassical Behavior of an Intense Cavity Field Revealed by Quantum Discord, Phys. Rev. Lett. **107**, 153601 (2011).
[17] A. Einstein, B. Podolsky, and N. Rosen, Can Quantum-Mechanical Description of Physical Reality Be Considered Complete? Phys. Rev. **47**, 777 (1935).
[18] M. D. Reid, P. D. Drummond, W. P. Bowen, E. G. Cavalcanti, P. K. Lam, H. A. Bachor, U. L. Andersen, and G. Leuchs, Colloquium: The Einstein-Podolsky-Rosen paradox: From concepts to applications, Rev. Mod. Phys. **81**, 1727 (2009).
[19] S. Pirandola, J. Eisert, C. Weedbrook, A. Furusawa, and S. L. Braunstein, Advances in quantum teleportation, Nat. Photon. **9**, 641 (2015).
[20] P. M. Anisimov, G. M. Raterman, A. Chiruvelli, W. N. Plick, S. D. Huver, H. Lee, and J. P. Dowling, Quantum Metrology with Two-Mode Squeezed Vacuum: Parity Detection Beats the Heisenberg Limit, Phys. Rev. Lett. **104**, 103602 (2010).
[21] R. Schnabel, Squeezed states of light and their applications in laser interferometers, Phys. Rep. **684**, 1 (2017).
[22] W. Schleich, M. Pernigo, and F. L. Kien, Nonclassical state from two pseudoclassical states, Phys. Rev. A **44**, 2172 (1991).
[23] B. C. Sanders, Entangled coherent states, Phys. Rev. A **45**, 6811 (1992).
[24] S. J. van Enk and O. Hirota, Entangled coherent states: Teleportation and decoherence, Phys. Rev. A **64**, 022313 (2001).
[25] H. Jeong, M. S. Kim, and J. Lee, Quantum-information processing for a coherent superposition state via a mixed entangled coherent channel, Phys. Rev. A **64**, 052308 (2001).
[26] J. Wenger, M. Hafezi, F. Grosshans, R. Tualle-Brouri, and P. Grangier, Maximal violation of Bell inequalities using continuous-variable measurements, Phys. Rev. A **67**, 012105 (2003).
[27] H. Jeong, W. Son, M. S. Kim, D. Ahn, and Č. Brukner, Quantum nonlocality test for continuous-variable states with dichotomic observables, Phys. Rev. A **67**, 012106 (2003).
[28] T. C. Ralph, A. Gilchrist, G. J. Milburn, W. J. Munro, and S. Glancy, Quantum computation with optical coherent states, Phys. Rev. A **68**, 042319 (2003).
[29] A. Gilchrist, K. Nemoto, W. J. Munro, T. C. Ralph, S. Glancy, S. L. Braunstein, and G. J. Milburn, Schrödinger cats and their power for quantum information processing, J. Opt. B **6**, S828 (2004).
[30] M. Stobińska, H. Jeong, and T. C. Ralph, Violation of Bell's inequality using classical measurements and nonlinear local operations, Phys. Rev. A **75**, 052105 (2007).
[31] A. P. Lund, T. C. Ralph, and H. L. Haselgrove, Fault-Tolerant Linear Optical Quantum Computing with Small-Amplitude Coherent States, Phys. Rev. Lett. **100**, 030503 (2008).
[32] Z. Leghtas, G. Kirchmair, B. Vlastakis, R. J. Schoelkopf, M. H. Devoret, and M. Mirrahimi, Hardware-Efficient Autonomous Quantum Memory Protection, Phys. Rev. Lett. **111**, 120501 (2013).
[33] D. J. Wineland, Nobel lecture: Superposition, entanglement, and raising Schrödinger's cat, Rev. Mod. Phys. **85**, 1103 (2013).
[34] S. Haroche, Nobel lecture: Controlling photons in a box and exploring the quantum to classical boundary, Rev. Mod. Phys. **85**, 1083 (2013).
[35] B. Vlastakis, G. Kirchmair, Z. Leghtas, S. E. Nigg, L. Frunzio, S. M. Girvin, M. Mirrahimi, M. H. Devoret, and R. J. Schoelkopf, Deterministically encoding quantum information using 100-photon Schrödinger cat states, Science **342**, 607 (2013).
[36] M. Mirrahimi, Z. Leghtas, V. V. Albert, S. Touzard, R. J. Schoelkopf, L. Jiang, and M. H. Devoret, Dynamically protected cat-qubits: A new paradigm for universal quantum computation, New J. Phys. **16**, 045014 (2014).
[37] C. Wang, Y. Y. Gao, P. Reinhold, R. W. Heeres, N. Ofek, K. Chou, C. Axline, M. Reagor, J. Blumoff, K. M. Sliwa, L. Frunzio, S. M. Girvin, L. Jiang, M. Mirrahimi, M. H. Devoret, and R. J. Schoelkopf, A Schrödinger cat living in two boxes, Science **352**, 1087 (2016).
[38] N. Ofek, A. Petrenko, R. Heeres, P. Reinhold, Z. Leghtas, B. Vlastakis, Y. Liu, L. Frunzio, S. M. Girvin, L. Jiang, M. Mirrahimi, M. H. Devoret, and R. J. Schoelkopf, Extending the lifetime of a quantum bit with error correction in superconducting circuits, Nature (London) **536**, 441 (2016).
[39] V. V. Albert, K. Noh, K. Duivenvoorden, D. J. Young, R. T. Brierley, P. Reinhold, C. Vuillot, L. Li, C. Shen, S. M. Girvin, B. M. Terhal, and L. Jiang, Performance and structure of single-mode bosonic codes, Phys. Rev. A **97**, 032346 (2018).
[40] B. Hacker, S. Welte, S. Daiss, A. Shaukat, S. Ritter, L. Li, and G. Rempe, Deterministic creation of entangled atom–light Schrödinger-cat states, Nat. Photon. **13**, 110 (2019).

[41] C. J. Villas-Bôas and M. H. Moussa, One-step generation of high-quality squeezed and EPR states in cavity QED, Eur. Phys. J. D **32**, 147 (2004).

[42] H.-S. Zeng, L.-M. Kuang, and K.-L. Gao, Two-mode squeezed states and their superposition in the motion of two trapped ions, Phys. Lett. A **300**, 427 (2002).

[43] A. Karimi, Superposition and entanglement of two-mode squeezed vacuum states, Int. J. Quantum Inf. **16**, 1850003 (2018).

[44] Z. Ficek and S. Swain, *Quantum Interference and Coherence: Theory and Experiments* (Springer, Heidelberg, 2005).

[45] H. Paul, Photon antibunching, Rev. Mod. Phys. **54**, 1061 (1982).

[46] D. Bhatti, J. von Zanthier, and G. S. Agarwal, Superbunching and nonclassicality as new hallmarks of superradiance, Sci. Rep. **5**, 17335 (2015).

[47] B. Bai, J. Liu, Y. Zhou, H. Zheng, H. Chen, S. Zhang, Y. He, F. Li, and Z. Xu, Photon superbunching of classical light in the Hanbury Brown–Twiss interferometer, J. Opt. Soc. Am. B **34**, 2081 (2017).

[48] Y. Zhou, F.-l. Li, B. Bai, H. Chen, J. Liu, Z. Xu, and H. Zheng, Superbunching pseudothermal light, Phys. Rev. A **95**, 053809 (2017).

[49] T. Lettau, H. A. M. Leymann, B. Melcher, and J. Wiersig, Superthermal photon bunching in terms of simple probability distributions, Phys. Rev. A **97**, 053835 (2018).

[50] J. Liu, J. Wang, H. Chen, H. Zheng, Y. Liu, Y. Zhou, F. li Li, and Z. Xu, High visibility temporal ghost imaging with classical light, Opt. Commun. **410**, 824 (2018).

[51] M. Marconi, J. Javaloyes, P. Hamel, F. Raineri, A. Levenson, and A. M. Yacomotti, Far-From-Equilibrium route to Superthermal Light in Bimodal Nanolasers, Phys. Rev. X **8**, 011013 (2018).

[52] L. Zhang, Y. Lu, D. Zhou, H. Zhang, L. Li, and G. Zhang, Superbunching effect of classical light with a digitally designed spatially phase-correlated wave front, Phys. Rev. A **99**, 063827 (2019).

[53] B. Lounis and M. Orrit, Single-photon sources, Rep. Prog. Phys. **68**, 1129 (2005).

[54] M. Penasa, S. Gerlich, T. Rybarczyk, V. Métillon, M. Brune, J. M. Raimond, S. Haroche, L. Davidovich, and I. Dotsenko, Measurement of a microwave field amplitude beyond the standard quantum limit, Phys. Rev. A **94**, 022313 (2016).

[55] A. Fedorov, A. K. Feofanov, P. Macha, P. Forn-Díaz, C. J. P. M. Harmans, and J. E. Mooij, Strong Coupling of a Quantum Oscillator to a Flux Qubit at Its Symmetry Point, Phys. Rev. Lett. **105**, 060503 (2010).

[56] D. Leibfried, R. Blatt, C. Monroe, and D. Wineland, Quantum dynamics of single trapped ions, Rev. Mod. Phys. **75**, 281 (2003).

[57] C. A. Regal, J. D. Teufel, and K. W. Lehnert, Measuring nanomechanical motion with a microwave cavity interferometer, Nat. Phys. **4**, 555 (2008).

[58] K. Duivenvoorden, B. M. Terhal, and D. Weigand, Single-mode displacement sensor, Phys. Rev. A **95**, 012305 (2017).

[59] C. M. Caves, K. S. Thorne, R. W. P. Drever, V. D. Sandberg, and M. Zimmermann, On the measurement of a weak classical force coupled to a quantum-mechanical oscillator. I. Issues of principle, Rev. Mod. Phys. **52**, 341 (1980).

[60] A. Facon, E.-K. Dietsche, D. Grosso, S. Haroche, J.-M. Raimond, M. Brune, and S. Gleyzes, A sensitive electrometer based on a Rydberg atom in a Schrödinger-cat state, Nature (London) **535**, 262 (2016).

[61] W. J. Munro, K. Nemoto, G. J. Milburn, and S. L. Braunstein, Weak-force detection with superposed coherent states, Phys. Rev. A **66**, 023819 (2002).

[62] N. Didier, A. Kamal, W. D. Oliver, A. Blais, and A. A. Clerk, Heisenberg-Limited Qubit Read-Out with Two-Mode Squeezed Light, Phys. Rev. Lett. **115**, 093604 (2015).

[63] S. Schreppler, N. Spethmann, N. Brahms, T. Botter, M. Barrios, and D. M. Stamper-Kurn, Optically measuring force near the standard quantum limit, Science **344**, 1486 (2014).

[64] D. Mason, J. Chen, M. Rossi, Y. Tsaturyan, and A. Schliesser, Continuous force and displacement measurement below the standard quantum limit, Nat. Phys. **15**, 745 (2019).

[65] W. Wang, Y. Wu, Y. Ma, W. Cai, L. Hu, X. Mu, Y. Xu, Z.-J. Chen, H. Wang, Y. P. Song, H. Yuan, C.-L. Zou, L.-M. Duan, and L. Sun, Heisenberg-limited single-mode quantum metrology in a superconducting circuit, Nat. Commun. **10**, 4382 (2019).

[66] M. Zwierz, C. A. Pérez-Delgado, and P. Kok, General Optimality of the Heisenberg Limit for Quantum Metrology, Phys. Rev. Lett. **105**, 180402 (2010).

[67] C. Gerry and P. L. Knight, *Introductory Quantum Optics* (Cambridge University, Cambridge, 2005).

[68] V. V. Dodonov and V. I. Man'ko, *Theory of Nonclassical States of Light* (Taylor & Francis, New York, 2003), and some references therein .

[69] A. Joshi and A.-S. F. Obada, Some statistical properties of the even and the odd negative binomial states, J. Phys. A: Math. Gen. **30**, 81 (1997).

[70] F. A. El-Orany, J. Peřina, and M. Sebawe Abdalla, Quantum properties of the parametric amplifier with and without pumping field fluctuations, Opt. Commun. **187**, 199 (2001).

[71] D. F. Walls and G. J. Milburn, *Quantum Optics* (Springer, Berlin, 2008).

[72] C. W. Helstrom, Quantum detection and estimation theory, J. Stat. Phys. **1**, 231 (1969).

[73] B. M. Escher, R. L. de Matos Filho, and L. Davidovich, General framework for estimating the ultimate precision limit in noisy quantum-enhanced metrology, Nat. Phys. **7**, 406 (2011); Quantum metrology for noisy systems, Braz. J. Phys. **41**, 229 (2011).

[74] R. A. Fisher, On the mathematical foundations of theoretical statistics, Philos. Trans. R. Soc. London Ser. A **222**, 309 (1922).

[75] R. A. Fisher, Theory of statistical estimation, Math. Proc. Camb. Philos. Soc. **22**, 700 (1925).

[76] H. Cramér, *Mathematical Methods of Statistics* (Princeton University Press, Princeton, 1999).

[77] C. R. Rao, *Linear Statistical Inference and its Applications* (Wiley, New York, 1973), Vol. 2.

[78] M. Woolley, G. Milburn, and C. M. Caves, Nonlinear quantum metrology using coupled nanomechanical resonators, New J. Phys. **10**, 125018 (2008).

[79] M. Napolitano and M. Mitchell, Nonlinear metrology with a quantum interface, New J. Phys. **12**, 093016 (2010).

[80] D. Tsarev, T. Ngo, R.-K. Lee, and A. Alodjants, Nonlinear quantum metrology with moving matter-wave solitons, New J. Phys. **21**, 083041 (2019).

[81] C. M. Caves, Quantum-mechanical noise in an interferometer, Phys. Rev. D **23**, 1693 (1981).

[82] L. Pezzé and A. Smerzi, Mach-Zehnder Interferometry at the Heisenberg Limit with Coherent and Squeezed-Vacuum Light, Phys. Rev. Lett. **100**, 073601 (2008).

[83] J. Sahota and N. Quesada, Quantum correlations in optical metrology: Heisenberg-limited phase estimation without mode entanglement, Phys. Rev. A **91**, 013808 (2015).

[84] L. G. Lutterbach and L. Davidovich, Method for Direct Measurement of the Wigner Function in Cavity QED and Ion Traps, Phys. Rev. Lett. **78**, 2547 (1997).

5 Detailed account of complexity for implementation of circuit-based quantum algorithms

frontiers in Physics

REVIEW
published: 01 November 2021
doi: 10.3389/fphy.2021.731007

Detailed Account of Complexity for Implementation of Circuit-Based Quantum Algorithms

Fernando R. Cardoso[1]*, *Daniel Yoshio Akamatsu*[1], *Vivaldo Leiria Campo Junior*[1], *Eduardo I. Duzzioni*[2], *Alfredo Jaramillo*[3] *and Celso J. Villas-Boas*[1]

[1]*Departamento de Física, Universidade Federal de São Carlos, São Carlos, Brazil,* [2]*Departamento de Física, Universidade Federal de Santa Catarina, Florianópolis, Brazil,* [3]*Escola de Engenharia de São Carlos, Universidade de São Paulo, São Carlos, Brazil*

In this review article, we are interested in the detailed analysis of complexity aspects of both time and space that arises from the implementation of a quantum algorithm on a quantum based hardware. In particular, some steps of the implementation, as the preparation of an arbitrary superposition state and readout of the final state, in most of the cases can surpass the complexity aspects of the algorithm itself. We present the complexity involved in the full implementation of circuit-based quantum algorithms, from state preparation to the number of measurements needed to obtain good statistics from the final states of the quantum system, in order to assess the overall space and time costs of the processes.

Keywords: quantum algorithms, quantum computation, quantum computational complexity, quantum tomography, quantum state preparation, quantum circuit model

OPEN ACCESS

Edited by:
Deniz Türkpençe,
Istanbul Technical University, Turkey

Reviewed by:
Jie-Hong Jiang,
National Taiwan University, Taiwan
Dongsheng Wang,
Institute of Theoretical Physics (CAS), China

***Correspondence:**
Fernando R. Cardoso
frc@df.ufscar.br

Specialty section:
This article was submitted to Quantum Engineering and Technology, a section of the journal Frontiers in Physics

Received: *25 June 2021*
Accepted: *20 September 2021*
Published: *01 November 2021*

Citation:
Cardoso FR, Akamatsu DY, Campo Junior VL, Duzzioni EI, Jaramillo A and Villas-Boas CJ (2021) Detailed Account of Complexity for Implementation of Circuit-Based Quantum Algorithms. Front. Phys. 9:731007. doi: 10.3389/fphy.2021.731007

1 INTRODUCTION

Quantum computing takes advantage of the unique properties of quantum mechanics, such as superposition and entanglement to carry out computational tasks in distinct ways than the classical computers do [1]. Since Richard Feynman's idealization that a quantum architecture would be a proper way to simulate actual quantum systems that occur in nature in the early 1980's [2], much attention has been given to the application of quantum systems for computational tasks. Among the greatest and most famous achievements of quantum information and quantum computation, one can cite superdense coding [3], the BB-84 algorithm for quantum public key distribution of cryptography systems [4], Shor's integer factoring algorithm [5], Grover's database search algorithm [6], alongside examples of no less importance or relevance. The advances have also reached important areas of mathematics and natural sciences in general, with quantum algorithms and circuit designing being developed to accomplish linear algebra tasks like eigen- [7, 8] and singular- value [9, 10] decompositions of matrices, finding solutions to linear systems of equations [11], solving linear [12–14] and nonlinear [15] differential equations, partial non-homogeneous linear differential equations [16], among other potential applications.

There have been recent progress in the current era of Noisy Intermediate Scale Quantum (NISQ) devices, such as problems that cannot be solved by any classical shallow circuits in reasonable time, but turns out to be possible by shallow quantum circuits [17], quantum supremacy using a superconducting quantum processor architecture achieved by Google team [18], and also quantum advantages over classical computation using boson sampling [19] and the simulation of quantum systems by means of quantum based architecture in D-Wave systems [20].

In general, the implementation of a quantum algorithm is based on many steps, that involve data pre-processing, preparation of input quantum states, the processing of the input information

through quantum gates and operations applied to the system, measurement of the final state of the composite quantum system, and post-processing of the data collected by the measurement process. In the present work, we will not deal with the pre- and post-processing steps, which are usually done by classical means. In most quantum algorithms, the quantum advantage over classical computation lies in the processing or evolution step, which takes advantage of the dimension of the Hilbert space of quantum systems and quantum parallelism to manipulate very large amounts of data, a task for which the present classical computers usually require exponential scaling resources, such as memory and state-of-the-art processors in supercomputer units. However, the preparation and measurement processes present in some quantum algorithms, which are essential for their proper implementations, are often neglected in their presentations, because of the intrinsic difficulties of these tasks.

The main purpose of this work is to perform a detailed analysis of the computational complexity defined by the space and time costs of quantum algorithms, considering all steps, from state preparation to readout processes. This work considers a scenario in which the rapid development of quantum computing has attracted the attention of people with different background, not only restricted to physicists or computer scientists from academia, but curious, investors, bankers, and entrepreneurs, which are delighted with the quantum speedups at first sight. Although quantum computing provides amazing results compared to its classical counterpart, a suitable interpretation of the algorithmic costs demands a proper analysis, which includes the circuit width, represented by the number of qubits necessary to carry on the tasks, as well as the circuit depth, which takes into account the number of quantum operations that must be implemented on the system for the proper processing of the information encoded in the qubit system. We are also concerned with the processes of recovering the resulting information of the processing, which can be represented by observable statistics or quantum tomography, depending on the task aimed by the quantum algorithm.

This work is organized as follows. In **section 2** the costs of state preparation using different schemes are covered. **Section 3** covers matrix and quantum gate decomposition and their complexity bounds. **Section 4** considers quantum state tomography, with emphasis on the required number of measurements and repetitions of the execution of a quantum algorithm to achieve a desired accuracy in the results. In **section 5**, the overall complexity aspects for implementation are given, from state preparation to readout process. Finally, **section 6** contains the conclusion of the work.

2 COMPLEXITY OF QUANTUM STATE PREPARATION

The need for preparation of quantum states as input for solving a given problem is a common task in many quantum algorithms implemented in the circuit model of Quantum Computation (QC) [1]. Such a preparation constitutes an important part in the process of implementation of a given algorithm for circuit gate-based quantum computing, as the final quantum state encoding the solution of the problem is directly linked to the input state through the evolution step. Thus, the complexity aspects of preparing the input state must be taken into account in a detailed resource analysis.

To describe the encoding of input states properly, we must split the entire quantum system that constitutes a quantum computer into two parts: the ancilla qubits, which are used, for instance, to encode relevant information and control logical operations, and the work system, that encodes the initial conditions of the problem to be solved, which is submitted to the evolution process defined by the quantum algorithm. For instance, consider the processes to encode the initial conditions for a linear differential equation [14] or for the HHL quantum linear problem [11] in the work system. The goal of state preparation is to initialize the system in a N-dimensional specific quantum superposition that is suitable to the problem to be solved on a quantum computer. This task is often accomplished by subroutines that, in quantum algorithms, are usually referred to as system encoding.

It is important to remark that there are different kinds of encoding, such as basis encoding and amplitude encoding: the former is often used when one needs to manipulate real numbers arithmetically, and the latter when one takes advantage of the large size of the Hilbert space to encode data as probability amplitudes [21]. As an example of basis encoding, let us see how a real number is encoded in a binary string. Suppose we must represent the real value vector $\vec{x} = (-0.3, 0.6)$. The first digit on the binary string encodes the sign of the number, in which a 0 stands for "+", and a 1 for "−" signs. The floating point is located immediately to the right of the sign bit. This will lead to the state vector $|x\rangle = |10100\ 01001\rangle$ in basis encoding [1]. Note that this representation is approximate, subjected to an error ε in its representation, which depends on the number of precision qubits employed. The exact representation of a decimal basis number into the binary basis would require more or less bits, according to the number to be represented. In general, assuming that the composite system starts from the configuration $|0\rangle^{\otimes n}$, those circuits present depth 1, as only one NOT operation may be executed on each qubit in parallel, depending on the binary representation that must be encoded. Examples of circuits for basis encoding are presented in detail in Ref. [22]. Basis encoded states can be used, for instance, to solve prime factorization problems [23], in machine learning techniques [24], and to encode the solution of the computation by quantum annealers [25].

For amplitude encoding, the relevant information for computation is stored in the probability amplitudes of the quantum state. The process usually starts from the n-qubit state $|0\rangle^{\otimes n}$, which is submitted to a transformation like

[1]A real number $x \in [0, 2)$ can be represented in binary basis as $x = \sum_{i=1}^{R} a_i 2^{-i}$, with $a_i \in \{0, 1\}$ and R is the number of precision bits. There are different strategies of covering the whole interval of real numbers.

$$|0\rangle^{\otimes n} \rightarrow |\psi\rangle = \sum_{i=0}^{N-1} c_i |i\rangle, \tag{1}$$

with $\sum_{i=0}^{N-1} |c_i|^2 = 1$, and each $|i\rangle$ corresponding to a given state vector of the N-dimensional computational basis, with $N = 2^n$. To address this task, one must be capable of preparing such a superposition preserving coherence properties. The costs of preparing such input states have been discussed in the literature [26–29]. The generic superposition can be prepared from the state $|0\rangle^{\otimes n}$ by the implementation of quantum gates that act directly upon the system to be prepared. These operations, and consequently, the cost of the procedure that aims to prepare a pure state, must be defined by the free parameters contained within $|\psi\rangle$, that is, a transformation $|\psi\rangle = U|0\rangle^{\otimes n}$, with $O(\tilde{N})$ [21, 30] gates, could be implemented, where $\tilde{N}$ corresponds to the number of free parameters. Since the number $\tilde{N}$ can be less than the total dimension of the system N, the process of preparing these bounded states can present a resulting cost that is cheaper than preparing the full upper bound case. Notice that, in the upper bound case, where $|\psi\rangle$ has 2^n free parameters, $\tilde{N} = N = 2^n$. This is often the case with general systems of differential or linear equations, where the degrees of freedom of the quantum state must encode the initial values of the variables within the problem. Nevertheless, there are cases where the state vector defining the initial conditions for a system to be evolved or simulated are defined by sparse vectors or specially bounded initial conditions. For instance, one can consider the study of the behavior and properties of spin chains [31], where often each site of the chain starts from a ground state configuration or with a few qubits representing the excited states of spins in the chain. This procedure of initialization has the advantages of being based on operations that act directly on the work qubits, without the presence of any ancilla systems which would increase the circuit width, whose operations are entirely defined by the free parameters of the initial state $|\psi\rangle$. On the other hand, it requires a number of quantum gates which grows with the number of free parameters. Although these gates can be executed in parallel, in each qubit, this scheme is better implemented when the initial conditions encoded in $|\psi\rangle$ are given by sparse configurations or specially bounded vectors.

The state initialization can follow the procedure described in detail in [26], which makes use of standard single- and controlled^k-operations, which are operations controlled by k qubits, acting on a single target. This method requires $O(N\log_2^2(N))$ single and two-qubit operations in total for executing a transformation like 1) without the introduction of additional quantum bits. One should also take notice of the presence of controlled^k-operations, that can be further decomposed into $O(k^2)$ single and two-qubit quantum gates [32]. The particular structure of these controlled operations increases the depth of its action throughout the components of the quantum system [26]. Soklakov and Schack presented a quantum algorithm [33] to prepare an arbitrary quantum register based on the Grover's search algorithm requiring resources that are polynomial in the number of qubits and additional gate operations.

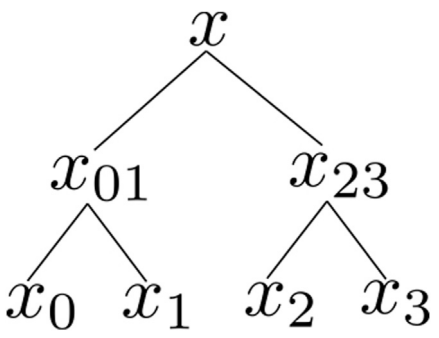

FIGURE 1 | Schematic representation of the Divide-and-Conquer algorithm for loading a four-dimensional vector x into a quantum state. The task of preparing $|x\rangle$ is divided into subtasks and can be represented as the logic tree shown above. Adapted from [34].

As an example of state preparation, the Divide-and-Conquer scheme [34] presents an algorithm for amplitude encoding in the form of a superposition like

$$|x\rangle = x_0|0\rangle|\psi_0\rangle + \cdots + x_{N-1}|N-1\rangle|\psi_{N-1}\rangle, \tag{2}$$

in which the qubits of the work and ancilla systems are entangled. So, although the system is prepared in a superposition state, the results after observation of ancilla qubtis will be left the work system as a mixed density matrix, what, in the case of algorithms for solving systems of linear or differential equations, this could be a disadvantage. Nevertheless, the algorithm is useful for machine learning and statistical analysis, and other applications, such as data sorting [34]. The algorithm structure presents the idea of dividing a problem into subproblems of the same class. The idea for creating the quantum superposition is to divide the problem like the scheme presented in **Figure 1**. The algorithm is based on the circuit model for quantum computing, which are presented in detail in [34], and presents space and time costs that scales as $O(N)$ and $O(\log_2^2(N))$, respectively.

The circuit for implementation of the Divide-and-Conquer algorithm for state preparation presents polylogarithmic depth and has a simplified structure, with the tasks divided into problems of the same class. It also presents the advantage of being based on the circuit model of computation, making its implementation simple as a subroutine for the main algorithm just by including the corresponding circuit in the state preparation step. However, this polylogarithmic depth comes at the cost of increasing the circuit width, as ancilla qubits are necessary to carry on its implementation. Thus, one can observe a trade-off between gate counts and number of qubits playing a significant role for this scheme.

Another state preparation scheme usually mentioned in quantum algorithms involves accessing a quantum database in which the quantum states are prepared in advance and can be quickly transferred to the working qubits. Below we describe this scheme in more detail, paying special attention to its complexity.

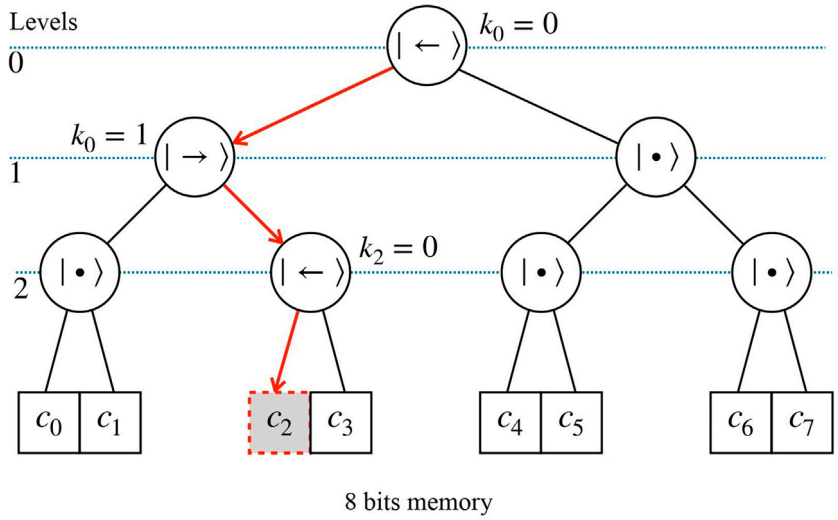

FIGURE 2 | Schematic representation of the BB architecture for a eight states qRAM. To address the memory cells only 3 = $\log_2(8)$ are needed. The nodes of the tree are composed by qutrits, which are initially in the wait state. The bit string determines the path to be followed by the bus signal, in which 0 means left path and 1 right path. Depending on the bits of the given string, the states of the qutrits are left in $|\leftarrow\rangle$ or $|\rightarrow\rangle$, and follows to the next level. Adapted from [38]. After returning by the same path to the beggining of the tree, the states return to the wait states.

2.1 Quantum Database and Quantum Random Access Memory

Employing calls on Random Access Memory (RAM) devices is an approach that aims to accomplish the task of preparation of quantum states by querying a database that contains the information of interest. For the purpose of querying a memory device with relevant information about the input state, one must be able to construct a database which consists in a set of state vectors containing the information for quantum computation. For instance, suppose a set of m vectors $S = \{\psi_1, \psi_2, \ldots, \psi_m\}$, each of them containing k components. The quantum equivalent of this database is the quantum associative memory representation [35] given by the uniform superposition of each state vector [21].

$$|S\rangle = \frac{1}{\sqrt{m}} \sum_{i=1}^{m} |\psi_i\rangle. \tag{3}$$

The cost for the creation of $|S\rangle$ scales as $O(mk)$ [21, 35]. Assuming that each $|\psi_i\rangle$ can be considered as a qubit system with dimension $k = N = 2^n$, this would require $O(mN)$ steps, which grows linearly (quadratically) with N in the best (worst) case. Grover's quantum search algorithm is often used as subroutine for querying databases with complexity $O\left(\sqrt{m}\log_2(m)\right)$ steps, while preparing and processing results of the query process would take $\Omega(m\log_2(N))$ steps [6].

There are other architectures for the implementation of quantum random access memory, such as the "Bucket Brigade" (BB) [36] and the Flip-Flop qRAM [37], which make use of different schemes to retrieve the content of a memory cell coherently. The BB architecture, for instance, is composed of a series of three-level quantum systems (qutrits), described by the states $|\bullet\rangle$, $|\leftarrow\rangle$ and $|\rightarrow\rangle$, which are used to guide a bus signal to the corresponding memory cell. A scheme to access a memory cell addressed by a 3-bit string is shown in **Figure 2**. In this architecture, each qubit in the address register is sequentially sent into the subsequent levels of the binary tree. These qubits then interact with the corresponding three-level system, whose initial state $|\bullet\rangle$ is changed to $|\leftarrow\rangle$ or $|\rightarrow\rangle$, depending on the address qubits. The three-level systems then act like a routing system which is used to guide a bus signal to the addressed memory cell. In this process, the state of the address qubits becomes entangled with the position state of the bus. The content of the cell is then transferred to the internal degrees of freedom of the bus signal by means of CNOT operations, whose number corresponds to the internal degrees of freedom that must be encoded. The signal is then sent backwards towards the path, and its position state

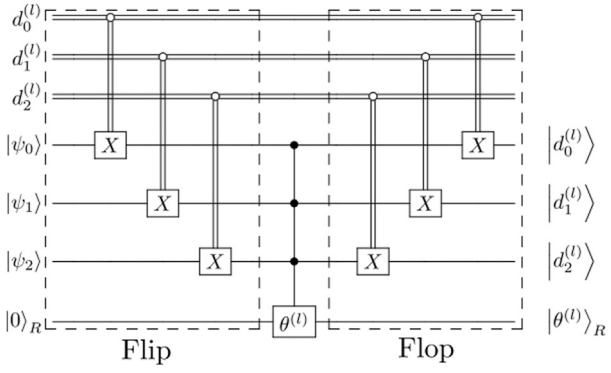

FIGURE 3 | Quantum circuit corresponding to one Flip-Flop iteration of the FF-qRAM algorithm. The classically-controlled operations X are applied to the states $|\psi_i\rangle$, and the register $|0\rangle_R$ can include the probability amplitudes for encoding. Note that the complete superposition creation requires the complete circuit implementation. Adapted from [37].

TABLE 1 | Resource Analysis of space and time for schemes of preparation (Free Parameters, BB—Bucket Brigade, Divide and Conquer, FF—Flip-Flop). The quantities in brackets represent the quantity of qutrits needed for the considered architecture.

Preparation scheme	Space costs	Time costs
Free Parameter	$O(\log_2(N))$	$O(\tilde{N})$
Divide and Conquer	$O(N)$	$O(\log_2^2(N))$
BB-qRAM	$O(\log_2(N) + [N])$	$O(\log_2^2(N))$
FF-qRAM	$O(\log_2(N))$	$O(\log_2(N))$

becomes uncorrelated with the address qubits. To complete the process, a SWAP operation is done between the internal degrees of freedom of the bus signal and the answer register. To completely construct the BB architecture for qRAM, $O(N)$ qutrits would be necessary, although only $O(\log_2(N))$ of those are activated for routing during one memory call. It has been shown that the BB architecture for quantum RAM accomplishes the task of retrieving the content of a memory cell coherently with $O(\log_2^2(N))$ [38] steps. The results can also be returned in a N-dimensional superposition form, if the bit string for addressing is given by a state of n qubits in superposition. The introduction of qutrit systems also has the effect of increasing the width of the circuit, as more quantum systems are introduced for its implementation. The architecture also presents the characteristic of not being suitable for quantum correction algorithms, as for the implementation of these, all the qutrits in the system would be activated, and this would make it equivalent to the usual FANOUT RAM architecture [36, 37]. Possible physical implementations of the BB architecture can be realized in quantum optical and solid state systems [36].

The Flip-Flop qRAM (FF-qRAM) [37] scheme has the advantage of being based on the circuit model for quantum computation, and thus can be implemented as a subroutine in the state preparation step of a quantum algorithm to generate a quantum database by just adding the circuit to the state preparation step. The circuit for one Flip-Flop iteration is shown in **Figure 3**. The operation executed by the complete circuit has the effect [37].

$$\mathrm{FF-QRAM}\sum_j |\psi_j\rangle|0\rangle_R = \sum_l |d^{(l)}\rangle|\theta^{(l)}\rangle_R, \tag{4}$$

where $|d^{(l)}\rangle$ encodes the string of the vector, and $|\theta^{(l)}\rangle_R = \cos(\theta^{(l)})|0\rangle_R + \sin(\theta^{(l)})|1\rangle_R$ represents the information about the amplitudes of encoding in superposition of the register qubit R. In this scheme, the CNOT operations applied to the qubits in the basis vectors $|\psi_j\rangle$ are classically controlled by the corresponding bits $d_i^{(l)}$. The gate denoted in the circuit by $\theta^{(l)}$ denotes a rotation on the register qubit to associate the probability amplitude to the qubits in the database. Note that the database qubits $|\psi_j\rangle$ can be in an arbitrary basis state, and the circuit has the effect of applying the controlled rotation $\theta^{(l)}$ only if the database state $|\psi_j\rangle$ matches the bit string $d^{(l)} = d_0^{(l)}d_1^{(l)}\ldots$, thus only associating the amplitude with the corresponding bit string.

According to Ref. [37], the costs of space and time amounts to $O(\log_2(N))$ qubits and $O(m\log_2(N))$ multi-qubit operations for creating superpositions of basis states with specific probability amplitudes on a quantum database such as represented by **Eq. 1**. The information can also be read and updated through repeated iterations of the Flip-Flop scheme. It has the advantage of not depending on proper routing algorithms, as it happens with the conventional and BB qRAM architectures [36], and is based on the quantum circuit computation model, what makes possible the application of quantum error-correction routines [37, 39–41]. The major disadvantage of the FF-qRAM architecture is the requirement of multi-controlled qubit rotations, whose cost can surpass the entire complexity of implementation for the whole FF-qRAM circuit, as the decomposition of such an operation can increase considerably the depth of the corresponding quantum circuit (see **Section 3**), depending on the architecture of the hardware in which it must be implemented.

In **Table 1**, the space and time costs for the preparation schemes are summarized. The BB based architecture for qRAM presents polylogarithmic time costs, as well as the Divide-and-Conquer algorithm, but needs $O(N)$ qutrits (represented in brackets), although only $O(\log_2(N))$ of these qutrits are activated during the process, and a proper routing algorithm, together with the $O(\log_2(N))$ address qubits for routing the bus signals to the corresponding the memory cells.

3 GATE DECOMPOSITION COMPLEXITY BOUNDS

Gate decomposition consists in the task of writing general operators that act upon a n-qubit system in the form of simpler gates that can be implemented in a quantum computer. For this purpose, different approaches and techniques have been developed, such as cosine-sine decomposition (CSD) [42], QR decomposition [43],[2] the Khaneja-Glaser decomposition (KGD) [44] among other methods with no less relevance.

In general, an arbitrary n-qubit gate U is represented by a $N \times N$ matrix, with N^2 degrees of freedom, that can be written as a product of $O(N^2)$ two-level unitary operations. To achieve such a decomposition, one can make use of a set of universal gates for computation, i.e., a set of one- and two-qubit operations from which any arbitrary operator U can be decomposed. For instance, it is known that the set of single-qubit and CNOT gates is universal [1]. With respect to the complexity regarding the implementation of U in terms of this universal set, the theoretical lower bound amounts to $\left\lceil \frac{1}{4}(N^2 - 3\log_2(N) - 1) \right\rceil$ CNOT operations [30].

Different approaches of circuit designing for gate decomposition are available in the literature. In particular, using the QR approach, the decomposition of U results in a quantum circuit with gate cost that amounts to $O(N^2\log_2^3(N))$ elementary operations [32]. Ref. [45] shows a circuit build in

[2]QR decomposition consists in decomposing an operator in a product of matrices, Q and R, each of which have particular properties.

which the CSD method is recursively applied together with uniformly controlled operations, resulting in a cost of $N^2 - 2N$ CNOTs and N^2 elementary single-qubit operations for implementing U. In [46], it is presented a circuit based on the use of Gray Codes [47], whose complexity bounds matches asymptotically the theoretical lower bound by reducing the gate cost from $O(N^2 \log_2(N))$ to $O(N^2)$ by elimination of superfluous control qubits from the corresponding quantum circuit.

Although the lower bound of CNOT gates for implementing an arbitrary U has an exponential cost in terms of the number of qubits n, it is possible to reduce the depth of a CNOT based circuit by the realization of a space-depth trade-off. This technique consists in the use of additional ancilla qubits, thus increasing the width of the quantum circuit, to parallelize the CNOT operations that must be realized throughout the circuit to implement the generic n-qubit gate U. The ideia was first demonstrated in [48], where it is proved that making use of $O(n^2)$ ancilla qubits, a n-qubit CNOT circuit can be parallelized to $O(\log_2(n))$ depth. It has been also already proved that each n-qubit CNOT circuit can be synthesized with $O\left(\frac{n^2}{\log_2(n)}\right)$ CNOT gates [49]. These results were recently improved [50], showing that it is possible to reduce the number of ancilla qubits presented in [49] by a factor of $\log_2^2(n)$, resulting that $m = \left(\frac{n^2}{\log_2^2(n)}\right)$ auxiliary qubits suffice to build $O(\log_2(n))$-depth circuits, and also, to reduce the depth presented in [49] by a factor of n, thus achieving the asymptotically optimal bound of $O\left(\frac{n}{\log_2(n)}\right)$. This optimization in space-depth trade-off is summarized in the following way [50]: For any integer $m \geq 0$, any n-qubit CNOT circuit can be parallelized to $O\left(\max\left\{\log_2(n), \frac{n^2}{(n+m)\log_2(n+m)}\right\}\right)$, with m standing for the number of ancillas in the composed system.

Thus, besides the exponential complexity of decomposing arbitrary n-qubit unitary operators, the space-depth trade-off presents an alternative in optimizing the circuit synthesis. Nevertheless, it is worth to consider that this parallel approach requires additional qubits to make the trade-off, having the immediate effect of increasing the circuit width of a quantum algorithm. It is also worth noting that different architectures for quantum computing may present different sets of basic gates in which the quantum operations must be decomposed, and also other different important aspects, such as connectivity, making the costs of decomposition and implementation of gates also dependent on the architecture of the quantum computer.

4 COMPLEXITY OF QUANTUM STATE TOMOGRAPHY

Quantum state tomography (QST) is a procedure that aims for the complete reconstruction of an unknown density matrix ρ [1]. Often, for information encoded in amplitudes or phases of a quantum state, after executing a quantum algorithm, one is presented with a density matrix whose elements (ρ_{ij}) codify the algorithm's output [51]. Information encoded in the complex amplitudes of a quantum state is not directly accessible through trivial means [1]. Thus, QST could represent a fundamental step in the knowledge of obtaining the full solution of a given problem. This consideration is important for a proper comparison between quantum and classical algorithms in which the quantum solution is a superposition state while the classical solution is a vector where all coefficients are known [52]. At the same time quantum information can be stored in a Hilbert space whose dimension increases exponentially according to the number of qubits. To retrieve such information it is necessary to pay the price for that, which also requires exponential steps. Alternatively, some global properties of the solution could be obtained by means of the expectation values of some observables, i.e., $O_k = \mathrm{Tr}(O_k\rho)$ [51]. This later approach usually conducts to quantum advantage in the processing time, however, it is not straightforward to get from average values of observables the desired quantities usually employed in practical applications of quantum computing. In this way, the impact of the QST complexity on the overall costs of quantum algorithms must be carefully considered.

There are many quantum algorithms whose output state has coherence in the computational basis. There are algorithms to solve partial differential equations [53–59], linear differential equations [12–14], nonlinear differential equations [60], linear system of equations (also named quantum linear problem) [61, 62]. In these examples, QST may be required depending on the level of detail expected to be known.

There is a variety of QST processes and schemes available to accomplish the characterization task, such as Simple Quantum State Tomography (SQST) [1], Ancilla Assisted Process Tomography[3] (AAPT) [63], QST *via* Linear Regression Estimation [64], Compressed-Sensing QST [65], Principal Component Analysis [66], efficient process tomography [67] and permutationally invariant tomography schemes [68, 69], each of these with particular complexity aspects, being suitable for specific problems. Their different computational costs arise from taking advantage of particular characteristics of ρ.

In general, QST is based on the decomposition of the density matrix in a linear combination of basis operators. For a system of n qubits, the reconstruction of a density matrix ρ in such space requires $4^n - 1 = N^2 - 1$ basis operators [1], which scales polynomially in the dimension $O(N^2)$. These exponential aspects of complexity are well known [70]. Besides the number of basis operators needed for characterization, it is important to remind that the reconstruction of ρ is based on expectation values of those basis operators. For instance, in the case of a single qubit, the set of $4^1 - 1 = 3$ basis operators needed for the proper quantum statistics could be based on the Pauli matrices X, Y, and Z, such that

$$\rho = \frac{1}{2}\left[\mathrm{Tr}(\rho)\mathcal{I} + \mathrm{Tr}(\rho X)X + \mathrm{Tr}(\rho Y)Y + \mathrm{Tr}(\rho Z)Z\right], \quad (5)$$

[3]Although Ref. [63] discusses quantum process tomography, a QST procedure is needed in order to complete the protocol in SQPT and AAPT schemes, and an insight about the complexity of quantum state tomography can be obtained.

where $\mathcal{I}$ is the identity operator. This statistical approach requires ensemble measurements of these observables, thus requiring a large number of copies of ρ [1]. Besides these fundamental concepts, it has been shown that by using machine learning theory one could learn information about ρ by a number of measurements that grow linearly with n [71]. Ref. [51] gives a detailed description of the number of measurements and the scaling of the physical resources of the system. There are also models in which the QST problem is converted into a parameter estimation problem such as linear regression [72], for which the computational complexity scales as $O(N^4)$.

The overall costs of implementation [4] yielded from SQST is $O(N^4 \log_2(N))$, and the same relation holds for AAPT using Joint Separable Measurement (JSM) scheme. Both SQST and AAPT-JSM require only single body interactions [51], while the Mutually Unbiased Bases (MUB) and the generalized POVM AAPT-schemes require many-body interactions. The costs for MUB scale as $O\left(N^2\log_2^2(N)\right)[O\left(N^2\log_2^3(N)\right)]$ under presence of nonlocal [local] two-body interactions, and the POVM scheme as $O(N^4)$ measurements on a single copy of the density matrix. The particular aspects of complexity of these schemes of tomography must take into account the required type of interactions between qubits, as nonlocal interactions may be not available in all architectures for quantum computation, which would represent a difficulty for its implementations. It is also worth noticing that AAPT-based schemes require the presence of ancillary systems, which, in practice, have the effect of increasing the system width. SQST has the ability of characterizing the full density matrix of a quantum system, including all probabilities and relative phases, but with a cost exponentially large with respect to the number of qubits that compose the system, making its implementation impractical to characterize output states of circuits with large width of the work system. The Quantum Principal Component Analysis (QPCA) [73], widely applied in machine learning techniques, focuses on reconstructing the eigenvectors of ρ corresponding to the largest eigenvalues of the system in a particular region of the space $\mathcal{H}$, in time $O(R\log_2(N))$. The full density matrix reconstruction can also be realized with QPCA process, in a number of time steps that amounts to $O(RN\log_2(N))$ [73]. Compressed-Sensing, in contrast, reconstructs the full density matrix of the system in $O\left(RN\log_2^2(N)\right)$ time steps [74]. In particular, the basic idea of Compressed-Sensing is that a low-rank density matrix can be estimated with fewer copies of the state, as the sample complexity depends on its rank R. Ref. [71] introduces the matrix Dantzig selector and matrix Lasso estimators, with sample complexity for obtaining an estimate accurate within ε in trace distance scaling as $O(\frac{R^2N^2}{\epsilon^2}\log_2(N))$ for rank-R states, requiring measuring of $O(RN\text{polylog}(N))$ Pauli expectation values. Finally, in the case where the final density matrix of the work qubits ends up in a state which is permutationally invariant (PI), the tomographic method presented in [68, 69] requires only $O\left(\log_2^2(N)\right)$ operations. If the density matrix is not perfectly invariant under qubit permutation, the method still provides a satisfactory result at least for those cases where the order of the qubits is not relevant. The PI method is best suited for the tomography of systems which present symmetric quantum states, like Dicke states [72] or spin squeezed states [73].

In practice, all of the costs rising from measurement schemes used for obtaining prior information about the systems under consideration will increase the overall cost of its implementation in quantum computing devices, which will be brought together in **section 5**. The cost of tomography schemes are brought together in **Table 2**.

TABLE 2 | Resource Analysis for schemes of tomography of quantum states. The schemes presented consists of Standard Quantum State Tomography (SQST), Joint Separable Measurements (JSM), Mutual Unbiased Measurements (MUB), Positive Operator Valued Measurements (POVM), Quantum Principal Component Analysis (QPCA), Compressed-Sensing (CS) and the Permutationally Invariant Quantum Tomography (PI) scheme. Note that QPCA process can be used to reconstruct large eigenvalues of the Hilbert space, as well as the full density matrix (QPCA Full).

Tomography scheme	Overall process cost
SQST/JSM	$O(N^4 \log_2(N))$
MUB	$O\left(N^2\log_2^2(N)\right)$
POVM	$O(N^4)$
QPCA	$O(R\log_2(N))$
CS	$O\left(RN\log_2^2(N)\right)$
QPCA (Full)	$O(RN\log_2(N))$
PI	$O\left(\log_2^2(N)\right)$

4.1 Pure State Tomography

There exist certain procedures where one is not interested in the full description of the resulting state ρ (e.g., some special cases of the algorithm in [14]). Instead, let us assume that the output of the algorithm is fully codified in the squares of the state's amplitudes, i.e., if $|\Psi\rangle = \sum_{m=1}^{N}\langle m|\Psi\rangle|m\rangle$ is the output of the algorithm, then all one needs to know is each $|\langle m|\Psi\rangle|^2$. More generally, one may be interested in knowing the square of the amplitudes associated to only a subspace of $\mathcal{H}$. An example of this is considered in [74], where it is assumed that the output of the algorithm can be written as

$$|\Psi\rangle = \frac{1}{\mathcal{N}}\left(|0\rangle|\Psi_0\rangle + |1\rangle|\Psi_1\rangle\right), \tag{6}$$

where the first qubit is an auxiliary one, $|\Psi_0\rangle = \sum_{m=1}^{N}\alpha_m|m\rangle$ is the target state (written in terms of the computational basis of the subsystem), $|\Psi_1\rangle$ is an arbitrary state, and $\mathcal{N}$ is a normalization constant that may depend on N. The probability of success p corresponds to the probability of the auxiliar qubit to be found in the state $|0\rangle$, which may be computed as

$$p = \frac{\langle\Psi_0|\Psi_0\rangle}{\mathcal{N}^2}. \tag{7}$$

Moreover, the probability of the system to be found in the state $|0\rangle|m\rangle$ is $p_m = |\alpha_m|^2/\mathcal{N}^2$, here assumed to be non-null for every

[4]The overall complexity is defined as in [51], given by the number of copies of ρ times the number of gates per measurement.

m. As explained in [51], each p_m is possible to be estimated by performing M_m independent measurements, each measurement requiring one copy of $|\Psi\rangle$. After these trials, the probability p_m is estimated as $\bar{p}_m = n_m/M_m$, where n_m is the number of occurrences of $|0\rangle|m\rangle$. By statistical arguments, in Ref. [51] it is shown that the number of trials necessary to estimate p_m up to a relative precision Δ with probability $1 - \varepsilon$ [5], denoted by $M_m(\Delta, \varepsilon)$, is bounded as

$$M_m \geq p_m^{-1} C(\triangle, \epsilon) , \tag{8}$$

where $C(\triangle, \epsilon) \equiv \frac{3}{\Delta^2}\log_2(1/\epsilon)$ does not depend on the system's size. Denoting now the square of the normalized amplitude by $\beta_m^2 \equiv |\alpha_m|^2\langle\Psi_0|\Psi_0\rangle$, then $p_m = |\alpha_m|^2/\mathcal{N}^2 = p\,\beta_m^2$, and thus, from **Eq. 8**, the behavior of M_m can be determined from the behavior of p and β_m^2 in terms of N. Finally, let's assume that each $|\alpha_m|^2$ goes to 0 at the same rate as N grows, i.e., $|\alpha_m|^2 = O(N^{-r})$ for $r > 0$ and all m. A particular case of the last occurs when the discrete probability distribution $\{\beta_m^2\}$ is fairly uniform, for which $r = 1$. Therefore, since $\beta_m^2 = |\alpha_m|^2/\sum_m|\alpha_m|^2$, one has that $\beta_m^2 = 1/N$ and from **Eq. 8** the number of copies of $|\Psi\rangle$ necessary to determine each p_m, that can be taken as $M = \max_m M_m$, is such that

$$M \geq O\left(p^{-1}\left(\min_m \beta_m^2\right)^{-1}\right) = O(p^{-1}N) . \tag{9}$$

We conclude that if p has a non-null minimum as a function of N, then the computational complexity of the tomography of all the p_i is of order N. Otherwise, one needs to determine the asymptotic behavior of the success probability p as N grows (e.g. Ref. [14]).

5 OVERALL COMPLEXITY OF IMPLEMENTATION

The overall complexity for implementation of a quantum algorithm accounts for all tasks that must be executed. It must take into account the total resource aspect, such as the number of work and ancilla qubits, represented by the width of the circuit, that could eventually include qRAM systems, as well as the usual gate cost aspect, brought together with the number of measurements. The last accounts for the number of copies times the number of measurements per copy done upon the final state in order to reconstruct its proper statistical averages and features.

Space costs: As discussed in **section 2**, the preparation of a generic superposition can be done by manipulating the work system, by the application of quantum gates that correspond to the transformations defined by the free parameters of the state. This results in a space cost which corresponds to the dimension of the work system alone. Assuming that such system has a Hilbert space dimension corresponding to a n-qubit space, it results in $O(\log_2(N))$ qubits needed for its implementation. The Divide-and-Conquer scheme requires a circuit width which have a space cost of $O(N)$ for implementation, but it is worth noting that it makes use of ancilla qubits that are left entangled with the work system. The discussed schemes for qRAM have similar aspects of qubit resources, but the presence of routing and $O(N)$ qutrits (although this is not the number of activated qutrits during a memory call) in the BB architecture makes it less favorable for the implementation of gate-based algorithms for computation.

Gate or time costs: For the analysis of the corresponding overall gate complexity of an implementation, we need to consider also the amount of identical copies of ρ needed for its proper reconstruction, given a determined scheme for the task [51]. The overall cost of these schemes will appear as a multiplying factor in the full time cost analysis, since all the operations in the implementation of the quantum algorithm, from preparation to readout, should be done this corresponding number of times.

Preparation: The overall time cost of the preparation step depends on whether it is implemented by operating directly on the work system based on the free parameters of the state, or by queries made upon a previously prepared quantum RAM device [6]. With preparation based on the free parameters, the amount of quantum operations has the upper bound of $O(N)$ for preparing a N-dimensional quantum superposition. The Divide-and-Conquer quantum algorithm can create an entangled superposition between ancilla and work systems, with a $O(\log_2^2(N))$ circuit depth. The Bucket-Brigade qRAM architecture [36] also presents $O(\log_2^2(N))$ time steps, as discussed in **section 2**. The preparation implemented *via* FF-qRAM scheme is fully based on the quantum circuit computation model, without any routing algorithm to address the memory cells that must be queried throughout the transformation represented by **Eq. 1**. The number of gate operations in the FF-qRAM sums up to $O(\log_2(N))$ [37].

Evolution: We define the expression *evolution* to denote the process in which the previously prepared work system is evolved to its last configuration, which could represent, for instance, the solution of a system of linear equations [11], a system of coupled differential equations [14], among other examples of possible applications for quantum computation. The quantum algorithm is composed by a sequence of defined steps and operations, which transforms the initial state under linear operations, that can be controlled by ancilla qubits that compose the full system under consideration. The evolution process will be denoted here as a linear map, represented by ε, as in Ref. [49]. The gate and resource costs of a given algorithm depend on the tasks that may be executed through its implementation, so different quantum algorithms have distinct space and time costs. To represent generically the time cost of the processing step of the algorithm, we will define a function $C(\varepsilon)$, of which one excludes the steps of preparation and measurement of the quantum states.

[5]This exactly means that $|\bar{p}_m - p_m|/|p_m| \leq \Delta$ with probability $1 - \varepsilon$.

[6]The complexity of preparing a quantum RAM device is beyond the scope of the present work.

TABLE 3 | Gate Complexity Analysis for various schemes of preparation (FP - Free Parameters, DC—Divide-and-Conquer, BB—Bucket Brigade, FF—Flip-Flop) and readout—Measurement procedures. The quantities in brackets are only taken into account if the system shows local interaction between qubits, in the case of the MUB sheme only. $C(\varepsilon)$ stands only for the time cost of the evolution stage of the quantum algorithm, represented *via* the linear map ε.

	Overall gate complexity		
Meas.Prep	FP	DC/BB-qRAM	FF-qRAM
SQTP/JSM	$O(N^4 \log_2(N)(N + C(\varepsilon)))$	$O(N^4 \log_2(N)(\log_2^2(N) + C(\varepsilon)))$	$O(N^4 \log_2(N) \log_2(N) + C(\varepsilon))$
MUB	$O(N^2 \log_2^2(N)[\log_2^3(N)](N + C(\varepsilon)))$	$O(N^2 \log_2^2(N)[\log_2^3(N)](\log_2^2(N) + C(\varepsilon)))$	$O(N^2 \log_2^2(N)[\log_2^3(N)](\log_2(N) + C(\varepsilon)))$
POVM	$O(N + C(\varepsilon) + N^4)$	$O(\log_2^2(N) + C(\varepsilon) + N^4)$	$O(\log_2(N) + C(\varepsilon) + N^4)$

TABLE 4 | Quantum algorithms and possible choices for input state preparation and tomography schemes.

Algorithm	State preparation	Tomography scheme
Quantum Simulation/ Systems with sparse/ specially bounded conditions	Free-parameter gate-based preparation	QPCA/ Compressed-Sensing
Machine Learning Techniques	Divide-and-Conquer algorithm	QPCA
Systems of linear/ differential equations with non-sparse initial conditions	BB-qRAM FF-qRAM	SQTP/JSM POVM QPCA (Full) Compressed-Sensing

Readout: The readout aspect must bring the analysis of the number of gates per measurement necessary to characterize a N-dimensional quantum system. For both SQTP and AAPT-JSM, $O(\log_2(N))$ single qubit operations must be implemented in order to reconstruct the density matrix. For AAPT-MUB based schemes, one needs $O(\log_2^2(N))$ $[O(\log_2^3(N))]$ single- and two-qubit gates, given that nonlocal [local] correlations occur in the system. The POVM scheme gate cost scales as $O(N^4)$ [49] operations per measurement. There are, also, particular methods of reconstruction for ρ, such as QPCA [67] and Compressed-sensing, which are capable of reconstructing the density matrix with a number of gates up to $O(R\log_2(N))$ and $O(RN\log_2^2(N))$ respectively, where R stands for the rank of the density matrix under reconstruction [65]. For systems which are permutationally invariant, the PI tomography scheme presents a measerement cost which scales quadratically with the number of qubits of the composed system [66, 67]. The PI method also presents approximate results of the density matrix being measured when the system is not invariant under permutations. For the application of those techniques, some knowledge of ρ must be needed, such as the existence of larger eigenvalues in some regions of the composed Hilbert space [67] and sparsity of ρ. Since we assume that no prior information about ρ is known, we shall not discuss these in the overall complexity analysis.

Overall Complexity: The overall gate cost for implementation of a quantum algorithm will now be classified according to each of the techniques discussed in the previous sections, including preparation and measurement schemes. The first multiplicative factors in each of the bounds presented stands for the number of experimental samples needed for each measurement scheme, which will be $O(N^4 \log_2(N))$ for both SQTP and JSM, $O(N^2\log_2^2(N))[\log_2^3(N)]$ for MUB, and $O(1)$ for POVM. We will not bring to this particular analysis the QPCA and Compressed-Sensing methods, since we suppose no further information (like the rank R) of the density matrix is known. For each of the considered preparation methods, the free parameter has the upper bound of $O(N)$ operations, while both of the divide-and-conquer algorithm and the BB-qRAM architecture present the same upper bound of $O(\log_2^2(N))$ quantum operations for preparing a state in a generic superposition. Using FF-qRAM, this bound is improved to $O(\log_2(N))$ operations. The evolution cost is generically represented by the function $C(\varepsilon)$. These information are brought all together in **Table 3**. We also present the possible choices of state preparation and measurement schemes suitable for tasks often approached by circuit-based quantum algorithms in **Table 4**.

6 CONCLUSION

We have presented a theoretic overview of the total complexity for the implementation of circuit-based quantum algorithms, involving the codification of the system parameters in the initial state of the work/register qubits, the evolution step towards the final state encoding the solution of the problem and the readout of this solution. A comparison between several schemes of preparation of input states as well as of tomography of final states was provided.

It is important to notice that algorithms that depend on the preparation of input states as superpositions of the basis states have at least $O(\tilde{N})$ gate operations based on the number of free parameters, $\tilde{N}$, defined by the initial state of the work qubits. Once a FF-qRAM device is available, this complexity can be reduced to $O(\log_2(\tilde{N}))$, which means to be linear in the number of qubits.

The evolution step can be represented by a linear map ε of the initial state to the final state. Its time cost, $C(\varepsilon)$, is strongly dependent on the quantum algorithm, and usually shows an exponential speedup compared to the classical algorithm solving the same problem. The origin of such speedup comes from the nature of the Hilbert space, i.e., the ability of a given number of qubits to encode an exponential number of states. Concerning the readout of the solution encoded in the final state, we have done a generic analysis assuming a fairly uniform probability distribution over the basis states of the Hilbert space. In this case, if the desired result is encoded in a single amplitude of a given basis state, the number of required ensemble copies will scale as $O(N)$ in the best scenario. This means a cost that is at least exponential in number of qubits. It is also important to mention that expectation values of observables which

represent global features of the solution can be realized as a method to avoid the full tomography of the system [11]. Combining this fact with the classical shadows technique [75] for measurements, it is possible to diminish even more the overall quantum algorithmic complexity.

Therefore, for algorithms depending upon the preparation of a superposition state, for which the solution is encoded in the final superposition state of the work qubits, the overall complexity to obtain the solution will be at least $O(N\log_2(N)C(\varepsilon))$, which can be significantly higher than $C(\varepsilon)$. We point out that this complexity overview also depends on the architecture of the quantum hardware in which the algorithm should be implemented, and the availability of basic quantum gates for proper decomposition of all operations needed in the process of implementation.

AUTHOR CONTRIBUTIONS

FC contributed mainly in the manuscritpt production. DA contributed in reviewing tomography schemes. VC reviewed and corrected the main text. ED reviewed and corrected the main text. AJ contributed with discussions and writing in probability of success of the algorithms and tomography. CV supervised the work, contributed to the manuscript and discussions.

FUNDING

São Paulo Research Foundation (FAPESP), Grant No. 2019/11999-5 Brazilian National Institute of Science and Technology for Quantum Information (INCT-IQ/CNPq) Grant No. 465469/2014-0. This work was supported by the Coordenação de Aperfeiçoamento de Pessoal de Nível Superior (CAPES)—Finance Code 001, and through the CAPES/STINT project, grant No. 88881.304807/2018-01. CV is also grateful for the support by the São Paulo Research Foundation (FAPESP) Grant No. 2019/11999-5, and the National Council for Scientific and Technological Development (CNPq) Grant No. 307077/2018-7. This work is also part of the Brazilian National Institute of Science and Technology for Quantum Information (INCT-IQ/CNPq) Grant No. 465469/2014-0.

REFERENCES

1. Nielsen MA, and Chuang I. *Quantum computation and quantum information*. Cambridge: Cambridge University Press (2002).
2. Feynman RP. Simulating physics with computers. *Int J Theor Phys* (1982) 21. doi:10.1007/bf02650179
3. Bennett CH, and Wiesner SJ. Communication via one- and two-particle operators on einstein-podolsky-rosen states. *Phys Rev Lett* (1992) 69: 2881–4. doi:10.1103/physrevlett.69.2881
4. Bennett CH, and Brassard G. *Quantum cryptography: Public key distribution and coin tossing* (1984). arXiv preprint arXiv:2003.06557.
5. Shor PW. Algorithms for quantum computation: discrete logarithms and factoring. *Ieee* (1994). p. 124–34.
6. Grover LK. Quantum computers can search arbitrarily large databases by a single query. *Phys Rev Lett* (1997) 79:4709–12. doi:10.1103/physrevlett.79.4709
7. Abrams DS, and Lloyd S. Quantum algorithm providing exponential speed increase for finding eigenvalues and eigenvectors. *Phys Rev Lett* (1999) 83: 5162–5. doi:10.1103/physrevlett.83.5162
8. Zhou X-Q, Kalasuwan P, Ralph TC, and O'Brien JL. Calculating unknown eigenvalues with a quantum algorithm. *Nat Photon* (2013) 7:223–8. doi:10.1038/nphoton.2012.360
9. Rebentrost P, Steffens A, Marvian I, and Lloyd S. Quantum singular-value decomposition of nonsparse low-rank matrices. *Phys Rev A* (2018) 97:012327. doi:10.1103/physreva.97.012327
10. Gilyén A, Su Y, Low GH, and Wiebe N. Quantum singular value transformation and beyond: exponential improvements for quantum matrix arithmetics. InProceedings of the 51st Annual ACM SIGACT Symposium on Theory of Computing, 2019 Jun (2019). p. 193–204. doi:10.1145/3313276.3316366
11. Harrow AW, Hassidim A, and Lloyd S. Quantum algorithm for linear systems of equations. *Phys Rev Lett* (2009) 103:150502. doi:10.1103/physrevlett.103.150502
12. Berry DW. High-order quantum algorithm for solving linear differential equations. *J Phys A: Math Theor* (2014) 47:105301. doi:10.1088/1751-8113/47/10/105301
13. Berry DW, Childs AM, Ostrander A, and Wang G. Quantum algorithm for linear differential equations with exponentially improved dependence on precision. *Commun Math Phys* (2017) 356:1057–81. doi:10.1007/s00220-017-3002-y
14. Xin T, Wei S, Cui J, Xiao J, Arrazola In., Lamata L, et al. Quantum algorithm for solving linear differential equations: Theory and experiment. *Phys Rev A* (2020) 101:032307. doi:10.1103/physreva.101.032307
15. Leyton SK, and Osborne TJ. *A quantum algorithm to solve nonlinear differential equations* (2008). arXiv:0812.4423 [quant-ph].
16. Arrazola JM, Kalajdzievski T, Weedbrook C, and Lloyd S. Quantum algorithm for nonhomogeneous linear partial differential equations. *Phys Rev A* (2019) 100:032306. doi:10.1103/physreva.100.032306
17. Bravyi S, Gosset D, König R, and Tomamichel M. Quantum advantage with noisy shallow circuits. *Nat Phys* (2020) 16:1040–5. doi:10.1038/s41567-020-0948-z
18. Arute F, Arya K, Babbush R, Bacon D, Bardin JC, Barends R, et al. supremacy using a programmable superconducting processor. *Nature* (2019) 574:505. doi:10.1038/s41586-019-1666-5
19. Zhong H-S, Wang H, Deng Y-H, Chen M-C, Peng L-C, Luo Y-H, et al. Quantum computational advantage using photons. *Science* (2020) 370:1460. doi:10.1126/science.abe8770
20. King AD, Raymond J, Lanting T, Isakov SV, Mohseni M, Poulin-Lamarre G, et al. Scaling advantage over path-integral monte carlo in quantum simulation of geometrically frustrated magnets. *Nat Commun* (2021) 12:1. doi:10.1038/s41467-021-20901-5
21. Leymann F, and Barzen J. The bitter truth about gate-based quantum algorithms in the NISQ era. *Quan Sci Tech* (2020) 5:044007. doi:10.1088/2058-9565/abae7d
22. Cortese JA, and Braje TM. *Loading classical data into a quantum computer* (2018). arXiv preprint arXiv:1803.01958.
23. Jiang S, Britt KA, McCaskey AJ, Humble TS, and Kais S. Quantum annealing for prime factorization. *Scientific Rep* (2018) 8(17667):1. doi:10.1038/s41598-018-36058-z
24. Neven H, Denchev VS, Rose G, and Macready WG. *Training a binary classifier with the quantum adiabatic algorithm* (2008). arXiv preprint arXiv:0811.0416.
25. Das A, and Chakrabarti BK. Colloquium: Quantum annealing and analog quantum computation. *Rev Mod Phys* (2008) 80:1061. doi:10.1103/revmodphys.80.1061
26. Long G-L, and Sun Y. Efficient scheme for initializing a quantum register with an arbitrary superposed state. *Phys Rev A* (2001) 64:014303. doi:10.1103/physreva.64.014303
27. Andrecut M, and Ali M. Efficient algorithm for initializing amplitude distribution of a quantum register. *Mod Phys Lett B* (2001) 15:1259. doi:10.1142/s0217984901003093
28. Ward NJ, Kassal I, and Aspuru-Guzik A. Preparation of many-body states for quantum simulation. *J Chem Phys* (2009) 130:194105. doi:10.1063/1.3115177
29. Girolami D. How difficult is it to prepare a quantum state?. *Phys Rev Lett* (2019) 122:010505. doi:10.1103/PhysRevLett.122.010505

30. Shende VV, and Markov IL. *Quantum circuits for incompletely specified two-qubit operators* (2004). arXiv preprint quant-ph/0401162.
31. Halimeh JC, and Zauner-Stauber V. Dynamical phase diagram of quantum spin chains with long-range interactions. *Phys Rev B* (2017) 96:134427. doi:10.1103/physrevb.96.134427
32. Barenco A, Bennett CH, Cleve R, DiVincenzo DP, Margolus N, Shor P, et al. Elementary gates for quantum computation. *Phys Rev A* (1995) 52:3457. doi:10.1103/physreva.52.3457
33. Soklakov AN, and Schack R. Efficient state preparation for a register of quantum bits. *Phys Rev A* (2006) 73:012307. doi:10.1103/physreva.73.012307
34. Araujo IF, Park DK, Petruccione F, and da Silva AJ. A divide-and-conquer algorithm for quantum state preparation. *Scientific Rep* (2021) 11:1. doi:10.1038/s41598-021-85474-1
35. Ventura D, and Martinez T. Quantum associative memory. *Inf Sci* (2000) 124: 273. doi:10.1016/s0020-0255(99)00101-2
36. Giovannetti V, Lloyd S, and Maccone L. Architectures for a quantum random access memory. *Phys Rev A* (2008) 78:052310. doi:10.1103/PhysRevLett.100.160501
37. Park D, Petruccione F, and Rhee J. Circuit-based quantum random access memory for classical data. *Sci Rep* (2019) 3949. doi:10.1038/s41598-019-40439-3
38. Giovannetti V, Lloyd S, and Maccone L. Quantum random access memory. *Phys Rev Lett* (2008) 100:160501. doi:10.1103/physrevlett.100.160501
39. Paetznick A, and Reichardt BW. Universal fault-tolerant quantum computation with only transversal gates and error correction. *Phys Rev Lett* (2013) 111:090505. doi:10.1103/PhysRevLett.111.090505
40. Anderson JT, Duclos-Cianci G, and Poulin D. Fault-tolerant conversion between the steane and reed-muller quantum codes. *Phys Rev Lett* (2014) 113:080501. doi:10.1103/PhysRevLett.113.080501
41. Jochym-O'Connor T, and Laflamme R. Using concatenated quantum codes for universal fault-tolerant quantum gates. *Phys Rev Lett* (2014) 112: 010505.
42. Paige C, and Wei M. History and generality of the CS decomposition. *Linear Algebra its Appl* (1994) 208-209:303–26. doi:10.1016/0024-3795(94)90446-4
43. Van Loan CF, and Golub G. *Matrix computations*. Baltimore): Johns Hopkins Press (1996).
44. Khaneja N, and Glaser SJ. Cartan decomposition of su(2n) and control of spin systems. *Chem Phys* (2001) 267:11. doi:10.1016/s0301-0104(01) 00318-4
45. Möttönen M, Vartiainen JJ, Bergholm V, and Salomaa MM. Quantum circuits for general multiqubit gates. *Phys Rev Lett* (2004) 93:130502. doi:10.1103/ physrevlett.93.130502
46. Vartiainen JJ, Möttönen M, and Salomaa MM. Efficient decomposition of quantum gates. *Phys Rev Lett* (2004) 92:177902. doi:10.1103/ physrevlett.92.177902
47. Press WH, Teukolsky SA, Flannery BP, and Vetterling WT. *Numerical recipes in fortran 77: volume 1, volume 1 of fortran numerical recipes: the art of scientific computing* (1992).
48. Moore C, and Nilsson M. Parallel quantum computation and quantum codes. *SIAM J Comput* (2001) 31:799. doi:10.1137/S0097539799355053
49. Patel KN, Markov IL, and Hayes JP. Optimal synthesis of linear reversible circuits. *Quan Inf. Comput.* (2008) 8:282. doi:10.26421/qic8.3-4-4
50. Jiang J, Sun X, Teng S-H, Wu B, Wu K, and Zhang J. *Optimal space-depth trade-off of cnot circuits in quantum logic synthesis* (2020). https://epubs.siam.org/doi/pdf/10.1137/1.9781611975994.13 (Accessed August 17, 2021).
51. Mohseni M, Rezakhani AT, and Lidar DA. Quantum-process tomography: Resource analysis of different strategies. *Phys Rev A* (2008) 77:032322. doi:10.1103/physreva.77.032322
52. Aaronson S. Read the fine print. *Nat Phys* (2015) 11:291. doi:10.1038/ nphys3272
53. Ekert AK, Alves CM, Oi DKL, Horodecki M, Horodecki P, and Kwek LC. Direct estimations of linear and nonlinear functionals of a quantum state. *Phys Rev Lett* (2002) 88:217901. doi:10.1103/physrevlett.88.217901
54. Clader BD, Jacobs BC, and Sprouse CR. Preconditioned quantum linear system algorithm. *Phys Rev Lett* (2013) 110:250504. doi:10.1103/physrevlett.110.250504
55. Cao Y, Papageorgiou A, Petras I, Traub J, and Kais S. Quantum algorithm and circuit design solving the poisson equation. *New J Phys* (2013) 15:013021. doi:10.1088/1367-2630/15/1/013021
56. Montanaro A, and Pallister S Quantum algorithms and the finite element, *method Phys Rev A*. 93 (2016). p. 032324. doi:10.1103/physreva.93.032324
57. Costa PC, Jordan S, and Ostrander A. Quantum algorithm for simulating the wave equation. *Phys Rev A* (2019) 99:012323. doi:10.1103/physreva.99.012323
58. Fillion-Gourdeau LEF. Simple digital quantum algorithm for symmetric first-order linear hyperbolic systems. *Numer Algor* (2019) 82. doi:10.1007/s11075-018-0639-3
59. Wang S, Wang Z, Li W, Fan L, Wei Z, and Gu Y. Quantum fast poisson solver: the algorithm and complete and modular circuit design. *Quan Inf Process* (2020) 19:1. doi:10.1007/s11128-020-02669-7
60. Leyton SK, and Osborne TJ. *A quantum algorithm to solve nonlinear differential equations* (2008). p. 4423. arXiv preprint arXiv:0812.
61. Childs AM, Kothari R, and Somma RD. Quantum algorithm for systems of linear equations with exponentially improved dependence on precision. *SIAM J Comput* (2017) 46:1920. doi:10.1137/16m1087072
62. Subaşı Y, Somma RD, and Orsucci D. Quantum algorithms for systems of linear equations inspired by adiabatic quantum computing. *Phys Rev Lett* (2019) 122:060504. doi:10.1103/PhysRevLett.122.060504
63. Altepeter JB, Branning D, Jeffrey E, Wei TC, Kwiat PG, Thew RT, et al. Ancilla-assisted quantum process tomography. *Phys Rev Lett* (2003) 90:193601. doi:10.1103/physrevlett.90.193601
64. Qi B, Hou Z, Li L, Dong D, Xiang G, and Guo G. Quantum state tomography via linear regression estimation. *Scientific Rep* (2013) 3:1. doi:10.1038/srep03496
65. Gross D, Liu Y-K, Flammia ST, Becker S, and Eisert J. Quantum state tomography via compressed sensing. *Phys Rev Lett* (2010) 105:150401. doi:10.1103/physrevlett.105.150401
66. Lloyd S, Mohseni M, and Rebentrost P. Quantum principal component analysis. *Nat Phys* (2014) 10:631. doi:10.1038/nphys3029
67. Cramer M, Plenio MB, Flammia ST, Somma R, Gross D, Bartlett SD, et al. Efficient quantum state tomography. *Nat Commun* (2010) 1:1. doi:10.1038/ ncomms1147
68. Tóth G, Wieczorek W, Gross D, Krischek R, Schwemmer C, and Weinfurter H. Permutationally invariant quantum tomography. *Phys Rev Lett* (2010) 105: 250403. doi:10.1103/physrevlett.105.250403
69. Schwemmer C, Tóth G, Niggebaum A, Moroder T, Gross D, Gühne O, et al. Experimental comparison of efficient tomography schemes for a six-qubit state. *Phys Rev Lett* (2014) 113:040503. doi:10.1103/PhysRevLett.113.040503
70. Aaronson S. The learnability of quantum states. *Proc R Soc A: Math Phys Eng Sci* (2007) 463:3089. doi:10.1098/rspa.2007.0113
71. Flammia ST, Gross D, Liu Y-K, and Eisert J. Quantum tomography via compressed sensing: error bounds, sample complexity and efficient estimators. *New J Phys* (2012) 14:095022. doi:10.1088/1367-2630/14/9/095022
72. Hartmann S. Generalized dicke states. *Quan Inf Comput* (2016) 16:1333. doi:10.26421/qic16.15-16-5
73. Kitagawa M, and Ueda M. Squeezed spin states. *Phys Rev A* (1993) 47:5138. doi:10.1103/physreva.47.5138
74. Suzuki Y, Uno S, Raymond R, Tanaka T, Onodera T, and Yamamoto N. Amplitude estimation without phase estimation. *Quan Inf Process* (2020) 19. doi:10.1007/s11128-019-2565-2
75. Huang H-Y, Kueng R, and Preskill J. Predicting many properties of a quantum system from very few measurements. *Nat Phys* (2020) 16:1050. doi:10.1038/ s41567-020-0932-7

Conflict of Interest: The authors declare that the research was conducted in the absence of any commercial or financial relationships that could be construed as a potential conflict of interest.

Publisher's Note: All claims expressed in this article are solely those of the authors and do not necessarily represent those of their affiliated organizations, or those of the publisher, the editors and the reviewers. Any product that may be evaluated in this article, or claim that may be made by its manufacturer, is not guaranteed or endorsed by the publisher.

6 Trapped ions as architecture for quantum computation

Trapped Ions as Architecture for Quantum Computation

Gabriel P. L. M. Fernandes,* Alexandre C. Ricardo, Fernando R. Cardoso, and Celso J. Villas-Boas
Universidade Federal de São Carlos, Departamento de Física, São Carlos, SP, Brasil

In this paper we describe one of the most promising platforms for the construction of a universal quantum computer, which consists of a chain of N ions trapped in a harmonic potential, whose internal states work out as qubits, and are coupled to collective vibrational modes of the chain. From such coupling, it is possible to build interactions between different ions of the chain, that is, qubit-qubit interactions that, together with individual operations on the ions, allow building a quantum computer as first proposed by Cirac and Zoller in the 1990s [Phys. Rev. Lett. **74**, 4091 (1995)]. Here we discuss from the physics involved in trapping ions in electromagnetic potentials to the Hamiltonian engineering needed to generate a universal set of logic gates, fundamental for the execution of more complex quantum algorithms. Finally, we present the current state of the art of quantum computing in trapped ion systems, highlighting recent advances made by companies and government projects that use such architecture, such as IonQ and AQTION.

Keywords: Quantum computation; Trapped ions; Quantum algorithms.

I. INTRODUCTION

The principle of superposition is at the origin of a series of attributes and properties of quantum states, which are essential in describing physical systems. Among its most notable consequences are the phenomena of coherence [1] and entanglement [2], both of which are fundamental to understanding the nature of non-classical properties and their applications to the development of new technologies, used, for example, in computing and information processing [3]. It has been shown that, based on these phenomena, machines operating under the laws of Quantum Mechanics can perform calculations more efficiently than those operating under the laws of Classical Mechanics [4], which enables a substantial gain in computing power when performing certain tasks [5]. The extent of the computational power of these new machines, known as quantum computers, depends on the task at hand and can translate into exponential gains in processing time [6] or even in solving problems that could not be solved in a timely manner by today's most powerful supercomputers [7].

In general, quantum computers are built in such a way that they can be programmed in one of the different possible models of quantum computing [8]. Specifically, considering the model of logic gates in discrete variables, a quantum computer is a network of systems whose dynamics are restricted to two levels. Individually, each system is called a *qubit*, the basic unit of quantum computing memory in which information is allocated and manipulated.

The *qubits* differ from classical bits in the following respect: while a bit has strictly deterministic behavior, given by a well-defined state, 0 or 1, the behavior of a *qubit* is probabilistic, and can present itself in the states $|0\rangle$ or $|1\rangle$, which form the computational basis of quantum computing, or in normalized superpositions of these [9]. In the computing model under consideration, the manipulation of the information allocated to the *qubits* is carried out via the application of quantum logic gates, which are interactions applied with the aim of rotating or entangling the states of the *qubits* [10]. The engineering behind these interactions and the mapping of the eigenstates onto the computational basis are issues that are inevitably linked to the nature of the systems that make up the quantum computer [11].

Over the last few decades, different physical systems have been considered for the implementation of quantum computing [11, 12]. Among those that have proved most appropriate, i.e. those in which a greater degree of control over the dynamics of the system has been achieved, are systems based on photonics [13], superconducting circuits [14] and trapped ions [15–17], each with its own particularities. In trapped ions, the first proposal for a scalable quantum computer was made by Cirac and Zoller [18], who idealized a system composed of a linear chain of N ions confined in a trap of approximately harmonic potential, in which the states of the qubits are manipulated via the application of laser pulses, which couple the internal states of the ions to the collective modes of motion of the chain [19, 20]. Currently, with financial investment from companies such as IonQ and AQT and government projects such as AQTION, architectures inspired by Cirac and Zoller's initial proposal have shown growing commercial success and new technological advances. In view of this, the aim of this article is to present in a didactic way the implementation of quantum computing in trapped ion systems, discussing some of the most fundamental results achieved to date.

This article is organized as follows: In Section II, we discuss the trapping of a single ion in a Paul trap, where we treat the classical equations of motion in order to derive the Hamiltonian of the motion of a single ion in a trap. In Section III, we consider two different schemes regarding the choice of the pair of states among the internal levels of the ions that will be mapped onto the $|0\rangle$ and $|1\rangle$ states, adopting the mathematically simpler model for the following sections. In Section IV, we consider a trapped ion interacting with a resonant or quasi-resonant laser pulse at only one atomic transition such that the dynamics of the ion is in fact restricted to a two-level system. We also discuss the engineering required to construct different interactions that allow the dynamics of the system to be controlled. In Section V, we consider the scalable (and therefore more interesting for quantum computing) system of a linear

* e-mail:gabrielpedro@df.ufscar.br

chain of N ions subjected to a harmonic potential, where the ions in the chain interact with each other via Coloumbian repulsion. In Section VI, we construct a set of elementary operations that can be applied to the ions in the chain such that any other unitary operations can be decomposed in terms of these, which is essential for implementing quantum algorithms. In Section VII, we demonstrate how the previously constructed interactions can be used to implement the quantum teleportation algorithm. In Section VIII, we discuss the current state of the art of quantum computers based on trapped ions. Finally, in Section IX, we present our conclusions.

II. ION TRAPS

Traps capable of confining ions in a region of space are essential for implementing quantum computing on trapped ion platforms. In this sense, the best-known ways of trapping ions are Penning traps and Paul traps, the result of independent work by physicists Hans Dehmelt [24, 25] and Wolfgang Paul [26], who shared the 1989 Nobel Prize in Physics for developing the trapping techniques used to this day [27]. Penning traps use electrostatic and magnetic fields for this purpose, while Paul traps use only electric fields - static and oscillating. Given its growing popularity in quantum computing, the confinement of ions in a Paul trap will be the subject of this section. Later on, we will address the problem of confining a linear chain of N ions in a trap, but for now we will devote our efforts to trapping a single ion. To do this, we will consider the partially time-dependent electric potential [28]

$$\Phi(\vec{x},t) = \frac{U}{2}\sum_{i=1}^{3}\alpha_i x_i^2 + \frac{\tilde{U}}{2}\cos(\omega_{\text{rf}}t)\sum_{i=1}^{3}\tilde{\alpha}_i x_i^2, \tag{1}$$

where $(x_1, x_2, x_3) = (x, y, z)$ denotes the Cartesian coordinates, U $\left(\tilde{U}\right)$ denotes the intensity of the time-independent (time-dependent) potential with the appropriate dimension and the constants α_i and $\tilde{\alpha}_i$ are the geometric parameters of the trap. We are assuming that the frequency of the oscillating field, ω_{rf}, is in the radio frequency range.

As discussed in basic electromagnetism courses, the electric potential must satisfy Laplace's equation,

$$\nabla^2\Phi(\vec{x},t) = 0, \tag{2}$$

which implies that the confinement of the ion in the trap is dynamic, since there is no point of global minimum in the potential, only saddle points. Furthermore, Laplace's equation generates restrictions on the values of the geometric parameters, i.e,

$$\begin{cases} \alpha_1 + \alpha_2 + \alpha_3 &= 0, \\ \tilde{\alpha}_1 + \tilde{\alpha}_2 + \tilde{\alpha}_3 &= 0, \end{cases} \tag{3}$$

It is therefore possible to build traps with different geometric configurations, depending on the choice of the parameters α_i and $\tilde{\alpha}_i$.

As the potential is separable in Cartesian coordinates, the treatment of the classical equations of motion comes down to determining the trajectory of the ion under the action of the force generated by the electric potential in one direction and generalizing the result for the others. Thus, for the axial direction, we have the ordinary differential equation

$$\frac{\mathrm{d}^2x}{\mathrm{d}t^2} = -\frac{Z|e|}{m}\left[U\alpha_x + \tilde{U}\tilde{\alpha}_x\cos(\omega_{\text{rf}})\right]x, \tag{4}$$

where Z is the degree of ionization of the atom (difference between the number of electrons and the number of protons), m is the mass of the ion and e is the electronic charge. Introducing the parameters

$$\xi = \frac{\omega_{\text{rf}}t}{2}, \quad a_x = \frac{4Z|e|U\alpha_x}{m\omega_{\text{rf}}^2}, \quad q_x = -\frac{2Z|e|\tilde{U}\tilde{\alpha}_x}{m\omega_{\text{rf}}^2}, \tag{5}$$

equation (4) can be written as

$$\frac{\mathrm{d}^2x}{\mathrm{d}\xi^2} + \left[a_x - 2q_x\cos(2\xi)\right]x = 0, \tag{6}$$

which is known as the Mathieu differential equation and has known solutions [30]. In the regime where $a_x, q_x^2 \ll 1$ [28], it can be shown that

$$x(t) \approx A\cos(\nu_x t)\left[1 - \frac{q_x}{2}\cos(\omega_{\text{rf}}t)\right], \tag{7}$$

where A is the amplitude of the oscilation of the ion in the trap and

$$\nu_x = \sqrt{a_x + \frac{q_x^2}{2}}\frac{\omega_{\text{rf}}}{2}. \tag{8}$$

The above expressions describe the motion of the ion in the axial direction: harmonic oscillations of frequency ν_x (secular motion or macromotion) superimposed by oscillations of smaller amplitude and higher frequency (micromotion). As Figure 1 shows, for sufficiently high frequencies of the oscillatory potential, in the radio frequency range, the micromotion can be neglected, bringing the trajectory of the ion in the trap closer to a harmonic motion in the axial direction, which justifies the decision to denote the frequency of the oscillatory potential as ω_{rf} from the start.

Thus, in the limit of high frequencies, the Hamiltonian of the ion's motion in one dimension is given by

$$H_m = \frac{p^2}{2m} + \frac{m}{2}\nu_x^2x^2, \tag{9}$$

isto é, a hamiltoniana do oscilador harmônico livre.

Quantitatively, still in the limit of high frequencies, it is possible to approximate the Hamiltonian of the ion's motion in one dimension to the Hamiltonian of a harmonic oscillator of frequency ν_x, by exchanging the coordinate x and the momentum p for the operators $\hat{x}$ and $\hat{p}$, which satisfy the commutation relation $[\hat{x},\hat{p}] = i\hbar$. To this end, the time dependence of the electric potential can be considered a disturbance whose effects, in the regime under consideration, will not significantly alter the eigenstates of the harmonic oscillator's Hamiltonian.

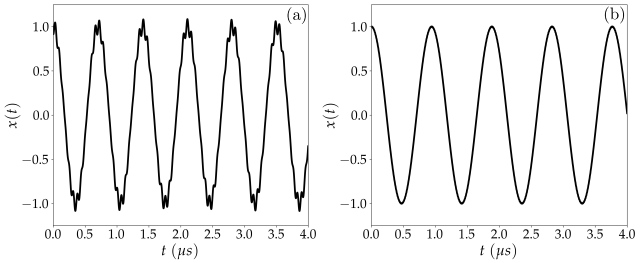

FIG. 1. Graph of the ion's position as a function of time for values of (a) $\omega_{\text{rf}} = 0.1$ GHz and (b) $\omega_{\text{rf}} = 0.5$ GHz, in the regime of equation (7), with $q_x = 0.17$, $\nu_x = 8.9$ MHz. It can be seen that for sufficiently large values of ω_{rf}, as occurs in (b), the ion's motion is close to a harmonic motion, so it is possible to disregard the micromotion term, represented by the visible deformation in relation to the harmonic motion in the peaks and valleys of (a), in the limit of high frequencies.

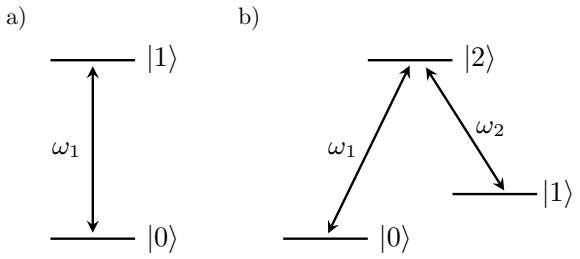

FIG. 2. Energy level diagrams for (a) two-level and (b) three-level systems. The states $|0\rangle$ and $|1\rangle$ in (a) have distinct parities. The states $|0\rangle$ e $|1\rangle$ in (b) have equal parities, and thus it is necessary to introduce an intermediate state, in general with a short lifetime for the dynamics between the states of the computational basis.

III. CHOICE OF INTERNAL LEVELS OF THE ION

In trapped ion architectures, the interactions that allow the information allocated to the qubits to be manipulated are constructed according to the theory of radiation-matter interaction [31, 32], by applying laser pulses with resonant or quasi-resonant frequencies to only one atomic transition of the ion, such that all other levels can be neglected, thus allowing the two internal states of the selected transition to be mapped onto the computational base, i.e. recognized as $|0\rangle$ and $|1\rangle$. The choice of which internal levels should be mapped onto the computational basis is made considering the parity of the wave functions of these states, which influence the engineering behind the interactions that are applied to the [33] system, as will be explained in the following sections.

There are two main schemes for choosing the internal [20] levels: In the first, which is conceptually simpler, the internal levels are chosen in such a way that the wave functions associated with the states have different parities. In the second, experimentally more complex, the internal levels have the same parity, but a third level of different parity must be used to mediate the interaction between the states of the computational base. The intermediate level, generally a state with a short lifetime, is used to bring the ion quickly to the initial desired level, which is chosen to be a state with a longer lifetime. A great deal of dissonance between the intermediate level and the fundamental levels means that it is not effectively populated, thus resulting in an effective interaction involving only the fundamental levels and, consequently, behaving in a manner equivalent to a two-level system. Thus, from now on, all discussion will consider ions as a two-level system, for simplicity. Both schemes are represented in Figure 2.

IV. HAMILTONIAN OF A SINGLE TRAPPED ION

The degree of success in implementing quantum computing in real physical systems depends on the control that can be obtained over the dynamics of the system. Each physical system has its own methods from which it is possible to generate interactions that make it possible to control its dynamics. In trapped ion platforms, control of the states that describe the system is achieved by applying laser pulses at specific frequencies. For a more in-depth discussion, this section aims to derive the Hamiltonian of a single ion trapped in a Paul trap interacting with a laser pulse and, from this Hamiltonian, to construct the elementary interactions that allow the dynamics of the system to be controlled.

The Hamiltonian to be derived is given by

$$\hat{H} = \hat{H}_m + \hat{H}_a + \hat{V}_I, \tag{10}$$

where $\hat{H}_m$ is the Hamiltonian of the motion of the ion trapped in the trap, $\hat{H}_a$ is the Hamiltonian of the ionized atom and $\hat{V}_I$ is the interaction potential between the ion and the applied beam. In the following subsections, we will deduce expressions for these Hamiltonians, quantizing different aspects of the system.

A. Quantization of the Motion

As discussed, the axial motion of the ion in the trap is approximately described by the Hamiltonian of the one-dimensional harmonic oscillator, and the result can be generalized to the other dimensions. In this way, we can describe the ion's motion quantumly by exchanging the coordinate and momentum variables for the respective operators $\hat{x}$ and $\hat{p}$ of a harmonic oscillator. For convenience, we also define the operators

$$\hat{a}_x = \sqrt{\frac{m\nu_x}{2\hbar}}\left(\hat{x} + \frac{i}{m\nu_x}\hat{p}\right), \tag{11a}$$

$$\hat{a}_x^\dagger = \sqrt{\frac{m\nu_x}{2\hbar}}\left(\hat{x} - \frac{i}{m\nu_x}\hat{p}\right), \tag{11b}$$

respectively called the annihilation and creation operators of the (axial) vibrational mode. In order not to overload the notation, the subscript for the secular frequency and the mode

creation and annihilation operators will be omitted from here on, it being clear that at all times we are referring to the operators and secular frequency of the axial mode. From the commutation relation between $\hat{x}$ and $\hat{p}$, it can be shown that $\left[\hat{a}, \hat{a}^\dagger\right] = 1$.

Inverting equations (11a) and (11b), it can be shown that

$$\hat{x} = \sqrt{\frac{\hbar}{2m\nu}}\left(\hat{a}^\dagger + \hat{a}\right), \tag{12a}$$

$$\hat{p} = i\sqrt{\frac{\hbar m\nu}{2}}\left(\hat{a}^\dagger - \hat{a}\right), \tag{12b}$$

such that, substituting in the quantized version of the equation (9), we get

$$\hat{H}_m = \hbar\nu\left(\hat{a}^\dagger\hat{a} + \frac{1}{2}\right), \tag{13}$$

i.e. the Hamiltonian of the ion's motion in terms of the creation and annihilation operators, whose physical meanings will be discussed below.

The definitions of $\hat{a}$ and $\hat{a}^\dagger$ show the non-hermiticity of these operators, but the product $\hat{a}^\dagger\hat{a}$ is hermitian and it is useful to define the vibrational mode number operator,

$$\hat{N} = \hat{a}^\dagger\hat{a}, \tag{14}$$

whose eigenvalues and eigenvectors equation is given by

$$\hat{N}\left|n\right\rangle = n\left|n\right\rangle, \tag{15}$$

where n assumes only non-negative integers [34]. Since $\left[\hat{H}_m, \hat{N}\right] = 0$, $\hat{H}_m$ and $\hat{N}$ share a common basis of eigenstates [35]. In this way, the set of eigenstates of the number operator also forms the basis of eigenvectors of the Hamiltonian of the ion's motion, and are called Fock states or mode number states.

The actions of the operators $\hat{a}$ and $\hat{a}^\dagger$ on the Fock states are - as expected from the treatment of the quantum harmonic oscillator - given by

$$\hat{a}\left|n\right\rangle = \sqrt{n}\left|n-1\right\rangle, \tag{16a}$$

$$\hat{a}^\dagger\left|n\right\rangle = \sqrt{n+1}\left|n+1\right\rangle, \tag{16b}$$

in such a way that applying the creation (annihilation) operator to the number state $\left|n\right\rangle$ generates a number state increased (decreased) by one, creating (annihilating) an excitation in the vibrational mode, i.e. a phonon. The number states therefore determine the number of phonons in the mode.

Finally, by relocating the energy zero in the equation (13), we obtain

$$\hat{H}_m = \hbar\nu\hat{a}^\dagger\hat{a} \tag{17}$$

as the Hamiltonian of the ion's motion in a harmonic trap. The result can be generalized to other dimensions when necessary.

B. Matter Quantization

Assuming that the laser pulse applied is resonant or quasi-resonant with only one atomic transition, it is possible to consider the states of the ion as restricted to two energy levels, disregarding interaction with all other levels, which is certainly fundamental for mapping the internal states in the computational base. Thus consider the states $\left|g\right\rangle$ and $\left|e\right\rangle$, which represent the states of the computational basis defined previously $\left|0\right\rangle$ and $\left|1\right\rangle$ [†], with energy E_g and E_e, respectively. Thus, the Hamiltonian of the atom in the eigenstate basis is given by

$$\hat{H}_a = \hat{\mathbb{I}}\hat{H}_a\hat{\mathbb{I}} = E_g\left|g\right\rangle\!\left\langle g\right| + E_e\left|e\right\rangle\!\left\langle e\right|, \tag{18}$$

where $\hat{\mathbb{I}}$ is the identity operator, such that, from the matrix representation of the states,

$$\left|g\right\rangle = \begin{pmatrix}0\\1\end{pmatrix}, \qquad \left|e\right\rangle = \begin{pmatrix}1\\0\end{pmatrix}, \tag{19}$$

we obtain the matrix form of $\hat{H}_a$,

$$\hat{H}_a = \begin{pmatrix}E_e & 0\\0 & E_g\end{pmatrix}, \tag{20}$$

which can be written as

$$\hat{H}_a = \frac{1}{2}(E_g + E_e)\hat{\mathbb{I}} + \frac{1}{2}(E_e - E_g)\hat{\sigma}_z. \tag{21}$$

where $\hat{\sigma}_z$ is one of the Pauli matrices introduced in Appendix A.

Defining $\omega_0 = \omega_e - \omega_g$ as the transition frequency between the ground state and the excited state of the atom and conveniently relocating the energy zero of the Hamiltonian, we obtain

$$\hat{H}_a = \frac{\hbar\omega_0}{2}\hat{\sigma}_z, \tag{22}$$

as the Hamiltonian of the ionized atom.

C. Quantization of the Interaction Between Internal and External Degrees of Freedom

By restricting the laser wavelength to values much larger than the dimensions of the ion, the coupling with the electric field generates an induced electric dipole, whose interaction potential with the field is given by [36]

$$\hat{V}_I = -\hat{\boldsymbol{d}}\cdot\mathbf{E}, \tag{23}$$

[†] In Quantum Mechanics texts, the notation $\left|g\right\rangle$ and $\left|e\right\rangle$ is widely used. In Quantum Computing texts, on the other hand, in an analog of Classical Computing, the notation $\left|0\right\rangle$ and $\left|1\right\rangle$ is the usual notation. Here, we will use both notations, depending on the context, and the states can be directly mapped, i.e. $\left|g\right\rangle \longleftrightarrow \left|0\right\rangle$ and $\left|e\right\rangle \longleftrightarrow \left|1\right\rangle$.

where $\hat{\boldsymbol{d}}$ is the electric dipole operator and $\mathbf{E}$ the electric field of the laser on the dipole. In the eigenstate basis, the electric dipole operator is given by

$$\hat{\boldsymbol{d}} = \sum_{i,j=g,e} \boldsymbol{d}_{ij} \left|i\right\rangle\!\left\langle j\right|, \tag{24}$$

where the elements

$$\boldsymbol{d}_{ij} = \langle i|\hat{\boldsymbol{d}}|j\rangle = -|e| \int \psi_i^*(\mathbf{r})\ \mathbf{r}\ \psi_j(\mathbf{r})\ \mathrm{d}^3r, \tag{25}$$

are commonly called dipole transitions, since they are associated with transitions from the $|j\rangle$ state to the $|i\rangle$ state, which can be allowed (non-zero) or forbidden (equal to zero) depending on the parity of the $\psi_i(\mathbf{r})$ and $\psi_j(\mathbf{r}$ wave functions, as shown in equation (25).

Assuming that the wave functions of the electronic states are distinct parity functions, we obtain

$$\hat{V}_I = -\left(\boldsymbol{d}_{ge}\hat{\sigma}_- + \boldsymbol{d}_{eg}\hat{\sigma}_+\right)\cdot\mathbf{E}, \tag{26}$$

where $\hat{\sigma}_- = |g\rangle\!\langle e|$ and $\hat{\sigma}_+ = |e\rangle\!\langle g|$, as discussed in Appendix A. For propagating electric fields, we can approximate them by plane waves and therefore we can write

$$\hat{V}_I = -\left(\boldsymbol{d}_{ge}\hat{\sigma}_+ + \boldsymbol{d}_{eg}\hat{\sigma}_-\right)\cdot\mathbf{E_0}\left(e^{i(\mathbf{k}\cdot\hat{\mathbf{r}}-\omega t+\phi)} + h.c.\right), \tag{27}$$

where $\mathbf{E_0}$ is the vector amplitude of the field, $\mathbf{k}$ is its wave vector, ω is its oscillation frequency and ϕ is the phase of the wave. $h.c.$ represents the conjugate Hermitian.

Assuming that the matrix element $\boldsymbol{d}_{ge}$ is real [‡], we can define the atom-field coupling constant,

$$\frac{\Omega}{2} = \left|\frac{e}{\hbar}\left\langle g\right|\hat{\mathbf{r}}\left|e\right\rangle\cdot\mathbf{E_0}\right|, \tag{28}$$

which describes the coupling strength between the atomic transition (between electronic levels) and the field. Thus, in terms of the coupling constant, we can write

$$\hat{V}_I = \frac{\hbar\Omega}{2}\left(\hat{\sigma}_+ + \hat{\sigma}_-\right)\left(e^{i(\mathbf{k}\cdot\hat{\mathbf{r}}-\omega t+\phi)} + h.c\right) \tag{29}$$

as the atom-field interaction potential.

D. Jaynes-Cummings Hamiltonian

The above results lead to the total Hamiltonian of the system in the Schrödinger picture,

$$\hat{H} = \hbar\nu\hat{a}^\dagger\hat{a} + \frac{\hbar\omega_0}{2}\hat{\sigma}_z + \frac{\hbar\Omega}{2}\left(\hat{\sigma}_+ + \hat{\sigma}_-\right)\left(e^{i(\mathbf{k}\cdot\hat{\mathbf{r}}-\omega t+\phi)} + h.c.\right).$$

[‡] According to D. Wineland *et al.* [28], it is always possible to choose a convention in which the element of the electric dipole matrix is real. This is possible because the general phase (which governs the evolution of the system) is composed of the sum of the phase coming from the wave functions and the phase of the external field (which is perfectly controllable). An alternative treatment is that in [37].

Rabi Hamiltonian, as the equation above is known, has sophisticated analytical solutions [38, 39]. However, it is possible to find simpler solutions to an approximate problem. This approximation consists of analyzing the time evolution of Rabi Hamiltonian and discarding the terms that oscillate more rapidly. The idea is that, on average, the terms that oscillate more slowly dominate the dynamics of the system. To follow the procedure, however, it is necessary to rewrite the Rabi Hamiltonian in the interaction picture.

The interaction picture is an intermediate picture between the Schrödinger and Heisenberg pictures. In the interaction picture, both the states of the system and the linear operators acting on these states have time dependence. The interaction picture can be used whenever the Hamiltonian of the system can be written as the sum of two terms

$$\hat{H} = \hat{H}_0 + \hat{H}_1, \tag{30}$$

where, typically, the separation of terms is done in such a way that the simplest terms of the total Hamiltonian - those whose dynamics are known - are included in $\hat{H}_0$ while the more complicated terms - whose dynamics are still unknown - are included in $\hat{H}_1$. In general, the terms in the last Hamiltonian describe the interaction between two systems whose Hamiltonians are included in $\hat{H}_0$, known as the free part of the system.

The states in the Schrödinger picture are connected to the states in the interaction picture via the transformation,

$$\left|\psi(t)\right\rangle_I = \hat{U}_0^\dagger(t)\left|\psi(t)\right\rangle_S = e^{i\hat{H}_0 t/\hbar}\left|\psi(t)\right\rangle_S, \tag{31}$$

while the connection between the operators of the different pictures is given by

$$\hat{A}_I(t) = e^{i\hat{H}_0 t/\hbar}\hat{A}_S e^{-i\hat{H}_0 t/\hbar}, \tag{32}$$

where the elements of the Schrödinger picture (Interaction) are represented by the subscript S (I).

By relating the elements of both descriptions, we can derive the equation that describes the evolution of states in the interaction picture. In fact, with a few algebraic manipulations, inverting the equation (31) and substituting it into the Schrödinger equation, we obtain

$$\left(\hat{U}_0\hat{H}\hat{U}_0 - \hat{H}_0\right)\left|\psi(t)\right\rangle_I = i\hbar\frac{\partial\left|\psi(t)\right\rangle_I}{\partial t}, \tag{33}$$

which, taking into account the evolution of operators in the interaction picture, equation (32), can be written as

$$\hat{H}_1(t)\left|\psi(t)\right\rangle_I = i\hbar\frac{\partial\left|\psi(t)\right\rangle_I}{\partial t}, \tag{34}$$

which is the analog of the Schrödinger equation in the interaction picture since the Hamiltonian $\hat{H} = \hat{H}_0 + \hat{H}_1$ is represented by

$$\hat{H} = \hat{U}_0^\dagger\hat{H}_1\hat{U}_0 \tag{35}$$

in the interaction picture.

Thus, from equation (35), with $\hat{H}_0 = \hat{H}_a + \hat{H}_m$ and $\hat{H}_1 = \hat{V}_I$, Rabi Hamiltonian in the interaction picture is given by

$$\hat{H} = \frac{\hbar\Omega}{2}[\hat{\sigma}_+(t) + \hat{\sigma}_-(t)]\left\{e^{i\left[\eta[\hat{a}(t)+\hat{a}^\dagger(t)]-\omega t+\phi\right]} + h.c.\right\}, \tag{36}$$

where $\eta = k\cos\theta\sqrt{\hbar/2m\nu}$ is called the Lamb-Dicke parameter, and θ is the angle between the direction of the laser and the direction of motion of the ion in the trap. The evolution of the operators present in Rabi Hamiltonian is given by

$$\hat{a}^\dagger(t) = \hat{a}^\dagger e^{i\nu t}, \qquad \hat{a}(t) = \hat{a}e^{-i\nu t}, \tag{37}$$

$$\hat{\sigma}_+(t) = \hat{\sigma}_+ e^{i\omega_0 t}, \qquad \hat{\sigma}_-(t) = \hat{\sigma}_- e^{-i\omega_0 t}, \tag{38}$$

as can be shown by the Baker-Campbell-Haussdorff lemma [40] from the equation (32).

Introducing the operator $\hat{\gamma} = \eta\left(\hat{a}e^{-i\nu t} + \hat{a}^\dagger e^{i\nu t}\right)$ just to simplify the notation, we can write

$$\hat{H} = \frac{\hbar\Omega}{2}\left(\hat{\sigma}_+ e^{-i\delta t}e^{i(\hat{\gamma}+\phi)} + \hat{\sigma}_- e^{i\bar{\omega}t}e^{i(\hat{\gamma}+\phi)} + h.c.\right), \tag{39}$$

where we define $\delta \equiv \omega - \omega_0$ and $\bar{\omega} \equiv \omega + \omega_0$. In the rotating wave approximation, the fastest oscillating terms - the exponentials with frequency $\bar{\omega}$ - can be discarded, which allows us to write

$$\hat{H}_{JC} = \frac{\hbar\Omega}{2}\left(\hat{\sigma}_+ e^{-i\delta t}e^{i(\hat{\gamma}+\phi)} + h.c.\right), \tag{40}$$

which is known as the semiclassical Jaynes-Cummings Hamiltonian.

E. Elementary Interactions

In the development of the semiclassical Jaynes-Cummings Hamiltonian, the Lamb-Dicke parameter, $\eta = k\cos\theta\sqrt{\hbar/2m\nu}$, was introduced. This parameter quantifies the amplitude of the oscillations of the ion in the trap when compared to the wavelength of the applied radiation [28]. A very useful regime is the Lamb-Dicke regime, in which $\eta \ll 1$, i.e. the oscillation amplitude is very small compared to the wavelength of the applied laser. Under these conditions, expanding the exponential to first order and disregarding higher order terms, we have

$$\hat{H}_{LD} = \frac{\hbar\Omega}{2}\left\{\hat{\sigma}_+\left[1 + i\eta\left(\hat{a}e^{-i\nu t} + \hat{a}^\dagger e^{i\nu t}\right)\right]e^{i(\phi-\delta t)} + h.c.\right\},$$

which allows us to study the possible interactions that can be built up by changing the frequency of the applied laser pulse, coupling the internal levels to the external (vibration) levels. The nature of the operators generates different transition frequencies for each possible interaction between ion and light, which are generally referred to as Rabi frequencies [41].

For $\delta = 0$, in which case the frequency of the applied laser is resonant with the transition frequency between the internal levels, we have

$$\hat{H} = \frac{\hbar\Omega}{2}\left(\hat{\sigma}_+ e^{i\phi} + \hat{\sigma}_- e^{-i\phi}\right), \tag{41}$$

where the spin-wave approximation was applied, in this case because we assumed $\nu \gg \eta\Omega$, thus allowing us to disregard the terms proportional to the time exponentials in $\hat{H}_{LD}$. The interaction with the resonant field induces transitions of the type $|g,n\rangle \longleftrightarrow |e,n\rangle$ with Rabi frequency Ω, changing the internal state without modifying the vibrational state of the mode. This interaction is called resonant field interaction (*carrier interaction*).

For $\delta = -\nu$, the case in which the frequency of the applied laser is given by $\omega = \omega_0 - \nu$, we have

$$\hat{H} = \frac{\hbar\Omega}{2}\eta\left(\hat{a}\hat{\sigma}_+ e^{i\phi} + \hat{a}^\dagger\hat{\sigma}_- e^{-i\phi}\right), \tag{42}$$

where the spin-wave approximation was applied (assuming then $\nu \gg \Omega$). The interaction induces transitions of the type $|g,n\rangle \longleftrightarrow |e,n-1\rangle$ with Rabi frequency $\Omega_{n,n-1} = \Omega\eta\sqrt{n}$. This Hamiltonian is known as the first red shift (*first red sideband interaction*) and produces interactions in which the internal state is excited at the cost of annihilating a phonon in the ion's vibrational mode, or the internal state is de-excited at the cost of creating a phonon in the ion's vibrational mode.

For $\delta = \nu$, then $\omega = \omega_0 + \nu$, and therefore,

$$\hat{H} = \frac{\hbar\Omega}{2}\eta\left(\hat{a}^\dagger\hat{\sigma}_+ e^{i\phi} + \hat{a}\hat{\sigma}_- e^{-i\phi}\right), \tag{43}$$

where the rotating wave approximation has been applied (again assuming $\nu \gg \Omega$) . The interaction induces transitions of the type $|g,n\rangle \longleftrightarrow |e,n+1\rangle$ with Rabi frequency $\Omega_{n,n+1} = \Omega\eta\sqrt{n+1}$. This Hamiltonian is known as the first blue shift (*first blue sideband interaction*) and produces interactions in which both the internal and external states of the ion undergo excitations or de-excitations.

The interactions constructed above – namely, resonant field interaction, first red shift and first blue shift – can be used to apply logic gates (in this case, rotations) on the internal states of a single trapped ion by means of the $\hat{\sigma}_+$ and $\hat{\sigma}_-$ matrices, as well as their possible combinations. The engineering of interactions behind logic gates will be discussed in Section VI, after studying the interactions that can be generated in a linear chain of N ions, i.e. a system of trapped ions that is scalable and more suitable for implementing quantum computing.

V. HAMILTONIAN OF SEVERAL TRAPPED IONS

Processing information and solving complex problems quickly and efficiently is one of the great challenges of quantum computing. An important (but not unique) aspect of a quantum computer's ability to solve problems is the number of qubits available for implementing [3] algorithms. In general, problems of technological and industrial interest require a high number of qubits, especially when error correction protocols are considered [42]. There is therefore a concern to develop quantum computers that are scalable, i.e. that can support a progressively larger number of qubits. On trapped ion platforms, one of the ways to develop scalable quantum computers is to gain control of the dynamics of a chain of

N ions, where each ion represents a qubit on which information can be allocated and processed. In this section, we will discuss the dynamics of a linear chain of N ions and the possible interactions that can be generated in such a system, which in a way represents an essential step towards characterizing trapped ion systems as a viable architecture for implementing quantum computing.

To do this, we will consider a chain of ions trapped in a Paul trap in which the motion of the ions is harmonic in the axial direction and strongly limited (to the point of being negligible) in the other directions. In a configuration like this, Coloumbian repulsion between the ions plays an important role, since the motion of each ion in the chain influences the motion of the others, as in a coupled oscillator problem. In this way, describing the individual motion of N coupled ions in terms of ordinary coordinates can become an extremely complex task. It is always possible, however, to describe the overall motion of the system as a combination of simpler collective and oscillatory motions, which are called [43] normal modes.

The normal modes of the system – a set of collective oscillatory motions whose combinations are useful for describing the overall motion of the system – are constructed in such a way that they are independent (or uncoupled) from each other, even though there is a physical coupling between the ions in the chain. Identifying each of the normal modes makes it possible to build up a revealing picture of the dynamics of the system, even though the actual motion is a sometimes complicated combination of all the independent periodic motions [44]. For this reason, the classical treatment of the equations of motion of a linear chain of N ions boils down to finding the normal modes of our system. Subsequently, we will quantize the normal modes in a similar way to what we did when we quantized the vibrational modes of a single trapped ion in the last section. For most of this section, we will follow the mathematical treatment carried out in the references [18, 20], considering at various times the simplest example of a chain of two ions, a problem that is intuitive and even possibly familiar to the reader.

In a system like the one described above, it is important to understand how the motion of each ion in the chain – subjected to a harmonic potential – is influenced by the Coloumbian repulsion generated by the other $(N-1)$ ions. To do this, assume that the displacement of the mth ion, listed from left to right, can be approximated by

$$x_m(t) \approx x_m^{(0)} + q_m(t), \tag{44}$$

where $x_m^{(0)}$ denotes the equilibrium position of the m-th ion and $q_m(t)$ denotes small displacements around the equilibrium position.

Under this notation, the potential energy of the system is written as

$$V = \sum_{m=1}^{N} \frac{1}{2} M\nu^2 x_m(t)^2 + \sum_{m,n=1\ m\neq n}^{N} \frac{Z^2e^2}{8\pi\epsilon_0} \frac{1}{|x_m(t) - x_n(t)|}, \tag{45}$$

where M is the mass of each ion, e is the electronic charge, Z is the degree of ionization of the atoms in the chain, ϵ_0 is the electrical permittivity of the vacuum and ν is the secular frequency in the axial direction. The kinetic energy is simply the sum of the kinetic energies of each of the ions in the chain.

Thus, the equilibrium position of the m-th ion in the chain is given by

$$\left[\frac{\partial V}{\partial x_m}\right]_{x_m = x_m^{(0)}} = 0, \tag{46}$$

and defining the parameter

$$\ell = \left(\frac{1}{4\pi\epsilon_0}\frac{Z^2e^2}{M\nu^2}\right)^{1/3}, \tag{47}$$

which has unit position, we can introduce a dimensionless variable for the equilibrium position of the m-th ion, i.e,

$$u_m = x_m^{(0)}/\ell. \tag{48}$$

Rewriting the equation (46) in terms of the dimensionless equilibrium positions, we have a linear system of N coupled equations for each $n = 1, ..., N$,

$$u_m - \sum_{m=1}^{n-1} \frac{1}{(u_m - u_n)^2} + \sum_{m=n+1}^{N} \frac{1}{(u_m - u_n)^2} = 0, \tag{49}$$

that can be solved for arbitrary N. For $N = 2$, for example,

$$x_1^{(0)} = -\frac{1}{2^{2/3}}\ell, \qquad x_2^{(0)} = \frac{1}{2^{2/3}}\ell.$$

More than knowing the equilibrium position, we want to describe the collective motion of the ion chain from the Hamiltonian of the system. To do this, based on the kinetic and potential energies, we can write the Lagrangian of the system as

$$L = \frac{M}{2}\sum_{m=1}^{N}\dot{q}_m^2 - \frac{1}{2}\sum_{m,n=1}^{N} q_m q_n \left[\frac{\partial^2 V}{\partial x_m \partial x_n}\right]_{q_m = q_n = 0}, \tag{50}$$

where the potential energy has been expanded in Taylor series around the equilibrium points, readjusting the zero energy and disregarding higher order terms.

It can be verified that

$$L = \frac{M}{2}\left[\sum_{m=1}^{N}\dot{q}_m^2 - \nu^2 \sum_{m,n=1} A_{mn} q_m q_n\right], \tag{51}$$

where the elements of the matrix A_{mn} are given by

$$A_{mn} = \begin{cases} 1 + 2\sum\limits_{\substack{p=1 \\ p\neq m}}^{N} \dfrac{1}{|u_m - u_p|^3}, m = n, \\ \dfrac{-2}{|u_m - u_n|^3}, m \neq n, \end{cases} \tag{52}$$

it is easy to see that, as well as having real elements, the matrix A is symmetric because the order of derivation is arbitrary.

The problem now comes down to finding a coordinate transformation that diagonalizes the matrix A, making the problem simpler [44]. These coordinates are found from the eigenvalues and eigenvectors equation,

$$\sum_{n=1}^{N} A_{mn}\boldsymbol{b}_n^{(p)} = \mu_p \boldsymbol{b}_m^{(p)} \quad (p = 1, ..., N), \tag{53}$$

with $\mu_p \geq 0$. The eigenvectors are enumerated by the index p (from the smallest to the largest corresponding eigenvalue) and normalized so that the completeness and orthonormality relations hold,

$$\sum_{p=1}^{N} \boldsymbol{b}_m^{(p)}\boldsymbol{b}_n^{(p)} = \delta_{mn}, \tag{54a}$$

$$\sum_{m=1}^{N} \boldsymbol{b}_m^{(p)}\boldsymbol{b}_m^{(q)} = \delta_{pq}. \tag{54b}$$

It can be shown that the first and second eigenvalues and eigenvectors are always given by

$$\boldsymbol{b}^{(1)} = \frac{1}{\sqrt{N}}\begin{pmatrix}1\\1\\\vdots\\1\end{pmatrix}, \quad \mu_1 = 1, \tag{55a}$$

$$\boldsymbol{b}^{(2)} = \frac{1}{\sqrt{\sum_{m=1}^{N} u_m^2}}\begin{pmatrix}u_1\\u_2\\\vdots\\u_N\end{pmatrix}, \quad \mu_2 = 3, \tag{55b}$$

where the constants u_m are determined by the equation (49). As an illustration, for $N = 2$, the eigenvectors of the matrix A are

$$\boldsymbol{b}^{(1)} = \frac{1}{\sqrt{2}}\begin{pmatrix}1\\1\end{pmatrix}, \quad \mu_1 = 1,$$

$$\boldsymbol{b}^{(2)} = \frac{1}{\sqrt{2}}\begin{pmatrix}-1\\1\end{pmatrix}, \quad \mu_2 = 3.$$

The normal modes of the system are defined by [44]

$$Q_p(t) = \sum_{m=1}^{N} \boldsymbol{b}_m^{(p)} q_m(t). \tag{57}$$

The first of these modes, $Q_1(t)$, called the center of mass mode, corresponds to a motion in which all the ions oscillate back and forth as if they were rigidly attached to each other. The second mode, $Q_2(t)$, called breathing mode, corresponds to a motion in which each ion oscillates with an amplitude proportional to its distance from the center of the trap [45].

Inverting the equation (57), we get

$$q_m(t) = \sum_{p=1}^{N} \boldsymbol{b}_m^{(p)} Q_p(t), \tag{58}$$

that allows us to rewrite the lagrangean of the system, equation (51), in terms of the normal modes,

$$L = \frac{M}{2}\sum_{p=1}^{N}\left[\dot{Q}_p^2 - \nu_p^2 Q_p^2\right], \tag{59}$$

where $\nu_p = \sqrt{\mu_p}\nu$ is the frequency of the p-th mode. As discussed earlier, the advantage of finding the normal modes that describe the system is that they allow the motion of the system to be studied as a combination of independent oscillatory motions with well-defined frequencies, as can be seen in the equation above, from which the Hamiltonian of the system can be derived.

In terms of normal modes, the Hamiltonian of the linear chain of N ions is, considering the canonically conjugate moment $P_p = M\dot{Q}_p$, given by

$$H = \sum_{p=1}^{N}\left[\frac{P_p^2}{2M} + \frac{1}{2}M\nu_p^2 Q_p^2\right]. \tag{60}$$

Similarly to what was done in the study of the dynamics of a single trapped ion, we can introduce the position and momentum operators of the p-th normal mode as a linear combination of the creation and annihilation operators of the respective normal mode,

$$\hat{Q}_p(t) = \sqrt{\frac{\hbar}{2M\omega}}\left(\hat{a}_p^\dagger e^{i\nu_p t} + \hat{a}_p e^{-i\nu_p t}\right), \tag{61a}$$

$$\hat{P}_p(t) = i\sqrt{\frac{\hbar M\omega}{2}}\left(\hat{a}_p^\dagger e^{i\nu_p t} - \hat{a}_p e^{-i\nu_p t}\right), \tag{61b}$$

already written in the interaction picture and defined in the same way as before, i.e. such that $\left[\hat{Q}_p, \hat{P}_p\right] = i\hbar$ and $\left[\hat{a}_p, \hat{a}_p^\dagger\right] = 1$.

From equation (58), it is possible to define the operator $\hat{q}_m(t)$, which denotes the displacement of the m-th ion around its equilibrium position, in terms of the creation and annihilation operators of the normal modes,

$$\hat{q}_m(t) = \sum_{p} s_m^{(p)}\left(\hat{a}_p^\dagger e^{i\nu_p t} + \hat{a}_p e^{-i\nu_p t}\right), \tag{62}$$

where we define

$$s_m^{(p)} = \frac{\sqrt{N}\boldsymbol{b}_m^{(p)}}{\mu_p^{1/4}} \tag{63}$$

as the mode coupling constant. Thus, for the center of mass mode,

$$s_m^{(1)} = 1, \qquad \nu_1 = \nu,$$

and for the breathing mode,

$$s_m^{(2)} = \frac{\sqrt{N}}{3^{1/4}} \frac{u_m}{(\sum_m^N u_m^2)^{\frac{1}{2}}}, \quad \nu_2 = \sqrt{3}\nu. \tag{64}$$

The equation (62) expresses an important result of the section. In short, we have shown that it is possible to have an organized structure of ions whose equilibrium positions are determined by the coulombic repulsion and the harmonic potential to which the ions are subjected. In this system, however, Coulombian repulsion does not allow us to study the motion of each ion separately, since the motion of one ion is coupled to that of all the others by the interaction between the electric charges. On the other hand, it is possible to describe the displacement of a single ion from the superposition of the creation and annihilation operators of the collective vibrational modes. Having defined the creation and annihilation operators for each mode, the next step is to analyze the interaction between a single laser and the chain of trapped ions, connecting what we have seen so far with the aim of applying logic gates to a scalable platform of trapped ions whose internal states are mapped onto the computational basis of the qubits of a quantum computer.

A. Elementary Interactions

Similar to the case of a single trapped ion, the interaction potential between a laser pulse and the m-th ion of the linear chain is described by the dipole interaction,

$$\hat{V}_I = -\hat{\boldsymbol{d}} \cdot \mathbf{E}, \tag{65}$$

where $\hat{\boldsymbol{d}}$ is the dipole moment of the m-th ion and $\mathbf{E}$ is the electric field in the dipole. Still following the reference [20], now considering, for convenience, a stationary field (where we replace the exponential function that appeared earlier with a sinusoidal function) and carrying out the same procedure for coupling the potential with the electronic states discussed in the previous section, we obtain

$$\hat{H} = \frac{\hbar\Omega}{2} \sin\left[k\hat{\zeta}_m(t)\right] e^{i(\delta t - \phi)} \hat{\sigma}_- + h.c., \tag{66}$$

i.e. the Hamiltonian describing the interaction between the stationary field and the m-th ion of the chain in the interaction picture, the spin-wave approximation having been applied. As before, δ is the dissonance between the frequencies, Ω_0 is the coupling constant of the field with the m-th ion, k is the wave number and ϕ is the phase of the field. The new operator introduced, $\hat{\zeta}_m(t)$, denotes the distance between the mth ion and the plane mirror used to form the stationary wave, as shown in Figure 3.

Adjusting the ion-mirror distance such that the equilibrium position of the m-th ion is at a node of the field,

$$\hat{\zeta}_m(t) = \frac{l\lambda}{2} + \hat{q}_m(t)\cos\theta, \tag{67}$$

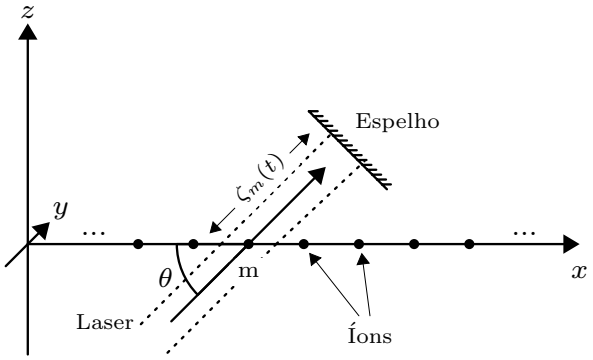

FIG. 3. Schematic representation of the linear ion chain proposed by Cirac and Zoller in a Cartesian coordinate system. The laser beam is applied parallel to the y direction. Adapted from [20].

where l is an integer, λ is the laser wavelength and θ is the angle between the direction of the applied beam and the trap axis. Therefore, the interaction generated is of the form

$$\hat{H} = \frac{\hbar\Omega}{2} \sin\left[k\hat{q}_m(t)\cos\theta\right] e^{i(\delta t - \phi + l\pi)} \hat{\sigma}_- + h.c.. \tag{68}$$

Thus, as we consider the displacement of the m-th ion around the equilibrium point to be sufficiently small, it is possible to disregard the higher orders of the operator $\hat{q}_m(t)$ in the expansion of $\sin\left[k\hat{q}_m(t)\cos\theta\right]$, obtaining the interaction

$$\hat{H} \approx \frac{\hbar\Omega}{2} k\cos\theta\hat{q}_m(t) e^{i(\delta t - \phi + l\pi)} \hat{\sigma}_- + h.c.. \tag{69}$$

On the other hand, adjusting the ion-mirror distance so that the equilibrium position of the m-th ion is at an antinode of the field,

$$\hat{\zeta}_m(t) = \frac{2l-1}{4}\lambda + \hat{q}_m(t)\cos\theta, \tag{70}$$

the Hamiltonian of the interaction will be given by

$$\hat{H} = \frac{\hbar\Omega}{2} \cos\left[k\hat{q}_m(t)\cos\theta\right] e^{i(\delta t - \phi + l\pi/2)} \hat{\sigma}_- + h.c.. \tag{71}$$

Again, since we consider the displacement of the m-th ion around the equilibrium point to be sufficiently small, we can approximate $\cos\left[k\hat{q}_m(t)\cos\theta\right] \approx 1$, obtaining the interaction

$$\hat{H} \approx \frac{\hbar\Omega}{2} e^{i(\delta t - \phi + l\pi/2)} \hat{\sigma}_- + h.c.. \tag{72}$$

Using equation (62), we can write the operator $\hat{q}_m(t)$ as a function of the creation and destruction operators of the collective modes, such that

$$k\cos\theta\hat{q}_m(t) = \frac{\eta}{\sqrt{N}} \sum_{p=1}^{N} \left(\hat{a}_p^\dagger e^{i\nu_p t} + \hat{a}_p e^{-i\nu_p t}\right), \tag{73}$$

where $\eta = \sqrt{\hbar k^2 cos^2\theta/2m\nu}$ is the Lamb-Dicke parameter of the interaction. From this definition, it can be seen that the interaction constructed in equation (69) couples the internal states of the m-th ion with the vibrational states of the normal modes of the chain, while the interaction constructed in equation (72) alters only the internal states of the m-th ion, without coupling the internal states with the vibrational states of the collective modes.

The interactions built into equations (69) and (72) are essential for implementing quantum computing in trapped ion systems, as we will see in the next section. Before that, it is important to note that equation (69), unlike equation (72), depends on the number of ions in the chain, which can become a complex problem since the internal levels are coupled with all N collective modes at each pulse applied to the system. However, as noted by Cirac and Zoller [18], it is possible to obtain a sufficient condition such that equation (69) can be approximated for the interaction

$$\hat{H}_{CZ} = \frac{\hbar\Omega\eta}{\sqrt{4N}}\left(\hat{a}_1 e^{-i\nu_1 t} + \hat{a}_1^\dagger e^{i\nu_1 t}\right)e^{i(\delta t-\phi)}\hat{\sigma}_- + h.c., \quad (74)$$

in which the laser interacts only with the collective mode of the center of mass, so that the interaction of the laser with the other modes can be neglected. The Hamiltonian above is known as the Cirac-Zoller Hamiltonian. The condition under which this approximation is valid is given by

$$\left(\frac{\Omega\eta}{\sqrt{N}\nu}\right)^2 \ll 1 \quad (75)$$

and demonstrated in Appendix B.

VI. IMPLEMENTATION OF LOGIC GATES IN TRAPPED ION SYSTEMS

In a quantum computer, information is stored in qubits and manipulated via the application of logic gates. The aim of this section is to construct, from the interactions developed in a linear chain of N ions, equations (72) and (74), a set of logic gates in which any operations between the qubits can be decomposed. A set like this is called a universal set of logic gates and is not unique [46]. In 1995, Sleator and Weinfurter [47] demonstrated that a universal set of logic gates can be formed by rotations on a single qubit and by the Controlled-NOT gate – a quantum gate that acts simultaneously on two qubits, controlling their respective states. Next, we will build the aforementioned interactions into a system of N trapped ions, thus constructing a universal set of logic gates for the architecture.

A. Rotations on a Single Qubit

In a system of trapped ions, the general state of the m-th qubit of the chain is represented by the superposition of the internal levels of the ion,

$$|\Psi\rangle_m = \alpha\,|0\rangle_m + \beta\,|1\rangle_m\,, \quad (76)$$

where we map the internal states of the ion onto the states of the computational base, where α and β are complex coefficients that satisfy $|\alpha|^2 + |\beta|^2 = 1$, i.e. the normalization condition. We can then rewrite the equation (76) as

$$|\Psi\rangle_m = \cos\theta/2\,|0\rangle_m + e^{i\varphi}\sin\theta/2\,|1\rangle_m\,, \quad (77)$$

which allows us to represent any state of a qubit as a point on the surface of a sphere of unit radius, known as a Bloch sphere [3], illustrated in Figure VI A. The Bloch sphere offers a simple and intuitive way of visualizing the result of operations applied to a single qubit, which we call rotations.

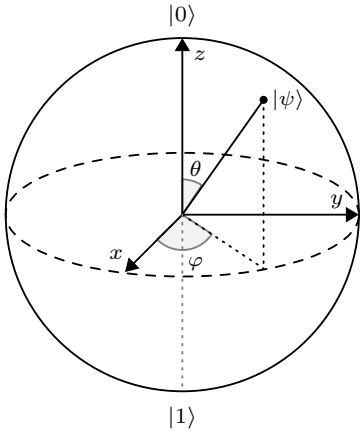

FIG. 4. Representation of an arbitrary $|\psi\rangle$ state on the surface of the Bloch sphere

.

Based on the representation of the states of the qubits as points on the surface of the Bloch sphere, applying an arbitrary rotation to the m-th qubit of a chain of N ions is analogous to performing a rotation at the point $|\Psi\rangle_m$, which represents the state of the qubit in relation to some arbitrary axis. In other words, to construct a general rotation about the m-th qubit in the chain is to construct an interaction in which a state of the computational basis of the m-th qubit, $|0\rangle_m$ or $|1\rangle_m$, is taken into the general state $\cos\theta\,|0\rangle_m + e^{i\varphi}\sin\theta\,|1\rangle_m$.

To construct an interaction with the properties discussed above, we start from the equation (72) with $\delta = 0$, adjusting the phase of the field and applying the interaction to the m-th qubit of the chain for a time $t = k\pi/\Omega$. In this way, the interaction's time evolution operator becomes

$$\hat{V}_m^k(\phi) = \exp\left\{-ik\frac{\pi}{2}\left(\sigma_+ e^{-i\phi} + \sigma_- e^{i\phi}\right)\right\}, \quad (78)$$

where k is a constant that can be adjusted to build different time evolutions. Note that the evolution described above does not act on the collective modes, which allows us to omit the vibrational states of these modes, knowing that they will not be altered by the interaction.

Applying the time evolution constructed above to the states of the computational basis of the m-th ion, we obtain

$$|0\rangle_m \xrightarrow{\hat{V}_m^k(\phi)} \cos\left(k\pi/2\right)|0\rangle_m - ie^{i\phi}\sin\left(k\pi/2\right)|1\rangle_m\,, \quad (79a)$$

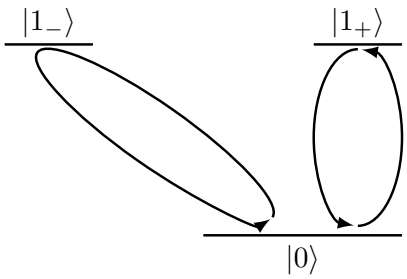

FIG. 5. Schematic representation of the internal energy levels of a trapped ion for the *CNOT* gate. The ellipses with different axes represent different polarizations of a laser with the same frequency, used to make transitions between levels. The $|1_+\rangle$ state is the state used in the computational base and the $|1_-\rangle$ state is used as an auxiliary state, for example to obtain desired rotations.

$$|1\rangle_m \xrightarrow{\hat{V}_m^k(\phi)} \cos\left(k\pi/2\right)|1\rangle_m - ie^{-i\phi}\sin\left(k\pi/2\right)|0\rangle_m . \tag{79b}$$

Thus, since the states $|0\rangle$ and $|1\rangle$ form the computational basis, equations (79a) and (79b) imply that it is possible to transform a general state such as that of equation (76) into a state such as that of equation (77) from applications of $\hat{V}_k^m(\phi)$, making it possible to perform any rotation on a qubit in the chain without altering the collective or individual states of the other qubits.

B. Controlled-NOT Gate

The Controlled-NOT (or CNOT) gate is a conditional operation performed between two qubits, denoted by the subscripts m and n. Conditional operations consist of changing the state of the n-th qubit, called the target qubit, depending on the state of the m-th qubit, called the control qubit. In particular, the action of CNOT can be described as follows: If the state of the control qubit is $|0\rangle$ ($|1\rangle$), then the state of the target qubit is not (will be) changed. To summarize:

To do this, first consider a slightly modified experimental scheme: Each ion has three internal levels, two distinct excited states, $|1_-\rangle$ and $|1_+\rangle$, and a ground state. The transitions between the ground state and the excited states are made with the same transition frequency, but with different polarizations of the incident laser, as shown in Figure 5. Effectively, we're still dealing with a two-level system, where the $|1_+\rangle$ state is mapped onto the $|1\rangle$ state of the computational base and the $|1_-\rangle$ state is only used as an auxiliary state to individually rotate the qubits.

Now, consider the time evolution operator that results from applying the interaction represented by the equation (74) for a time interval $t = k\pi\sqrt{N}/\Omega\eta$ with $\delta = -\nu_1$, i.e.,

$$\hat{U}_m^{k,q} = \exp\Big\{-ik\frac{\pi}{2}\big(\hat{a}_1\hat{\sigma}_+^q e^{-i\phi} + \hat{a}_1^\dagger\hat{\sigma}_-^q e^{i\phi}\big)\Big\}, \tag{80}$$

where $q = +, -$ represents the two possible polarizations, the rotating wave approximation having been used. Applying the time evolution above on the m-th qubit - accompanied by the vibrational state that will be altered by the interaction, we have that

$$|0\rangle_m|0\rangle \xrightarrow{\hat{U}_m^{k,q}(\phi)} |0\rangle_m|0\rangle ,$$

$$|0\rangle_m|1\rangle \xrightarrow{\hat{U}_m^{k,q}(\phi)} \cos\left(k\pi/2\right)|0\rangle_m|1\rangle - ie^{i\phi}\sin\left(k\pi/2\right)|1_q\rangle_m|0\rangle ,$$

$$|1\rangle_m|0\rangle \xrightarrow{\hat{U}_m^{k,q}(\phi)} \cos\left(k\pi/2\right)|1_q\rangle_m|0\rangle - ie^{-i\phi}\sin\left(k\pi/2\right)|0\rangle_m|1\rangle .$$

Considering the m-th and n-th ions in the chain, the application of time evolution $\hat{U}_{CNOT} = \hat{U}_m^{1,+}\hat{U}_n^{2,-}\hat{U}_m^{1,+}$ leva a

$$|0\rangle_m|0\rangle_n|0\rangle \xrightarrow{\hat{U}_m^{1,+}\hat{U}_n^{2,-}\hat{U}_m^{1,+}(0)} |0\rangle_m|0\rangle_n|0\rangle , \tag{82a}$$

$$|0\rangle_m|1\rangle_n|0\rangle \xrightarrow{\hat{U}_m^{1,+}\hat{U}_n^{2,-}\hat{U}_m^{1,+}(0)} |0\rangle_m|1\rangle_n|0\rangle , \tag{82b}$$

$$|1\rangle_m|0\rangle_n|0\rangle \xrightarrow{\hat{U}_m^{1,+}\hat{U}_n^{2,-}\hat{U}_m^{1,+}(0)} |1\rangle_m|0\rangle_n|0\rangle , \tag{82c}$$

$$|1\rangle_m|1\rangle_n|0\rangle \xrightarrow{\hat{U}_m^{1,+}\hat{U}_n^{2,-}\hat{U}_m^{1,+}(0)} -|1\rangle_m|1\rangle_n|0\rangle , \tag{82d}$$

where we set $\phi = 0$ for convenience. At first glance, the final state of these evolutions doesn't look like the port suggested at the beginning. However, by defining the normalized state base

$$|\pm\rangle = \frac{|0\rangle \pm |1\rangle}{\sqrt{2}}, \tag{83}$$

the specified Hamiltonian acts in such a way that

$$|0\rangle_m|\pm\rangle_n|0\rangle \longrightarrow |0\rangle_m|\pm\rangle_n|0\rangle , \tag{84a}$$

$$|1\rangle_m|\pm\rangle_n|0\rangle \longrightarrow |1\rangle_m|\mp\rangle_n|0\rangle . \tag{84b}$$

Therefore, by rotating the nth qubit so that $|0\rangle \to |\pm\rangle$ and $|1\rangle \to |\mp\rangle$, it is possible to implement the CNOT gate in a trapped ion chain. In fact, by choosing $\phi = \pm\pi/2$ and $k = 1/2$ in the equation (78),

$$|0\rangle_n|0\rangle \xrightarrow{\hat{V}_n^{\frac{1}{2}}(\frac{\pi}{2})} |+\rangle_n|0\rangle , \tag{85a}$$

$$|1\rangle_n|0\rangle \xrightarrow{\hat{V}_n^{\frac{1}{2}}(\frac{\pi}{2})} |-\rangle_n|0\rangle , \tag{85b}$$

$$|-\rangle_n|0\rangle \xrightarrow{\hat{V}_n^{\frac{1}{2}}(-\frac{\pi}{2})} |1\rangle_n|0\rangle , \tag{85c}$$

$$|+\rangle_n|0\rangle \xrightarrow{\hat{V}_n^{\frac{1}{2}}(-\frac{\pi}{2})} |0\rangle_n|0\rangle , \tag{85d}$$

we show that the operator $\hat{V}_n^{\frac{1}{2}}\left(\frac{\pi}{2}\right)\hat{U}_{CNOT}\hat{V}_n^{-\frac{1}{2}}\left(-\frac{\pi}{2}\right)$ acts as a CNOT gate in a general state. Another way of generating the CNOT gate, as an alternative to using lasers with different polarizations, can be found in [48].

C. Decomposition of Other Logic Gates

In addition to the representations used so far, logic gates and states can also be represented in matrix form. In matrix algebra, the $|0\rangle$ and $|1\rangle$ states that form the computational basis are defined as

$$|0\rangle \equiv \begin{pmatrix} 1 \\ 0 \end{pmatrix}, \qquad |1\rangle \equiv \begin{pmatrix} 0 \\ 1 \end{pmatrix}, \tag{86}$$

while the logic gates are represented as unitary and square matrices that act on the states of the qubits – superpositions of the states of the computational base, modifying them.

1. *Logic gates acting on a single qubit*

Considering a single qubit system, the rotations that act on the system – described by equations (79a) and (79b) – can be mathematically written as the unitary matrix 2×2

$$R(k,\phi) = \begin{pmatrix} \cos(k\pi/2) & -ie^{-i\phi}\sin(k\pi/2) \\ -ie^{i\phi}\sin(k\pi/2) & \cos(k\pi/2) \end{pmatrix}, \tag{87}$$

such that every operation on the qubit can be broken down into sequential applications of the rotation matrix.

Among the main operations applied to a single qubit, it is important to highlight the X, Y and Z operations, which are represented by their respective Pauli matrices. In order to demonstrate the process of decomposing operations that act on a single qubit, we will construct these gates - apart from a global phase α - from the rotation matrix $R(k,\phi)$.

For the execution of an X gate, we can choose $R(1,0)$ with global phase $\alpha = \pi/2$ such that

$$e^{i\pi/2}R(1,0) = e^{i\pi/2}\begin{pmatrix} 0 & -i \\ -i & 0 \end{pmatrix} = \begin{pmatrix} 0 & 1 \\ 1 & 0 \end{pmatrix}. \tag{88}$$

Similarly, we can generate the Y gate using $R(1,\pi/2)$ with $\alpha = \pi/2$, obtaining

$$Y = e^{i\pi/2}\begin{pmatrix} 0 & -1 \\ 1 & 0 \end{pmatrix}. \tag{89}$$

Finally, to obtain the port Z, we can use the relation $Z = iYX$ such that

$$Z = e^{i\pi/2}YX = e^{i3\pi/2}\begin{pmatrix} 0 & -i \\ -i & 0 \end{pmatrix}\begin{pmatrix} 0 & -1 \\ 1 & 0 \end{pmatrix} = \begin{pmatrix} 1 & 0 \\ 0 & -1 \end{pmatrix}. \tag{90}$$

2. *Logic Gates action on Two Qubits*

For systems where n qubit entanglements are handled, the computational base is made up of 2^n column matrices with 2^n entries and the logic gates are $2^n \times 2^n$ unit matrices. In the case of a system composed of two qubits, the matrices that form the computational base are

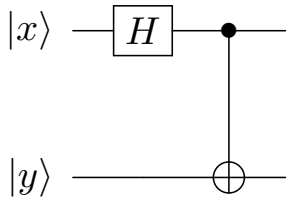

FIG. 6. Circuit representing the operations needed to create the Bell state $|\beta_{xy}\rangle$ from states in the computational base. The first operation H is called a Hadamard gate [3], and can be decomposed as a rotation of the X gate. The second operation is a CNOT gate, where the qubit $|x\rangle$ is being controlled.

$$|00\rangle \equiv \begin{pmatrix} 1 \\ 0 \end{pmatrix} \otimes \begin{pmatrix} 1 \\ 0 \end{pmatrix}, \qquad |01\rangle \equiv \begin{pmatrix} 1 \\ 0 \end{pmatrix} \otimes \begin{pmatrix} 0 \\ 1 \end{pmatrix},$$

$$|10\rangle \equiv \begin{pmatrix} 0 \\ 1 \end{pmatrix} \otimes \begin{pmatrix} 1 \\ 0 \end{pmatrix}, \qquad |11\rangle \equiv \begin{pmatrix} 0 \\ 1 \end{pmatrix} \otimes \begin{pmatrix} 0 \\ 1 \end{pmatrix}. \tag{91}$$

In addition to the computational base, Bell states $|\beta_{xy}\rangle$

$$|\beta_{00}\rangle = \frac{1}{\sqrt{2}}(|00\rangle + |11\rangle), \tag{92a}$$

$$|\beta_{01}\rangle = \frac{1}{\sqrt{2}}(|01\rangle + |10\rangle), \tag{92b}$$

$$|\beta_{10}\rangle = \frac{1}{\sqrt{2}}(|00\rangle - |11\rangle), \tag{92c}$$

$$|\beta_{11}\rangle = \frac{1}{\sqrt{2}}(|01\rangle - |10\rangle), \tag{92d}$$

form another important basis for quantum computing, being the first gate to act in many quantum algorithms, such as the algorithms of Shor [49], Deutsch-Jozsa [50], Grover [51] and Bernstein [52].

Bell states can be easily generated from the computational base using the sequence of operations shown in the circuit in Figure 6, which involves a Hadamard gate, represented mathematically by

$$H = \begin{pmatrix} 1 & 1 \\ 1 & -1 \end{pmatrix} = X\,R\Big(\frac{1}{2},\frac{\pi}{2}\Big), \tag{93}$$

and a CNOT port. Thus, using the method for generating the CNOT gate obtained in section VI B and the decomposition of the Hadamard gate, it is possible to generate the base formed by Bell states from the computational base.

VII. QUANTUM TELEPORTATION ALGORITHM

Formulated by Bennett *et al.* [53] in 1993, the quantum teleportation algorithm was experimentally verified in photonic systems [54, 55] in 1997 and in trapped ion systems by Riebe *et al.* [56] and Barrett *et al.* [57] in 2004. The protocol developed is not related to the teleportation of physical objects, but rather to the transmission of information – more specifically, the transmission of the state of a qubit – over an arbitrary distance in a secure and efficient manner. The aim of this section is to discuss how the quantum teleportation algorithm can be implemented in trapped ion systems from the logic gates built in the previous sections, following the reference [56].

To do this, imagine the following situation: Alice, who has ion A, wants to send the information contained in the internal states of her ion to a distant friend, Bob, who has ion C. Alice consults Figure 7, which describes the quantum teleportation algorithm and realizes that she will need an auxiliary ion, also in her possession, which she names the B ion.

In the first part of the algorithm, we assume that Alice's and Bob's ions have previously been prepared in the $|1\rangle_A |1\rangle_B |1\rangle_C$ state and then it is possible to generate the superposition state

$$|\Psi\rangle = |1\rangle_A \otimes \left(|0\rangle_B |1\rangle_C + |1\rangle_B |0\rangle_C \right)/\sqrt{2},$$

in which a Bell state of the form explained in the equation (92b) is constructed between the B and C ions. Once the superposition has been prepared, Alice then modifies, using sequential rotations represented by the U_χ gate, the state of the A ion to the state to be teleported to Bob, $|\chi\rangle = a|0\rangle + b|1\rangle$, such that

$$|\Psi\rangle = \left(a|0\rangle_A + b|1\rangle_A\right) \otimes \frac{(|0\rangle_B |1\rangle_C + |1\rangle_B |0\rangle_C)}{\sqrt{2}}.$$

Next, a controlled Hadamard-CNOT-Hadamard operation – also known as *CZ*, an operation of the type σ_z controlled by the qubit B, which can also be performed from the sequence of operations presented by the equations (82) – is performed between ions A and B followed by the application of a rotation $R(1/2, \pi/2)$ to each ion. At that moment, the state describing the system is given by

$$\begin{aligned} |\Psi\rangle = \quad & -\frac{1}{2} |0\rangle_A |0\rangle_B (a|0\rangle_C + b|1\rangle_C) \\ & +\frac{1}{2} |0\rangle_A |1\rangle_B (b|0\rangle_C + a|1\rangle_C) \\ & +\frac{1}{2} |1\rangle_A |0\rangle_B (-a|0\rangle_C + b|1\rangle_C) \\ & +\frac{1}{2} |1\rangle_A |1\rangle_B (-b|0\rangle_C + a|1\rangle_C). \end{aligned}$$

The state constructed above has an interesting feature that makes the quantum teleportation protocol feasible. By performing a measurement on the states of the A and B ions, Alice causes the state of the C ion to be projected into a superposition of the $|0\rangle_C$ and $|1\rangle_C$ states, whose coefficients are related to the state you want to teleport. This new superposition can then be measured by Bob – before applying the conditional operations Z and X that finalize the algorithm – such that, with a statistical treatment of the measurements, the amplitudes of the state $|\chi\rangle$ previously known only to Alice can now be known to Bob, and the information has been successfully teleported. It is important to note that, due to the sequential operations performed on the A ion and the detection performed, the original state is erased from the A ion at the end of the algorithm's execution, which can be seen as a consequence of the Non-Cloning Theorem [3]. As a way of confirming the success of the algorithm, it is possible to apply the U_χ^{-1} gate to the state teleported to Bob, hoping that the $|1\rangle$ state will be obtained in less than one global phase.

VIII. STATE OF THE ART

The architecture for quantum computing based on trapped ions consists of a system made up of many atoms, which are confined in a certain region of space by electromagnetic traps. Although this platform presents promising results, made possible by the high degree of control over the ion chain and the high precision of the laser pulses applied to realize logic gates, trapped ion systems are at the center of important research aimed at improving the conditions for their implementation and for the development of quantum computers for industrial and commercial use.

Much of the progress made on ion platforms consists of optimizing and increasing the degree of control of operations that are already implementable. Current examples of operation and control optimization include methods for reducing the cost of gates that produce entanglement between two *qubits* by using optimized pulses that require less energy in certain parameter regimes [58], procedures for efficiently entangling arbitrary pairs of ions in a chain [59] using amplitude-modulated laser pulses applied directly to individual ions in the chain,

In addition to technological advances, there is great interest in making trapped ion architectures available for commercial use. In this regard, the American company IonQ [21], a pioneer in the field, which uses ytterbium (Yb) atoms in its devices, stands out. Founded in 2015, IonQ provides access to its quantum computers via the Amazon Braket [60] and Azure Quantum [61] platforms of technology giants Amazon and Microsoft, respectively. The quantum computers available on the platforms have 11 qubits with a fully interconnected topology, as shown in Figure 8, allowing a two-qubit gate to act on any pair of qubits in the chain, a unique feature of ion platforms. The average fidelity in the application of logic gates is over 99.5% for gates acting on a single qubit and over 97.5% for gates acting on two qubits. More technical information about the quantum computer and algorithm implementations can be found at [62], demonstrating the operation (and interconnectivity) of the machine.

Recently, IonQ announced the future launch of a machine with 32 interconnected qubits, scheduled for the year 2022 [63]. In its public *roadmap*, it plans to launch a quantum

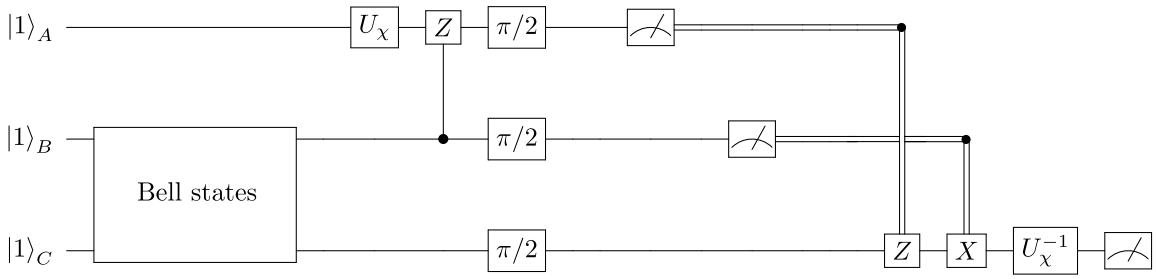

FIG. 7. Quantum teleportation algorithm performed by a trapped ion system. Adapted from [56].

computer with 256 qubits by 2026 and with 1024 qubits by 2028. However, despite the highly promising results shown by trapped ion systems, there are still difficulties and challenges that must be discussed when considering the prospect of a quantum computer based on trapped ions for practical use, with tens of thousands of qubits, including error correction protocols and system decoherence. Among these challenges, the most important is to progressively increase the number of qubits in the traps without losing individual control and, therefore, the high fidelity in the application of logic gates demonstrated by quantum computers with few ions. Possible solutions for different models of quantum computers based on trapped ion architectures, including the one exposed in this article, can be found in (Sec. IV, [17]). One of these solutions, for example, is to compartmentalize the linear chain into smaller chains, divided into modules, which has the consequence of making it difficult to manipulate each module without damaging the fidelity obtained with the logic gates and avoiding any other type of loss of quantum information.

Finally, among the initiatives in development that are attracting attention to the area, it is worth highlighting the intergovernmental project AQTION (*Advanced Quantum computing with Trapped IONs*) [23] which aims to build a quantum computer based on trapped ions with a forecast of raising 1 billion euros between 2018 and 2028. In 2021, an article published by the initiative in the scientific journal *PRX Quantum* demonstrated the ability to build a quantum state with 24 entangled ions in a quantum computer that occupies the space of just $1.7\,m^3$ [65], which represents a first step towards miniaturizing the components needed to engineer such technologies.

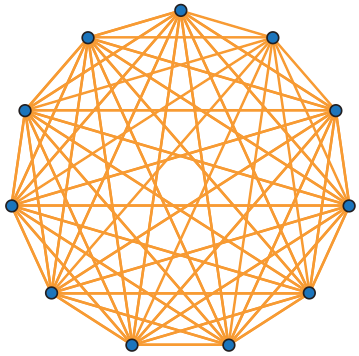

FIG. 8. Topology of the American company IonQ quantum computer with 11 fully interconnected qubits. Taken from [60].

IX. CONCLUSIONS

In this article, we aimed to present the characteristics that guarantee that trapped ion systems are architectures for implementing quantum computing. To this end, considering the circuital model of quantum computing, we discussed how the internal levels of a single trapped ion can be mapped onto the computational basis of a *qubit* and how laser pulses can be used to generate interactions that act as logic gates in the system. With the intention of demonstrating the ease with which the architecture can be scaled up to a certain limit, we expand the discussion to a chain of N trapped ions, in which the normal modes of the chain serve as the basis for generating interactions that allow different pairs of qubits to be connected. As an application, we discuss the implementation of the quantum teleportation algorithm. Finally, we present the current state of the art of the architecture, exposing the advantages and current limitations of the system.

In conclusion, trapped ion systems present characteristics that hold great expectations for the future of this architecture, such as high fidelity in the generation of logic gates and different proposals for dealing with the challenges of scalability. In addition, the interconnectivity between qubits is an aspect of the architecture that, although its importance is not fully understood, has great potential to increasingly favor these systems, as high financial investments from intergovernmental projects such as AQTION and commercial companies such as IonQ and AQT already indicate. In this sense, in addition to the different future prospects for the area, trapped ion platforms allow us to explore unique possibilities in the implementation of algorithms in quantum computers, which makes the architecture a source of learning in many exclusive terms for the evolution, development and implementation of quantum computing.

ACKNOWLEDGMENTS

This work was supported by Conselho Nacional de Desenvolvimento Científico e Tecnológico (CNPq), Coordenação

de Aperfeiçoamento de Pessoal de Nível Superior (CAPES) - Code 001, and the National Institute of Science and Technology for Quantum Information (INCT-IQ/CNPq), Process No. 465469/2014-0. C.J.V.-B. also gratefully acknowledges the support of Fundação de Amparo à Pesquisa do Estado de São Paulo (FAPESP) (FAPESP), Process No. 2019/11999-5 and 2019/13143-0, and CNPq, Process No. 311612/2021-0.

APPENDIX A - PAULI MATRICES

The Pauli matrices $(\hat{\sigma}_x, \hat{\sigma}_y, \hat{\sigma}_z)$ form a set of three 2×2 Hermitian matrices that are originally related to the interaction between a $1/2$ spin particle and an electromagnetic field [40], and are represented by

$$\hat{\sigma}_x = \begin{pmatrix} 0 & 1 \\ 1 & 0 \end{pmatrix}, \quad \hat{\sigma}_y = \begin{pmatrix} 0 & -i \\ i & 0 \end{pmatrix}, \quad \hat{\sigma}_z = \begin{pmatrix} 1 & 0 \\ 0 & -1 \end{pmatrix}.$$

Together with the identity matrix 2×2, the Pauli matrices form the spin algebra $1/2$, i.e. they generate the space of operators that act on the Hilbert space of two-level systems. In this way, any operator that acts on the qubits of a quantum computer can be mapped onto combinations of this set of matrices. In this sense, it is worth

$$|g\rangle\langle g| + |e\rangle\langle e| \to \hat{\mathbb{I}}, \quad |g\rangle\langle g| + |e\rangle\langle g| \to \hat{\sigma}_x, \; i(|g\rangle\langle e| - |e\rangle\langle g|) \to \hat{\sigma}_y, |e\rangle\langle e| - |g\rangle\langle g| \to \hat{\sigma}_z,$$

as should be easy to see. Furthermore, from the combination of the Pauli matrices

$$\hat{\sigma}_\pm = \frac{\hat{\sigma}_x \pm i\hat{\sigma}_y}{2}, \tag{94}$$

can be mapped

$$|e\rangle\langle g| \to \hat{\sigma}_+, \qquad |g\rangle\langle e| \to \hat{\sigma}_-,$$

where $\hat{\sigma}_+$ and $\hat{\sigma}_-$ act as qubit excitation and de-excitation operators, as we can see from their respective definitions.

APPENDIX B - CIRAC-ZOLLER HAMILTONIAN

The aim of this appendix is to find the necessary condition for the interaction that couples the internal state of the m-th ion to the N collective states of the motion of the ions in the chain,

$$\hat{H} = \frac{\hbar\Omega\eta}{\sqrt{4N}} \sum_{p=1}^{N} \left(\hat{a}_p^\dagger e^{i\nu_p t} + \hat{a}_p e^{-i\nu_p t}\right) e^{i(\delta t - \phi)}\hat{\sigma}_- + h.c., \tag{95}$$

can be approximated for the Cirac-Zoller Hamiltonian,

$$\hat{H}_{CZ} = \frac{\hbar\Omega\eta}{\sqrt{4N}}\left(\hat{a}_1 e^{-i\nu_1 t} + \hat{a}_1^\dagger e^{i\nu_1 t}\right)e^{i(\delta t - \phi)}\hat{\sigma}_- + h.c, \tag{96}$$

that couples the internal states of the m-th ion only to the vibrational mode of the center of mass of the chain. The condition under which this approximation is valid was introduced by James [20] and is presented below.

To do this, we assume that the wave function of the m-th ion of the chain interacting with a laser is a superposition of the coupling of the internal states with the N collective vibrational modes that can be expressed as

$$\begin{aligned} |\Psi(t)\rangle = \alpha_0(t)\,|g\rangle\,|0\rangle + \beta_0(t)\,|e\rangle\,|0\rangle + \\ + \sum_{p=1}^{N} \alpha_p(t)\,|g\rangle\,|1_p\rangle + \sum_{p=1}^{N} \beta_p(t)\,|e\rangle\,|1_p\rangle\,, \end{aligned} \tag{97}$$

where we choose the order of the kets in such a way that the kets of the internal states, $|g\rangle$ and $|e\rangle$, are represented in front of the vibrational states.

In this way, the equation of motion of the wave function that describes the behavior of the m-th ion is therefore given by

$$i\hbar\frac{\partial}{\partial t}\,|\Psi(t)\rangle = \hat{H}\,|\Psi(t)\rangle\,, \tag{98}$$

from where, choosing $\delta = -\nu_1$ so that the laser is in resonance with the mode of the center of mass, it is possible to obtain

$$\dot{\alpha}_0 = \frac{\Omega\eta}{\sqrt{N}} \sum_{p=1}^{4N} s_m^{(p)} \beta_p(t), \tag{99}$$

$$\dot{\beta}_0 = \frac{\Omega\eta}{\sqrt{4N}} \sum_{p=1}^{N} s_m^{(p)} \alpha_p(t), \tag{100}$$

$$\dot{\alpha}_p(t) = -i(\nu_p - \nu_1)\alpha_p - \frac{\Omega\eta}{\sqrt{4N}} s_m^{(p)} \beta_p(t), \tag{101}$$

$$\dot{\beta}_p = -i(\nu_p + \nu_1)\beta_p - \frac{\Omega\nu}{\sqrt{4N}} s_m^{(p)} \alpha_0(t). \tag{102}$$

Furthermore, we know that

$$\sum_{p=0}^{N} |\alpha_p(t)|^2 + |\beta_p(t)|^2 = 1, \tag{103}$$

which allows us to write, using the triangle inequality,

$$|(\nu_p - \nu_1)\alpha_p(t)| = \left|\dot{\alpha}_p + \frac{\Omega\eta}{\sqrt{4N}} s_m^{(p)} \beta_0(t)\right| \leq 2\frac{\Omega\eta}{\sqrt{4N}}|s_m^{(p)}|, \tag{104}$$

$$|\beta_p(t)| \leq \frac{\Omega_0\eta}{\sqrt{N}(\nu_p + \nu_1)}|s_m^{(p)}|, \tag{105}$$

so that the probability of finding the ion outside the center-of-mass mode is given by

$$P_m = \sum_{p=2}^{N} |\alpha_p(t)|^2 + |\beta_p(t)|^2 \tag{106}$$

$$\leq 2\left(\frac{\Omega\eta}{\sqrt{N}\nu}\right)^2 \sum_{p=2}^{N} \frac{\mu_p + 1}{(\mu_p - 1)^2}|s_m^{(p)}|^2. \tag{107}$$

However, this probability is only related to the m-th ion in the chain and will be different for each ion. We must consider the average probability over the entire chain, which is given by

$$\overline{P} = \frac{1}{N}\sum_{m=1}^{N} P_i = \frac{2}{N}\left(\frac{\Omega\eta}{\sqrt{N}\nu}\right)^2 \left[\sum_{m,p}\frac{\mu_p+1}{(\mu_p-1)^2}|s_m^{(p)}|^2\right]$$

$$\leq 2\left(\frac{\Omega\eta}{\sqrt{N}\nu}\right)^2 \sum_{p=2}^{N}\frac{\mu_p+1}{(\mu_p-1)^2}\sup_{m,t}|s_m^{(p)}|^2 = 2\left(\frac{\Omega\eta}{\sqrt{N}\nu}\right)^2 \Sigma(N),$$

where

$$\Sigma(N) = \sum_{p=2}^{N}\frac{\mu_p+1}{\sqrt{\mu_p}(\mu_p-1)^2}. \tag{108}$$

Numerically, it is possible to show that $\Sigma(N)$ is increasing and tends to 0.82 for sufficiently large N. Therefore,

$$\overline{P} \leq 1,69\left(\frac{\Omega\eta}{\sqrt{N}\nu}\right)^2 \tag{109}$$

must be much smaller than unity for Cirac and Zoller's approximation to be valid.

[1] A. Streltsov, G. Adesso e M.B. Plenio, Rev. Mod. Phys. **89**, 041003 (2017).
[2] R. Horodecki, P. Horodecki, M. Horodecki e K. Horodecki, Rev. Mod. Phys. **81**, 865 (2009).
[3] M.A. Nielsen e I.L. Chuang, *Quantum Computation and Quantum Information* (Cambridge University Press, Cambridge, 2010).
[4] H. Jack, *Quantum computing: an applied approach* (Springer, Cham, 2019).
[5] A. Montanaro, npj Quantum Information **2**, 1 (2016).
[6] D. Deutsch e R. Jozsa, Proceedings of Royal Society in London A **439**, 553 (INSERIR ANO).
[7] F. Arute, K. Arya, R. Babbush, D. Bacon, J.C. Bardin, R. Barends, R. Biswas, S. Boixo, F.G. Brandao, D.A. Buell et al., Nature **574**, 505 (2019).
[8] P. Nimbe, B. Weyori e F. Adekoya, Quantum Information Processing **20**, 1 (2021).
[9] A. Steane, Reports on Progress in Physics **61**, 117 (1998).
[10] A. Barenco, C.H. Benneet, R. Cleve, D.P. DiVincenzo, N. Margolus, P. Shor, T. Sleator, J. Smolin e H. Weinfurter, Physical Review A **52**, 3457 (1995).
[11] D.P. DiVincenzo, Fortschritte der Physik: Progress of Physics **48**, 771 (2000).
[12] T.D. Ladd, F. Jelezko, R. Laflamme, Y. Nakamura, C. Monroe e J.L. O'Brien, Nature **464**, 45 (2010).
[13] S. Slussarenko e G.J. Pryde, Applied Physics Reviews **6**, 041303 (2019).
[14] M. Kjaergaard, M.E. Schwartz, J. Braumüller, P. Krantz, J.I.J. Wang, S. Gustavsson e W.D. Oliver, Annual Review of Condensed Matter Physics **11**, 369 (2020).
[15] A. Steane, Applied Physics B **64**, 623 (1997).
[16] H. Haffner, C. Roos e R. Blatt, Physics Reports **469**, 155 (2008).
[17] C.D. Bruzewicz, J. Chiaverini, R. McConnell e J.M. Sage, Applied Physics Reviews **6**, 021214 (2019).
[18] J.I. Cirac e P. Zoller, Phys. Rev. Lett. **74**, 4091 (1995).
[19] R. Blatt e D. Wineland, Nature **453**, 1008 (2008).
[20] D.F.V. James, Applied Physics B **66**, 181 (1998).
[21] https://ionq.com/, acessado em 30/05/2022.
[22] https://www.aqt.eu/, acessado em 30/05/2022.
[23] https://www.aqtion.eu/, acessado em 30/05/2022.
[24] H.G. Dehmelt, em: *Advances in Atomic and Molecular Physics*, editado por D.R. Bates e I. Estermann (Harcourt Brace Jovanovic, New York, 1968), v. 3.
[25] H.G. Dehmelt, em: *Advances in Atomic and Molecular Physics*, editado por D.R. Bates e I. Estermann (Harcourt Brace Jovanovic, New York, 1969), v. 5.
[26] W. Paul, Reviews of Modern Physics **62**, 531 (1990).
[27] https://www.nobelprize.org/prizes/physics/1989/summary/, acessado em 30/05/2022.
[28] D. Leibfried, R. Blatt, C. Monroe e D. Wineland, Rev. Mod. Phys. **75**, 281 (2003).
[29] D.J. Griffiths, *Introduction to Electrodynamics* (Pearson, Boston, 2013).
[30] É. Mathieu, *Course de Physique Mathématique* (Gauthier-Villars, Paris, 1873).
[31] M.O. Scully e M.S. Zubairy, *Quantum Optics* (Cambridge Universty Press, Cambridge, 1999).
[32] D.F. Walls e G.J. Milburn, *Quantum Optics* (Springer-Verlag, Berlim, 2008).
[33] S. Lloyd, Universal Quantum Simulation, Science **273**. 1074 (1996).
[34] G.J. Milburn e S.L. Braunstein, Phys. Rev. A **60**, 937 (1999).
[35] A.F.R.T. Piza, *Mecânica Quântica* (Edusp, São Paulo, 2003).
[36] C. Cohen-Tannoudji, B. Diu e F. Laloe, *Quantum Mechanics* (Wiley, New York, 1978), v.2.
[37] A. Lemmer, Quantum Dynamics with Trapped Ions. Tese de Doutorado, Universidade de Ulm, Baden-Württemberg (2017).
[38] D. Braak, Physical Review Letters **107**, 100401 (2011).
[39] H. Zhong, X. Qiongtao, M. Batchelor, T. Murray e C. Lee, Journal of Physics A: Mathematical and Theoretical **46**, 415302 (2013).
[40] J.J. Sakurai e J. Napolitano, *Modern Quantum Mechanics* (Cambridge University Press, Cambridge, 2017).
[41] R. Blatt, em: *École d' été de Physique des Houches Session LXXIX Course 5*, editado por D. Estève, J.Raimond e J. Dalibard (Elsevier, Londres, 2004).
[42] A. Steane, em: *Proceedings of the International School of Physics "Enrico Fermi", Course CLXII*, editado por G. Casati, D.L. Shepelyansky e P. Zoller (IOS Press, Amsterdã, 2006).
[43] H. Goldstein, C. Poole e J. Safko, *Classical Mechanics* (Addison-Wesley, Boston, 2001).
[44] S. Thornton e J. Marion, *Classical Dynamics of Particles and Systems* (Cengage Learning, Boston, 2003).

[45] H.C. Nägerl, D. Leibfried, F. Schmidt-Kaler, J. Eschner e R.Blatt, Optics Express **3**, 89 (1998).

[46] D.E. Deutsch, A. Barenco e A. Ekert, Proceedings of the Royal Society of London A **449**, 669 (1995).

[47] T. Sleator e H. Weinfurter, Phys. Rev. Lett. **74**, 4087 (1995).

[48] S. Gulde, M. Riebe, G.P.T. Lancaster, C. Becher, J. Eschner, H. Häffner, F. Schmidt-Kaler, I.L. Chuang e R. Blatt, Nature **421**, 48 (2003).

[49] P.W. Shor, em: *Proceedings of the 35th Annual Symposium on Foundations of Computer Science* (Washington, 1994).

[50] D. Deutsch e R. Jozsa, Proceedings of the Royal Society of London Series A **439**, 553 (1992).

[51] L. K. Grover, em: *Proceedings of the 28th Annual ACM symposium on Theory of Computing, ACM Press* (New York, 1996).

[52] E. Bernstein e U. Vazirani, SIAM Journal on Computing 5 **26**, 1411 (1997).

[53] C. Bennet, G. Brassard, C. Crépeau, R. Josza, A. Peres e W.K. Wootters, Physical Review Letters **70**, 1895 (1993).

[54] D. Bouwmeester, J. Pan, K. Mattle, M. Eibl, H. Weinfurter e A. Zeilinger, Nature **390**, 575 (1997).

[55] D. Boschi, S. Branca, F. de Martini, L. Hardy e S. Popescu, Physical Review Letters **80**, 1121 (1998).

[56] M. Riebe, H. Häffner, C.F. Roos, W. Hänsel, J. Benhelm, G.P.T. Lancaster, T.W. Körber, C. Becher, F. Schmidt-Kaler, D.F.V. James et al., Nature **429**, 734(2004).

[57] M.D. Barrett, J. Chiaverini, T. Schaetz, J. Britton, W.M. Itano, J.D. Jost, E. Knill, C. Langer, D. Leibfried, R. Ozeri et al., Nature **492**, 737 (2004).

[58] R. Blümel, N. Grzesfiak, N.H. Nguyen, A.M. Green, M. Li, A. Maksymov, N.M. Linke e Y. Nam, Phys. Rev. Lett. **126**, 220503 (2021).

[59] N. Grzesiak, R. Blümel, K. Wright, K.M. Beck, N.C. Pisenti, M. Li, V. Chaplin, J.M. Amini, S. Debnath, J. Chen et al., Nat Commun **11**, 2963 (2020).

[60] https://aws.amazon.com/pt/braket/, acessado em 30/05/2022.

[61] https://azure.microsoft.com/pt-br/services/quantum/, acessado em 30/05/2022.

[62] K. Wright, K.M. Beck, S. Debnath, J.M. Amini, Y. Nam, N. Grzesiak, J.S. Chen, N.C. Pisenti, M. Chmielewski, C. Collins et al., Nature Communications **10**, 5464 (2019).

[63] P. Chapman, *Introducing the World's Most Powerful Quantum Computer*, disponível em: https://ionq.com/posts/october-01-2020-introducing-most-powerful-quantum-computer, acessado em 30/05/2022.

[64] P. Chapman, *Scaling IonQ's Quantum Computers: the Roadmap*, disponível em: https://ionq.com/posts/december-09-2020-scaling-quantum-computer-roadmap, acessado em 30/05/2022.

[65] I. Pogorelov, T. Feldker, C.D. Marciniak, L. Postler, G. Jacob, O. Krieglsteiner, V. Podlesnic, M. Meth, V. Negnevitsky, M. Stadler et al., PRX Quantum **2**, 020343 (2021).

7 Impact of temporal correlations, coherence and postselection on two-photon interference

Impact of temporal correlations, coherence, and postselection on two-photon interference

Fernando Redivo Cardoso,[1,2] Jaewon Lee,[2] Riccardo Checchinato,[2] Jan-Heinrich Littmann,[2] Marco De Gregorio,[3] Sven Höfling,[3] Christian Schneider,[4] Celso J. Villas-Boas,[1] and Ana Predojević[2,*]

[1]*Departamento de Física, Universidade Federal de São Carlos, 13565-905 São Carlos, São Paulo, Brazil*
[2]*Department of Physics, Stockholm University, 10691 Stockholm, Sweden*
[3]*Technische Physik, Physikalisches Institut and Würzburg-Dresden Cluster of Excellence ct.qmat, Universität Würzburg, Am Hubland, D-97074 Würzburg, Germany*
[4]*Institut of Physics, University of Oldenburg, D-26129 Oldenburg, Germany*

Two-photon interference is an indispensable resource in quantum photonics, but it is not straightforward to achieve. The cascaded generation of photon pairs contains intrinsic temporal correlations that negatively affect the ability of such sources to perform two-photon interference, thus hindering applications. We report on how such correlation interplays with decoherence and temporal postselection, and under which conditions temporal postselection could improve two-photon interference visibility. Our study identifies crucial parameters and points the way to a source with optimal performance.

Photons are a highly suitable choice for flying qubits due to their ease of generation, ability to carry encoding in various degrees of freedom, and low decoherence resulting from low interaction with the environment. The latter comes at a cost of a limited means to enable photons to interact. The primary method for achieving photon interaction is through two-photon interference on a beamsplitter, also known as the Hong-Ou-Mandel interference [1]. The use of this effect spans numerous platforms and applications, including operations such as teleportation [2] and entanglement swapping [4], linking quantum systems [5, 6], photonic circuits [7], fusing of photonic states [8], and state control and characterization [9].

Spontaneous parametric downconversion and quantum dots are the two most commonly used systems to generate bipartite photon entanglement. In the case of spontaneous parametric downconversion, the high two-photon interference contrast is engineered by modifying the joined-spectral amplitude [10] and eliminating the underlying correlations by means of spectral filtering. In contrast to spontaneous parametric downconversion, where the two photons are generated simultaneously, a quantum dot emits a pair of photons as a time-ordered cascade, with the biexciton photon preceding the exciton photon. The resulting two-photon wave function describing the cascade emission has the following form [11, 12]

$$\psi(t_b,t_x)=2\sqrt{\Gamma_b\Gamma_x}\mathrm{e}^{-\Gamma_b t_b}\Theta(t_b)\mathrm{e}^{-\Gamma_x(t_x-t_b)}\Theta(t_x-t_b), \tag{1}$$

where t_b (t_x) is the emission time of the biexciton (exciton) photon, while Γ_b (Γ_x) denotes the biexciton (exciton) decay rate. The factor $\Theta(t_x-t_b)$ has the form of a Heaviside step function and accounts for the temporal ordering (cascade emission) that induces correlations between the emitted photons [11, 12]. The extent of the correlations between the two photons, and hence, the purity of a single photon belonging to a pair, can be quantified by determining the trace of the squared reduced density operator [13]. Due to the form of the two-photon wave function, $\psi(t_b,t_x)$, tracing over the biexciton (exciton) photon subsystem will reveal that the exciton (biexciton) is not in a pure state. For example, by denoting $\rho_x=\mathrm{Tr}_b(\psi^*\psi)$, we obtain [12] the purity of the exciton photon as

$$\mathrm{Tr}\left(\rho_x^2\right)=\frac{\Gamma_b}{\Gamma_b+\Gamma_x}. \tag{2}$$

The upper bound of $\mathrm{Tr}\left(\rho_x^2\right)$ is unity and manifests itself in the case the state is pure. Hence, $\Gamma_x \ll \Gamma_b$ implies high purity, a condition required to achieve high visibility contrast in two-photon interference experiments. On the other hand, $\Gamma_x \gg \Gamma_b$ indicates that the temporal correlations described by $\psi(t_b,t_x)$ are strong and that they would lead to a reduction of purity of the individual photons pertaining to a photon pair.

In a quantum dot embedded in a bulk material, the biexciton and exciton decay times are comparable [15, 16]. As a result, the two-photon interference visibility observed in the experiments rarely exceeded 0.5 [14]. On the other hand, the ability to use photon pairs generated by a single quantum dot in experiments that rely on two-photon interference [2, 4] is an essential prerequisite for their use. Therefore, there is a need for an in-depth analysis of the origins of the low interference contrast and mitigation strategies. Here, we theoretically and experimentally investigate how the visibility of the two-photon interference is affected by temporal correlations, decoherence, and the temporal postselection. Our results identify the strategy required to maximize the visibility.

The measurements were performed using an In(Ga)As quantum dot embedded in a micropillar cavity. The cavity was designed to feature a low quality factor (200-300) and in return provide a bandwidth of ∼5 nm [17]. The quantum dot was excited resonantly by means of two-photon resonant excitation of the biexciton [18]. To this end, we employed an excitation laser featuring 80 MHz repetition rate and a pulse length of 15 ps. The excess laser scattering was removed by means of spectral and polarization filtering. The biexciton and exciton single photons were separated using a diffraction grating and coupled into single mode fibers. The low multi-photon contribution in the quantum dot emission was confirmed by measuring the auto-correlation function (shown

in [19]). The measurements yield $g_b^{(2)}(0)$=0.0144(19) for biexciton and $g_x^{(2)}(0)$=0.0074(11) for exciton photons. We also performed lifetime measurements and obtained $\tau_b = 237.16(59)$ ps and $\tau_x = 367.61(99)$ ps for the biexciton and exciton, respectively (data plots and the respective fits are given in [19]). The ratio of the lifetimes indicates that the correlations between the biexciton and the exciton emission time should significantly reduce the purity of the individual photons [20]. However, to determine the upper bound of the two-photon interference visibility we had to employ a theoretical model.

We modeled the quantum dot as a three-level system consisting of a ground state, exciton, and biexciton, as shown in Fig. 1a. Once the quantum dot is two-photon resonantly excited it decays to the ground state via emission of photons with frequencies ω_1 (biexciton) and ω_2 (exciton). The full description of the system dynamics is given in [19].

Two indistinguishable photons impinging on the beamsplitter will undergo interference [21]. If we denote the beamsplitter input modes as a and b, the time-resolved interference of two photons emitted by independent sources is given by [22, 23]

$$G^{(2)}_{HOM}(t,\tau) = \frac{1}{2}\left[\left\langle \xi_a^\dagger(t)\xi_a(t)\right\rangle \left\langle \xi_b^\dagger(t+\tau)\xi_b(t+\tau)\right\rangle - 2\,\mathrm{Re}\left\{\left(G_a^{(1)}(t,\tau)\right)^* G_b^{(1)}(t,\tau)\right\}\right]. \quad (3)$$

In the equation above the $n_a(t) = \left\langle \xi_a^\dagger(t)\xi_a(t)\right\rangle$ and $n_b(t+\tau) = \left\langle \xi_b^\dagger(t+\tau)\xi_b(t+\tau)\right\rangle$ are values of photon number in modes a and b and, as such, are proportional to the intensity in the respective mode. On the other hand, $G^{(1)}_{a,b}(t,\tau)$ is the first-order (field) correlation function. The function describing the two-photon interference is the second-order (intensity) correlation function $G^{(2)}_{HOM}(t,\tau)$.

To calculate the first-order correlation function, we implemented the sensor method [24]. This approach is based on supplementing the three-level system by weakly coupled quantized radiation modes (two-level systems) that act as sensors. Here, we introduced two such sensors (one per emission frequency) and they are described by the following Hamiltonian

$$H_s = \sum_{j=1}^{2}\left\{\omega_j \xi_j^\dagger \xi_j + g\left[\left(\sigma_{xb}+\sigma_{gx}\right)\xi_j^\dagger + \mathrm{h.c.}\right]\right\}, \quad (4)$$

where ω_j is the resonance frequency, while $\xi_j^\dagger$ (ξ_j) correspond to the creation (annihilation) operator for a sensor j. The coupling strength between the sensors and the quantum dot is given by g. The presence of the sensors must not perturb the three-level system by, for example, introducing back action from the sensed excitation. Therefore, the parameter g must be very small (we consider $g = 10^{-3}$). The detailed description of the sensor method is given in [19].

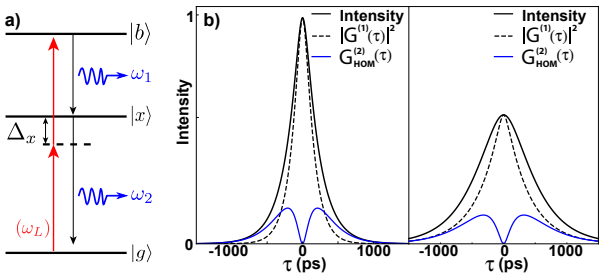

FIG. 1: (a) Schematic of the three-level system. A laser with a frequency ω_L coherently couples the ground state, $|g\rangle$, and the biexciton, $|b\rangle$, via a virtual level. Upon excitation, the biexciton photon, ω_1, and exciton photon, ω_2, are emitted. The two-photon resonance is detuned from the single-photon resonance (ground state, $|g\rangle$, to exciton, $|x\rangle$) by Δ_x. (b) The results of the sensor method simulation: intensity, first-order correlation function, $G^{(1)}(\tau)$ and second-order correlation function, $G^{(2)}_{HOM}(\tau)$, for the biexciton (left) and the exciton (right). For optimal comparison of the two plots, the area under the intensity peak was scaled to unity. The simulation assumed the experimentally determined biexciton and exciton lifetimes ($\tau_b = 237.16(59)$ ps and $\tau_x = 367.61(99)$ ps) and no dephasing. These results yield two-photon coincidence probability of $P_0 = 0.15$ while the visibility is equal to ν=0.54 for both the biexciton and the exciton photon.

The sensor method allows the treatment of photon correlations taking into account the uncertainties in time and frequency of the detection [24]. Hence, it is the ideal approach to quantify the correlations present in quantum dot emission. We employed it to calculate the photon number and the first-order correlation function of the sensor modes. By replacing these in (3) and integrating over t, we obtain the $G^{(2)}_{HOM}(\tau)$. Similarly, by integrating the individual terms in (3) one obtains the correlation in photon number and $G^{(1)}(\tau)$, respectively. The results are shown in Fig. 1b. They yield the probability of a coincidence at the outputs of the beamsplitter of $P_0 = 0.15$. While this value is significantly lower than the classical limit of $P_\infty = 0.5$, imposed by full absence of the interference effect, it demonstrates the detrimental effect of the temporal correlations. The corresponding visibility ν is 0.54, where the visibility is defined as $(P_\infty - P_0)/(P_\infty + P_0)$ [25].

We accessed P_0 and ν experimentally. To achieve this we employed two unbalanced interferometers with a nominal delay of 3 ns. The first interferometer served to generate two laser pulses required to excite the quantum dot, while we used the second interferometer to observe two-photon interference of photons emitted in two consecutive excitations. The detailed schematic of the setup is given in [26]. The results of these measurements are shown as points in Fig. 2c and Fig. 2d for biexciton and exciton, respectively. The measurements yield $P_{0,b} = 0.3355(19)$ and $P_{0,x} = 0.3777(18)$ for biexciton and exciton, respectively. The values $P_{0,b}$ and $P_{0,x}$ were determined by summing the area under the central peak and dividing it with the sum of the areas of the adjacent peaks [27]. In the absence of the two-photon interference the three peaks would be identical, resulting in $P_\infty = 0.5$. The correspond-

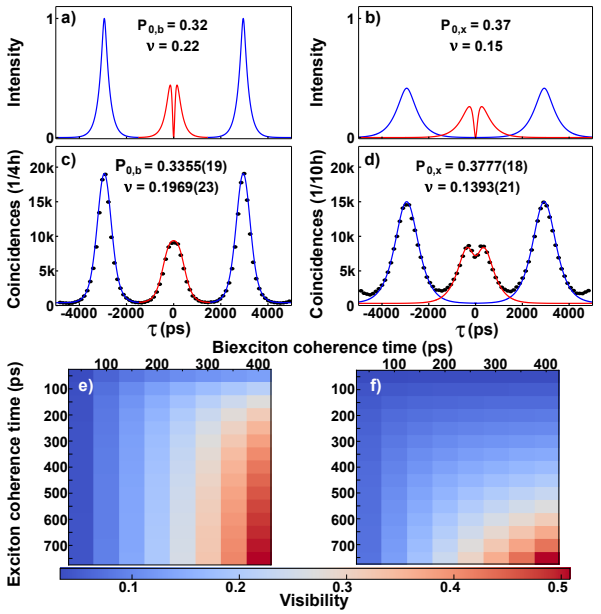

FIG. 2: The results of the sensor method calculation for a) biexciton and b) exciton. We assumed the coherence time of biexciton and exciton to be τ_{cb}=200 ps and τ_{cx}=450 ps, respectively. The $G^{(2)}_{HOM}(\tau)$ is plotted as the red central peak, while in blue we plotted the profile of the peak that would be achieved if no interference occurs. P_0 and ν match the experimentally observed ones. Panels c) and d) show the results of the two-photon interference measurement for biexciton and exciton, respectively. The measurement data are shown as points. The solid line is theory prediction achieved by convolution of the curves shown in the panel a) and b) with the response of the detector. The panels e) and f) show the visibility of the biexciton and exciton photon, respectively, for various values of the biexciton and exciton photon coherence time. The numerical values are given as tables in [19].

ing values of the visibility were found to be $\nu_b = 0.1969(23)$ and $\nu_x = 0.1393(21)$, respectively. These values suggest that the reduction of the interference contrast is not solely caused by the cascaded emission, but that there is a coexisting effect of the dephasing of the quantum dot levels. However, accessing the degree of dephasing for a cascaded decay is not straightforward. Specifically, when a quantum dot is driven in the two-level regime, exciting only the exciton, the information on the dephasing is commonly extracted from the two-photon interference measurement [28, 29]. This approach is motivated by slow dephasing mechanisms that cause methods such as the $G^{(1)}$ measurement using Michelson interferometer to record a higher degree of dephasing than commonly observed in a measurement implemented using photons emitted shortly after each other [30]. In a three-level system, two-photon interference is reduced by both the dephasing of any of the energy levels involved and cascade correlations. Therefore, estimating dephasing-induced photon distinguishability is more complex than in the two-level regime.

However, accessing the coherence time and purity of the photons pertaining to a cascade is crucial for experiments relying on two-photon interference. Therefore, we investigated this interplay between cascade-correlations and decoherence-induced reduction of two-photon interference contrast. The sensor method can also be used for this purpose. We introduced the dephasing via the Lindblad terms of the master equation [19]. This enabled us to determine $G^{(2)}_{HOM}(\tau)$ for any value of the coherence time attributed to either biexciton or exciton. Several examples of $G^{(2)}_{HOM}(\tau)$ we calculated using this method are plotted in Fig. 3 in [19], while the results that most closely match the experimentally observed values of $P_{0,b}$ and $P_{0,x}$ are shown in Fig. 2a and 2b, respectively. To fit the $G^{(2)}_{HOM}(\tau)$ calculated using sensor method shown in Fig. 2a and 2b to the experimental data, the $G^{(2)}_{HOM}(\tau)$ needs to be convoluted with the response of the detector employed in the measurement, resulting in curves shown in Fig. 2c and Fig. 2d. The data fitting confirmed the values of coherence time of τ_{cb}=200(25) ps and τ_{cx}=450(25) ps for biexciton and exciton, respectively. We used this result to determine the dephasing times of the biexciton and exciton, which are 346(74) ps and 1160(167) ps, respectively. In addition, the coherence time of the biexciton and exciton are, as anticipated, significantly longer than the $G^{(1)}$ values we measured employing the Michelson interferometer, which yielded 193(9) ps and 130(5) ps for biexciton and exciton, respectively.

We determined the values of the expected two-photon interference visibility for a wide range of different values of the coherence time. The results are shown in Fig.2e and Fig.2f for biexciton and exciton, respectively. They show that the visibility for the biexciton photon is unequally affected by the coherence loss of the biexciton and the exciton. The numerical values of the visibility are given as tables in [19]. Furthermore, to achieve a generalized analysis of the problem, we determined the values of the two-photon interference visibility for the same wide range of coherence time values and a biexciton to exciton lifetime ratio of 1:2 (200 ps and 400 ps). The plots and the table with numerical values are given in [19].

The most common method for eliminating undesired correlations between a pair of entangled photons is postselection. While sources based on spontaneous parametric downconversion rely on spectral postselection [10], the system we are addressing here asks for temporal postselection. In this scenario, to improve the purity of individual photons biexciton decay is truncated. We conducted both theoretical and experimental study of this scenario.

To theoretically address the effect of temporal postselection on two-photon interference visibility, we employed the quantum trajectory approach [31]. This method determines single quantum trajectories from the time evolution of the non-hermitian Hamiltonian,

$$H' = H_I - \frac{\mathrm{i}\hbar}{2}\sum_k C_k^\dagger C_k, \tag{5}$$

where C_k corresponds to the k-th collapse operator and H_I is the time-independent Hamiltonian describing our three level

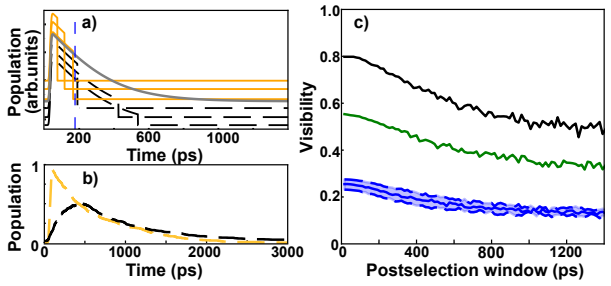

FIG. 3: a) The trajectories shown in orange exhibit a quantum jump before the 180 (ps) cut-off (blue dashed line), while the trajectories shown in black feature a quantum jump after the cut-off time. In gray is plotted the change of biexciton population with time calculated as the sum of all possible trajectories. The intensity of the individual plots is given in arbitrary units as the individual curves were vertically displaced for better visual presentation. b) The population change with time for exciton when the corresponding biexiton had a postselection cut-off at at 512 ps (black) and 64 ps (orange). c) Theoretically predicted result of postselection for no-dephasing (black), dephasing such that the coherence time of biexciton and exciton is at 80% of the Fourier-transform limit (green). The parameters of lifetime were equal to the ones of the emitter we used in the experiment. In blue is shown the result for our emitter, accounting for the coherence time determined experimentally. The light blue region accounts for the error with which we have determined the coherence time.

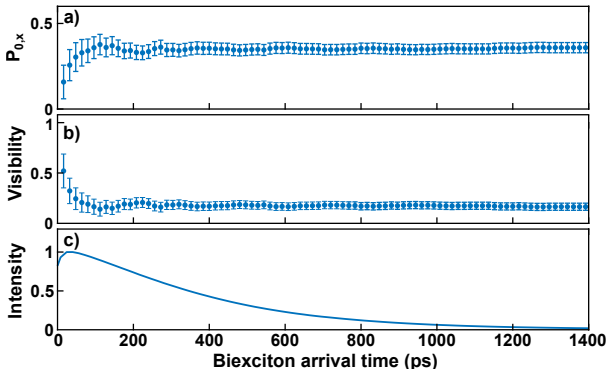

FIG. 4: a) The probability of a coincidence at the output of the beamsplitter for exciton photon $P_{0,x}$ and b) the visibility, respectively. Both of these results were achieved in a measurement conditioned by biexciton detection and plotted as a function of the size of the postselection window. c) Lifetime of the biexciton used to define the postselection window.

system together with the sensors (eq. (16) [19]). Each trajectory consists of a continuous evolution governed by H' and a quantum jump that takes place at a random time, enabling spontaneous emission. The continuous evolution is described by the operator $U(t) = e^{-iH't/\hbar}$, where the imaginary term of H' decreases the norm of the state vector such that $\||\psi(t_1)\rangle\| > \||\psi(t_2 > t_1)\rangle\|$. To describe the quantum jumps we discretized the time evolution and for each step we computed the norm of the state vector. We compared values of the norm of the state vector with a randomly generated number r ($0 \leq r \leq 1$). We assumed that when the condition $\||\psi(t_1)\rangle\| < r$ was satisfied the collapse and the re-normalization of the wavefunction took place.

While a single trajectory corresponds to the single evolution of the initial state under a random collapse condition, an averaged set of N trajectories ($N \to \infty$) approximates the density operator $\rho(t)$ typically obtained by solving the ensemble quantum master equation. Thus, with a numerical solution for a large number of trajectories, we can simulate the effect of temporal postselection based on the biexciton emission that occurs before a given time (Fig. 3a). This postselection procedure modifies the shape of the corresponding exciton wavepacket (Fig. 3b). The postselection effectively truncates the biexciton wavepacket, increasing the purity of the exciton-reduced density matrix. The increase in visibility as a result of the temporal postselection is shown in the Fig. 3c.

To test the effect of postselection experimentally, we conditioned the detection of exciton two-photon interference on the detection of a biexciton photon. This allowed us to use the time of biexciton photon detection as the postselection criterion. The results are shown in Fig. 4. The observed effect of postselection is stronger than predicted theoretically, especially for short postselection windows. However, it should be noted that the accuracy of the result is limited by the measurement statistics for such a short postselection window.

The concept of correlation of photons emitted as a cascade can be generalized to the phenomenon of time-energy entanglement as introduced by Franson [32]. The manifestation of Franson's interference is based on two properties of the emission time: the uncertainty of when a cascade is emitted and the strong correlations of the photons belonging to a cascade. This property of quantum dot emission has recently been exploited to demonstrate time-energy entanglement [33]. However, any other application of entangled photon pairs generated by a quantum dot requires the complete elimination of the cascade-induced correlations.

We have analysed the combined effect of decoherence and cascade-induced correlations on the visibility of the two-photon interference of biexciton (exciton) photons emitted sequentially from a semiconductor quantum dot. We have shown that the sensor method and the two-photon interference measurement provide access to the coherence times of the biexciton and exciton photons. We generalised our results and showed that, in terms of two-photon interference visibility, the biexciton and exciton photons do not respond equally to the loss of coherence. We also investigated temporal postselection as a method to improve the visibility of two-photon interference. Our results indicate that improvement is only possible in the absence of dephasing mechanisms, which typically set the quantum dot emission far from Fourier-transform limited. This result has an important implication: it points to the appropriate approach for designing photonic cavities that can improve the performance of quantum dot-based sources of entangled photon pairs. Namely, not only the biexciton emission rate must be modified to eliminate the cascade-induced

correlations, but also the exciton emission rate must be modified to overcome the dephasing.

This work was supported by the CAPES/STINT project, grant No. 88887.646229/2021-01. J. L. was supported by the Knut & Alice Wallenberg Foundation (through the Wallenberg Centre for Quantum Technology (WACQT)). A.P. would like to acknowledge the Swedish Research Council (grant 2021-04494). C.S gratefully acknowledges funding from the German Ministry of Research and Education (BMBF) within the project EQUAISE. EQUAISE was funded within the QuantERA program.

* Electronic address: ana.predojevic@fysik.su.se

[1] C. K. Hong, Z. Y. Ou, and L. Mandel Phys. Rev. Lett. **59**, 2044 (1987).
[2] D. Bouwmeester, J.-W. Pan, K. Mattle, M. Eibl, H. Weinfurter, and Anton Zeilinger, Nature **390**, 575 (1997).
[3] D. Fattal, E. Diamanti, K. Inoue, and Y. Yamamoto, Phys. Rev. Lett. **92**, 037904 (2004).
[4] M. Żukowski, A. Zeilinger, M. A. Horne, and A. K. Ekert, Phys. Rev. Lett. **71**, 4287 (1993).
[5] J. Beugnon, M. P. A. Jones, J. Dingjan, B. Darquié, G. Messin, A. Browaeys, and P. Grangier, **440**, 779 (2006).
[6] V. Krutyanskiy, M. Galli, V. Krcmarsky, S. Baier, D. A. Fioretto, Y. Pu, A. Mazloom, P. Sekatski, M. Canteri, M. Teller, J. Schupp, J. Bate, M. Meraner, N. Sangouard, B. P. Lanyon, and T. E. Northup, Phys. Rev. Lett. **130**, 050803 (2023).
[7] J. Wang, F. Sciarrino, A. Laing, and M. G. Thompson, Nature Photonics **14**, 273 (2020).
[8] D. Cogan, Z.-E. Su, O. Kenneth, and D. Gershoni, Nature Photonics **17**, 324 (2023).
[9] T. Walker, S. Vartabi Kashanian, T. Ward, and M. Keller, Phys. Rev. A **102**, 032616 (2020).
[10] W. P. Grice and I. A. Walmsley Phys. Rev. A **56**, 1627 (1997).
[11] H. Huang and J. H. Eberly, J. Mod. Opt. **40**, 915 (1993).
[12] C. Simon and J.-P. Poizat, Phys. Rev. Lett. **94**, 030502 (2005).
[13] K. Zyczkowski, P. Horodecki, A. Sanpera, and M. Lewenstein, Phys. Rev. A **58**, 883 (1998).
[14] M. B. Rota, F. Basso Basset, D. J. Tedeschi, and Rinaldo Trotta, IEEE Journal of Selected Topics in Quantum Electronics **26**, 1 (2020).
[15] G. Sęk, A. Musiał, P. Podemski and J. Misiewicz, J. Appl. Phys. **108**, 033507 (2010)
[16] G. Bacher, R. Weigand, J. Seufert, V. D. Kulakovskii, N. A. Gippius, A. Forchel, K. Leonardi, and D. Hommel, Phys. Rev. Lett. **83**, 4417 (1999).
[17] L. Ginès, et al. Phys. Rev. Lett. **129**, 033601 (2022).
[18] H. Jayakumar, et al. Phys. Rev. Lett. **110**, 135505 (2013).
[19] Supplemental material
[20] T. Huber, A. Predojević, H. Zoubi, H. Jayakumar, G. S. Solomon, and G. Weihs, Optics Express **21**, 9890 (2013).
[21] C. K. Hong, Z. Y. Ou, and L. Mandel. Phys. Rev. Lett. **59**, 2044 (1987).
[22] T. Legero, T. Wilk, M. Hennrich, G. Rempe, and A. Kuhn Phys. Rev. Lett. **93**, 070503 (2004).
[23] A. Kiraz, M. Atatüre, and A. Imamoğlu, Phys. Rev. A **69**, 032305 (2004).
[24] E. del Valle, A. Gonzalez-Tudela, F. P. Laussy, C Tejedor, M. J. Hartmann, Phys. Rev. Lett. **109**, 183601 (2012).
[25] R. Kaltenbaek, B. Blauensteiner, M. Żukowski, M. Aspelmeyer, and A. Zeilinger, Phys. Rev. Lett. **96**, 240502 (2006).
[26] T. Huber, A. Predojević, D. Föger, G. Solomon, G. Weihs, New Journal of Physics, **17**, 123025 (2015).
[27] C. Santori, D. Fattal, J. Vucković, G. S. Solomon and Y. Yamamoto, Nature **419**, 594 (2002).
[28] X. Ding, Y. He, Z.-C. Duan, N. Gregersen, M.-C. Chen, S. Unsleber, S. Maier, C. Schneider, M. Kamp, S. Höfling, C.-Y.Lu, and J.-W. Pan, Phys. Rev. Lett. **116**, 020401 (2016).
[29] S. Unsleber, Y.-M. He, S. Gerhardt, S. Maier, C.-Y. Lu, J.-W. Pan, N. Gregersen, M. Kamp, C. Schneider, and S. Höfling, Optics Express **24**, 8539 (2016).
[30] A. Thoma, P Schnauber, M Gschrey, M Seifried, J Wolters, J-H Schulze, A Strittmatter, S Rodt, A Carmele, A Knorr, T Heindel, S Reitzenstein, Phys. Rev. Lett. **116**, 033601 (2016).
[31] H. Carmichael Statistical Methods in Quantum Optics 1: master equations and Fokker-Planck equations, Springer Science and Business Media (1999).
[32] J. D. Franson Phys. Rev. Lett. **62**, 2205 (1989).
[33] M. Hohn, K. Barkemeyer, M. von Helversen, L. Bremer, M. Gschrey, J.-H. Schulze, A. Strittmatter, A. Carmele, S. Rodt, S. Bounouar, and S. Reitzenstein, Phys. Rev. Research **5**, L022060 (2023).

Supplemental Material: Impact of temporal correlations, coherence, and postselection on two-photon interference

Fernando Redivo Cardoso,[1,2] Jaewon Lee,[2] Riccardo Checchinato,[2] Jan-Heinrich Littmann,[2] Marco De Gregorio,[3] Sven Höfling,[3] Christian Schneider,[4] Celso J. Villas-Boas,[1] and Ana Predojević[2,*]

[1]*Departamento de Física, Universidade Federal de São Carlos, 13565-905 São Carlos, São Paulo, Brazil*
[2]*Department of Physics, Stockholm University, 10691 Stockholm, Sweden*
[3]*Technische Physik, Physikalisches Institut and Würzburg-Dresden Cluster of Excellence ct.qmat, Universität Würzburg, Am Hubland, D-97074 Würzburg, Germany*
[4]*Institut of Physics, University of Oldenburg, D-26129 Oldenburg, Germany*

Two-photon interference is an indispensable resource in quantum photonics, but it is not straightforward to achieve. The cascaded generation of photon pairs contains intrinsic temporal correlations that negatively affect the ability of such sources to perform two-photon interference, thus hindering applications. We report on how such correlation interplays with decoherence and temporal postselection, and under which conditions temporal postselection could improve two-photon interference visibility. Our study identifies crucial parameters and points the way to a source with optimal performance.

I. THE QUANTUM DOT PHOTON PAIR SOURCE

To perform the measurements, we used a quantum dot embedded in a micropillar cavity. The cavity was designed to consist of 5 top and 18 bottom pairs of $\lambda/4$ thick AlAs/GaAs distributed Bragg reflectors. The diameter of the micropillar was 2.74 μm. The sample was kept in a closed-cycle cryostat at 5.273(23) K. The quantum dot emission was collected using a 0.7 NA aspherical lens. We eliminated the excess laser scattering using a polarizer and a notch filter with a bandwidth of 0.65 nm. The single-photon nature of the emission was confirmed by measuring the autocorrelation function, as shown in Fig. 1. The results of the biexciton and exciton lifetime measurement are presented in Fig. 2a, along with the respective fits.

II. QUANTUM DOT LEVEL STRUCTURE AND SYSTEM DYNAMICS

In the interaction picture, the Hamiltonian for the three-level system can be expressed as follows

$$H_I = \Delta_x \sigma_{xx} + \frac{\Omega(t)}{2}\left(\sigma_{xg} + \sigma_{bx} + \text{h.c.}\right) \tag{1}$$

with $\sigma_{ij} = |i\rangle\langle j|$. The two-photon resonance is detuned from the single-photon resonance (ground state, $|g\rangle$, to exciton, $|x\rangle$) by Δ_x, which is equal to $2\pi\times 434$ GHz for the system we studied. We assume the laser excitation pulse to have a Gaussian profile with the following form

$$\Omega(t) = \Omega_0 \mathrm{e}^{-2\log(2)\left(\frac{t-t_0}{\sigma}\right)^2}, \tag{2}$$

where Ω_0 is the Rabi frequency. The intensity of the pulse peaks at $t = t_0$ and the pulse width is σ. Upon the quantum dot excitation the biexciton photon, ω_1, and exciton photon, ω_2, are emitted. The biexciton and exciton decay rates are Γ_b and Γ_x, respectively. The frequencies of the emitted photons are related as $\omega_2 > \omega_L > \omega_1$ (see Figure 1a in the main text). The biexciton and exciton lifetimes are τ_b and τ_x, respectively.

The system dynamics can be obtained by solving the master equation for the density operator ρ,

$$\dot{\rho} = -\mathrm{i}[H_I, \rho] + \sum_k \mathcal{L}_k \rho. \tag{3}$$

Here, the $\mathcal{L}_k$ $(k = 1, 2)$ are the Lindblad terms that account for spontaneous decay

$$\mathcal{L}_1\rho = \frac{\Gamma_b}{2}\left[2\sigma_{xb}\rho\sigma_{xb}^\dagger - \sigma_{xb}^\dagger\sigma_{xb}\rho - \rho\sigma_{xb}^\dagger\sigma_{xb}\right], \tag{4}$$

$$\mathcal{L}_2\rho = \frac{\Gamma_x}{2}\left[2\sigma_{gx}\rho\sigma_{gx}^\dagger - \sigma_{gx}^\dagger\sigma_{gx}\rho - \rho\sigma_{gx}^\dagger\sigma_{gx}\right], \tag{5}$$

and dephasing $\mathcal{L}_k$ $(k = 3, 4)$

$$\mathcal{L}_3\rho = \frac{\Gamma_{\text{db}}}{2}\left[2\sigma_{\text{db}}\rho\sigma_{\text{db}}^\dagger - \sigma_{\text{db}}^\dagger\sigma_{\text{db}}\rho - \rho\sigma_{\text{db}}^\dagger\sigma_{\text{db}}\right], \tag{6}$$

$$\mathcal{L}_4\rho = \frac{\Gamma_{\text{db}}}{2}\left[2\sigma_{\text{dx}}\rho\sigma_{\text{dx}}^\dagger - \sigma_{\text{dx}}^\dagger\sigma_{\text{dx}}\rho - \rho\sigma_{\text{dx}}^\dagger\sigma_{\text{dx}}\right], \tag{7}$$

with $\sigma_{\text{db}} = \sigma_{bb} - \sigma_{xx}$ and $\sigma_{\text{dx}} = \sigma_{xx} - \sigma_{gg}$. The factors $\Gamma_{\text{db,dx}} = (1/\tau_{\text{db,dx}})$ are the dephasing rates of biexciton and exciton, respectively. For the simulations, the population of the biexciton state, defined by

$$P_b = \Gamma_b \int_0^\infty \langle\sigma_{bb}(t)\rangle\, \mathrm{d}t, \tag{8}$$

was adjusted via Ω_0 to the value of $P_b = 0.5$. Figure 2b illustrates the biexciton and exciton population as a function of time. Figure 2c shows the 2D histogram of the biexciton and exciton emission times. The triangular shape of the 2D histogram indicates correlation that originates in the temporal ordering of the photon emission, mathematically described by two-photon wave function $\psi(t_b, t_x)$, given in the main text.

* ana.predojevic@fysik.su.se

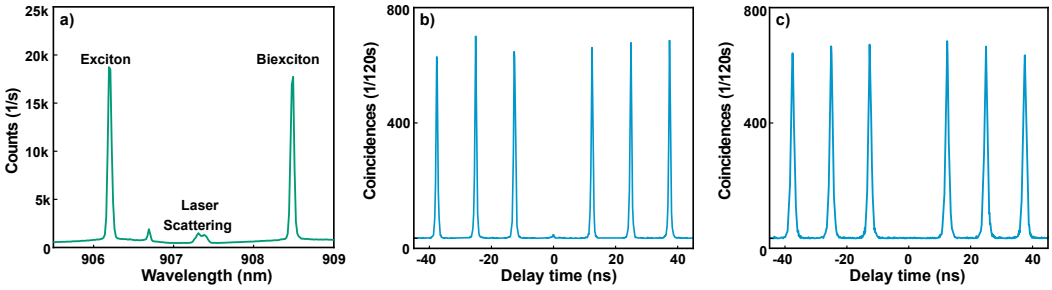

FIG. 1. a) Quantum dot emission spectrum, measured under two-photon resonant excitation. b) The results of auto-correlation measurements for b) biexciton and c) exciton. The measurements yield $g_b^{(2)}(0)$=0.0144(19) and $g_x^{(2)}(0)$=0.0074(11) for biexciton and exciton, respectively.

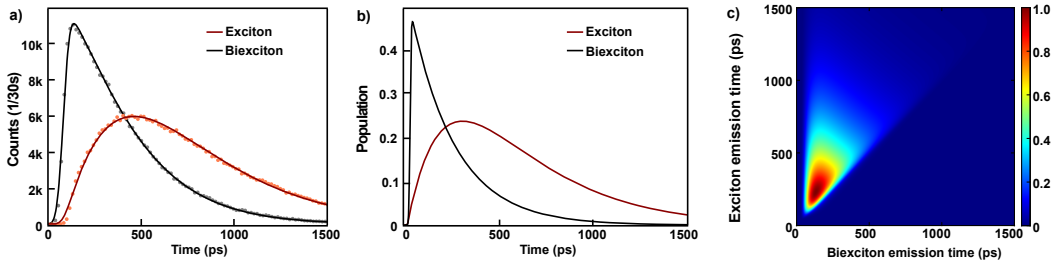

FIG. 2. a) Results of the biexciton and exciton lifetime measurements. We employed a 35 ps resolution single photon detector. From the data fit we deduct the lifetimes of $\tau_b = 237.16(59)$ ps and $\tau_x = 367.61(99)$ ps for the biexciton and exciton, respectively. b) Simulated quantum dot populations for biexciton ($|b\rangle$) and exciton ($|x\rangle$) as a function of time. The lifetimes were considered to be τ_b and τ_x, determined experimentally. c) 2D histogram of the emission times of the biexciton and exciton. The triangular shape reflects the time ordering of the emitted photons. The correlation intensity is normalized to unity.

III. SENSOR METHOD

As introduced in the main text the sensor method supplements the three-level system with 2 two-level systems, one per emission frequency. These two-level systems act as sensors and, as given in the main text, are described by the following Hamiltonian:

$$H_s = \sum_{j=1}^{2} \left\{ \omega_j \xi_j^\dagger \xi_j + g \left[(\sigma_{xb} + \sigma_{gx}) \, \xi_j^\dagger + \text{h.c.} \right] \right\}. \quad (9)$$

Upon performing a unitary transformation, the complete Hamiltonian of the system can be written as

$$\begin{aligned} H' = {} & \Delta_x \sigma_{xx} + \omega_1 \xi_1^\dagger \xi_1 + \omega_2 \xi_2^\dagger \xi_2 \\ & + \frac{\Omega(t)}{2} \left(\sigma_{gx} + \sigma_{xb} + \text{h.c.} \right) \\ & + g \sum_{j=1}^{2} \left[(\sigma_{xb} + \sigma_{gx}) \, \xi_j^\dagger \mathrm{e}^{-\mathrm{i}\omega_L t} + \text{h.c.} \right] \end{aligned} \quad (10)$$

where the terms that oscillate with double the laser frequency have been eliminated. To make the Hamiltonian time independent, we perform two unitary transformations involving sensor operators. The first transformation is $U_2 = \mathrm{e}^{-\mathrm{i}H_2 t}$, with H_2 being the free part of the sensor Hamiltonian

$$H_2 = \omega_1 \xi_1^\dagger \xi_1 + \omega_2 \xi_2^\dagger \xi_2. \quad (11)$$

By defining the sensor detunings $\Delta_i = \omega_i - \omega_L$ $(i = 1, 2)$, the Hamiltonian is transformed to

$$\begin{aligned} H'' = {} & \Delta_x \left| x \right\rangle\!\left\langle x \right| + \frac{\Omega(t)}{2} \left(\left| g \right\rangle\!\left\langle x \right| + \left| x \right\rangle\!\left\langle b \right| + \text{h.c.} \right) \\ & + \epsilon \sum_{i=1}^{2} \left[(\sigma_{xb} + \sigma_{gx}) \, \mathrm{e}^{\mathrm{i}\Delta_i t} \xi_i^\dagger + \text{h.c.} \right]. \end{aligned} \quad (12)$$

In the second transformation, the time dependence from the sensor coupling terms is removed using the following unitary operation $U_3 = \mathrm{e}^{-\mathrm{i}H_3 t}$, with

$$H_3 = \alpha_1 \xi_1^\dagger \xi_1 + \alpha_2 \xi_2^\dagger \xi_2, \quad (13)$$

where α coefficients are to be determined. The transformation acts on H'' in the following way

$$\begin{aligned} H_I = {} & -\alpha_1 \xi_1^\dagger \xi_1 - \alpha_2 \xi_2^\dagger \xi_2 + \Delta_x \left| x \right\rangle\!\left\langle x \right| \\ & + \frac{\Omega(t)}{2} \left(\left| g \right\rangle\!\left\langle x \right| + \left| x \right\rangle\!\left\langle b \right| + \text{h.c.} \right) \\ & + g \sum_{j=1}^{2} \left[(\sigma_{xb} + \sigma_{gx}) \, \mathrm{e}^{\mathrm{i}(\Delta_j + \alpha_j)t} \xi_j^\dagger + \text{h.c.} \right], \end{aligned} \quad (14)$$

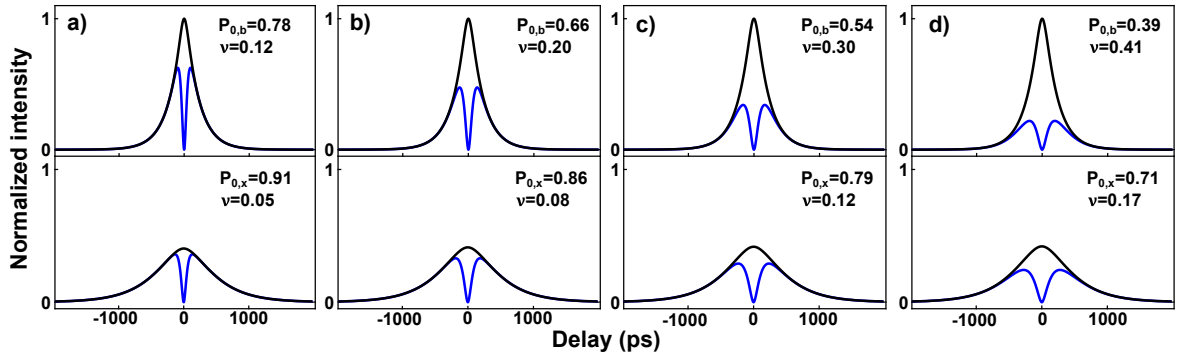

FIG. 3. Simulated values of $G^{(2)}_{HOM}(\tau)$ (in blue) obtained using sensor method and accounting for dephasing of the quantum dot levels. The coherence time of both biexciton and exciton were chosen to be a) 100 ps, b) 200 ps, c) 300 ps d) 400 ps. The top image shows the $G^{(2)}_{HOM}(\tau)$ of the biexciton while the bottom one shows the $G^{(2)}_{HOM}(\tau)$ of the exciton. for better comparison on each image is shown the mode intensity (in black). While the selected coherence times are equal for the biexciton and, exciton the achieved values of the $P(\tau)$ and visibility (ν) (shown in each plot) are quite different.

resulting in a Hamiltonian that is time independent under the following conditions

$$\begin{cases} \Delta_1 + \alpha_1 = 0 \Rightarrow -\alpha_1 = \Delta_1 \\ \Delta_2 + \alpha_2 = 0 \Rightarrow -\alpha_2 = \Delta_2. \end{cases} \tag{15}$$

We employ this result to rewrite the time independent Hamiltonian as

$$\begin{aligned} H_I = \Delta_1 \xi_1^\dagger \xi_1 + \Delta_2 \xi_2^\dagger \xi_2 + \Delta_x \left|x\right\rangle\!\left\langle x\right| \\ + \frac{\Omega(t)}{2} \left(\left|g\right\rangle\!\left\langle x\right| + \left|x\right\rangle\!\left\langle b\right| + \text{h.c.}\right) \\ + g \sum_{j=1}^{2} \left[\left(\sigma_{xb} + \sigma_{gx}\right) \xi_j^\dagger + \text{h.c.} \right]. \end{aligned} \tag{16}$$

This adjustment in eq. (16) enables the sensors to be resonant to the respective optical transitions of the three level system. To this end, the sensor detunings Δ_1 and Δ_2 are chosen to be

$$\begin{aligned} \omega_1 &= \omega_b - \omega_x \\ \omega_1 - \omega_L &= (\omega_b - \omega_x) - \omega_L + \omega_L - \omega_L \\ \Delta_1 &= -\Delta_x, \end{aligned} \tag{17}$$

for sensor 1, and

$$\begin{aligned} \omega_2 &= \omega_x - \omega_g \\ \omega_2 - \omega_L &= \omega_x - \omega_L \\ \Delta_2 &= \Delta_x. \end{aligned} \tag{18}$$

for sensor 2. Finally, we consider each of the sensors to have a linewidth. These manifest as two additional Lindblad terms that we add to the master equation,

$$\mathcal{L}_j \rho = \frac{\kappa_j}{2} \left(2\xi_j \rho \xi_j^\dagger - \xi_j^\dagger \xi_j \rho - \rho \xi_j^\dagger \xi_j \right), \tag{19}$$

with $j = 1, 2$.

In our study, we use the sensor method where two quantized modes act as weakly coupled sensors to model the behavior of a detector. A notable advantage of this framework is its ability to compute N-photon correlations for arbitrary time delays and frequencies, making it suitable for application to any open quantum system. Since the emissions ultimately occur in free space, we assume that the linewidth κ_j associated with each of the sensors is broadband ($\kappa \gg 1$). The coupling strengths (g) associated with the sensors are made small, satisfying $\epsilon_j \ll \sqrt{\kappa_j \gamma_j / 2}$, to prevent the introduction of feedback into the main system. The sensor method has been previously developed and used to study photon-photon correlations in various physical systems [1, 2]. Moreover, no additional assumptions are imposed on the system, and the correlation functions obtained with the sensor operators correspond to the correlations in emission [3]. We employ and demonstrate the applicability of the sensor method to investigate time-resolved correlations, as well as to model the emission and two-photon interference of photons emitted as a part of the biexciton-exciton cascade.

IV. TWO-PHOTON INTERFERENCE

The Hong-Ou-Mandel (HOM) or two-photon interference manifests when two photons impinge on distinct ports of a beamsplitter. The photons will interfere, depending on their degree of indistinguishability. We investigated the two-photon interference of the consecutively emitted biexciton (exciton) photons while considering the inherent correlations present in biexciton-exciton cascade.

Our analysis considers as parameters the lifetimes of biexciton and exciton as well as the dephasing resulting from the drifting of the internal levels, all of which can exert an impact on the interference visibility of the generated photons. The two-photon interference properties are obtained, as explained in the main text, via the correlations of the auxiliary two-level

TABLE I. Values of the visibility, ν, for biexciton two-photon interference for the quantum dot we used in our measurements. The exciton coherence times are given in the row most to the left, while the values of the biexciton coherence time are given in the top column. All coherence times are in ps.

	50	100	150	200	250	300	350	400
50	0.087	0.112	0.129	0.143	0.153	0.162	0.169	0.175
100	0.092	0.124	0.151	0.175	0.196	0.215	0.233	0.249
150	0.093	0.129	0.162	0.192	0.221	0.249	0.276	0.302
200	0.094	0.132	0.168	0.203	0.237	0.272	0.307	0.343
250	0.095	0.134	0.172	0.210	0.249	0.289	0.331	0.375
300	0.095	0.136	0.175	0.215	0.257	0.302	0.350	0.401
350	0.095	0.136	0.177	0.219	0.264	0.312	0.365	0.422
400	0.095	0.137	0.179	0.222	0.269	0.321	0.377	0.440
450	0.096	0.138	0.180	0.225	0.274	0.328	0.388	0.456
500	0.096	0.138	0.181	0.227	0.277	0.334	0.397	0.469
550	0.096	0.139	0.182	0.229	0.281	0.338	0.404	0.481
600	0.096	0.139	0.183	0.230	0.283	0.343	0.411	0.491
650	0.096	0.139	0.184	0.232	0.285	0.346	0.417	0.500
700	0.096	0.139	0.184	0.233	0.287	0.350	0.422	0.508
750	0.096	0.140	0.185	0.234	0.289	0.353	0.427	0.515

TABLE II. Values of visibility, ν, for exciton interference, for the quantum dot we used in our measurements. The exciton coherence times are given in the column most to the left, while the values of the biexciton coherence time are given in the top row. All coherence times are in ps.

	50	100	150	200	250	300	350	400
50	0.033	0.035	0.035	0.036	0.036	0.036	0.036	0.036
100	0.042	0.047	0.049	0.050	0.051	0.052	0.052	0.052
150	0.049	0.058	0.062	0.064	0.066	0.067	0.068	0.068
200	0.054	0.067	0.073	0.077	0.080	0.082	0.084	0.085
250	0.058	0.075	0.085	0.091	0.095	0.099	0.101	0.103
300	0.062	0.082	0.095	0.104	0.111	0.116	0.120	0.123
350	0.064	0.089	0.106	0.118	0.127	0.135	0.141	0.146
400	0.067	0.095	0.116	0.132	0.145	0.155	0.164	0.171
450	0.069	0.101	0.126	0.146	0.163	0.177	0.189	0.199
500	0.070	0.106	0.136	0.161	0.182	0.201	0.217	0.232
550	0.072	0.111	0.145	0.176	0.203	0.227	0.249	0.269
600	0.073	0.116	0.155	0.191	0.225	0.256	0.286	0.313
650	0.074	0.120	0.164	0.207	0.248	0.288	0.327	0.366
700	0.076	0.124	0.173	0.223	0.273	0.324	0.376	0.430
750	0.077	0.128	0.182	0.239	0.300	0.364	0.434	0.508

systems, i.e. sensors.

In figure 3 are shown several examples of $G^{(2)}_{HOM}(\tau)$ calculated for various values of the coherence length of the biexciton and the exciton. The figures clearly demonstrate that even for the same values of the coherence length the biexciton and exciton will not exhibit the same P_0 and ν. Namely the potential to perform two-photon interference is always stronger

TABLE III. Values of visibility, ν, for biexciton two-photon interference for the ratio of 2 between the lifetimes of the exciton and biexciton (400 ps and 200 ps, respectively). The first column on the left contains exciton coherence times, while the top row contains biexciton coherence times. All values are given in ps.

	50	100	150	200	250	300	350	400
50	0.090	0.115	0.134	0.147	0.158	0.167	0.175	0.181
100	0.094	0.128	0.156	0.181	0.204	0.224	0.242	0.258
150	0.096	0.134	0.167	0.199	0.230	0.260	0.289	0.315
200	0.097	0.137	0.174	0.211	0.247	0.284	0.322	0.358
250	0.097	0.139	0.178	0.218	0.260	0.303	0.348	0.392
300	0.098	0.140	0.181	0.224	0.269	0.317	0.369	0.420
350	0.098	0.141	0.184	0.228	0.276	0.328	0.385	0.443
400	0.098	0.142	0.185	0.231	0.282	0.337	0.399	0.463
450	0.098	0.142	0.187	0.234	0.286	0.345	0.411	0.480
500	0.099	0.143	0.188	0.236	0.290	0.351	0.420	0.494
550	0.099	0.143	0.189	0.238	0.294	0.356	0.429	0.507
600	0.099	0.144	0.190	0.240	0.296	0.361	0.436	0.518
650	0.099	0.144	0.190	0.241	0.299	0.365	0.443	0.528
700	0.099	0.144	0.191	0.242	0.301	0.369	0.449	0.536
750	0.099	0.144	0.191	0.244	0.303	0.372	0.454	0.544
800	0.099	0.144	0.192	0.244	0.304	0.374	0.458	0.551

TABLE IV. Values of visibility, ν, for exciton two-photon interference for the ratio of 2 between the lifetimes of the exciton and biexciton (400 ps and 200 ps, respectively). The first column on the left contains exciton coherence times, while the top row contains biexciton coherence times. All values are given in ps.

	50	100	150	200	250	300	350	400
50	0.032	0.034	0.034	0.035	0.035	0.035	0.035	0.035
100	0.041	0.046	0.048	0.049	0.050	0.050	0.051	0.051
150	0.048	0.056	0.060	0.062	0.064	0.065	0.066	0.066
200	0.053	0.065	0.071	0.075	0.078	0.080	0.081	0.083
250	0.057	0.073	0.082	0.088	0.093	0.096	0.098	0.100
300	0.060	0.080	0.093	0.101	0.108	0.112	0.116	0.119
350	0.063	0.086	0.103	0.114	0.123	0.130	0.136	0.140
400	0.065	0.092	0.112	0.128	0.140	0.150	0.158	0.164
450	0.067	0.098	0.122	0.141	0.157	0.170	0.182	0.191
500	0.068	0.103	0.131	0.155	0.175	0.193	0.208	0.221
550	0.070	0.108	0.141	0.169	0.195	0.218	0.238	0.256
600	0.071	0.112	0.150	0.184	0.215	0.245	0.272	0.296
650	0.072	0.117	0.158	0.198	0.237	0.275	0.311	0.344
700	0.073	0.121	0.167	0.214	0.261	0.308	0.356	0.401
750	0.074	0.124	0.175	0.229	0.285	0.345	0.408	0.469

with biexciton photon. On the other hand, and as shown in the Fig. 1 of the main text the cascade correlation alone induces equal reduction of the interference contrast.

In the tables I and II we give the numerical values of the visibility for biexicton and exciton, respectively. These values have been calculated for the quantum dot emitter that we em-

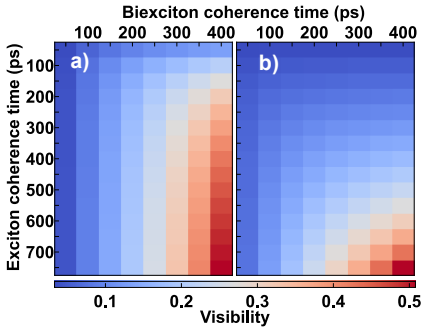

FIG. 4. The panels a) and b) show the visibility of the biexciton and exciton photon respectively for various values of the biexciton and exciton photon coherence time. The numerical values are given in tables III and IV.

ployed in the experiments. These values of the visibility are also graphically presented in the the Figure 2e and 2f of the main text.

In addition to this we also have calculated the values of the visibility for an emitter that has the ratio of 2:1 between the exciton and the biexciton lifetime (400 ps and 200 ps, respectively). These values are shown in the the tables III and IV, while the plot is shown in the Figure 4.

[1] M. Peiris, B. Petrak, K. Konthasinghe, Y. Yu, Z. C. Niu, and A. Muller, Phys. Rev. B **91**, 195125 (2015).
[2] E. Darsheshdar, M. Hugbart, R. Bachelard, and C. J. Villas-Boas, Phys. Rev. A **103**, 053702 (2021).
[3] E. del Valle, A. Gonzalez-Tudela, F. P. Laussy, C Tejedor, M. J. Hartmann, Phys. Rev. Lett. **109**, 183601 (2012).
[4] H. Carmichael Statistical Methods in Quantum Optics 1: master equations and Fokker-Planck equations, Springer Science and Business Media (1999).